EMISSION GUIDED RADIATION THERAPY: A FEASIBILITY STUDY

A Dissertation
Presented to
The Academic Faculty

by

Qiyong Fan

In Partial Fulfillment
of the Requirements for the Degree
Doctor of Philosophy in
Medical Physics

School of Mechanical Engineering
Georgia Institute of Technology
August 2013

EMISSION GUIDED RADIATION THERAPY: A FEASIBILITY STUDY

Approved by:

Dr. Lei Zhu, Advisor
School of Mechanical Engineering
Georgia Institute of Technology

Dr. John N. Oshinski
Department of Biomedical Engineering
Georgia Institute of Technology

Dr. Chris C.-K. Wang
School of Mechanical Engineering
Georgia Institute of Technology

Dr. Dingkang Zhang
School of Mechanical Engineering
Georgia Institute of Technology

Dr. Xiangyang Tang
Department of Radiology
Emory University

Date Approved: May 1, 2013

To the love of my parents

ACKNOWLEDGEMENTS

This work would not have been possible without the financial support from Georgia Institute of Technology new faculty startup fund and Reflexion Medical, generous help and persistent guidance from my coworkers, friends, and many other people.

In particular, I am deeply grateful to Akshay Nanduri and Dr. Samuel Mazin from Reflexion Medical. They have been extremely supportive for my investigations of this work. I thank them for providing me with yearlong internship support, enormous resources and help for my research, and unforgettable memories of all happy moments in California. I am greatly indebted to Dr. Mazin for his efforts, guidance, and contributions in every possible way on this dissertation.

This work has received tremendous help from people across many institutions. In particular, I thank Dr. Sue Wallace, Dr. Michael Kaus, Dr. Ying Xiong, Hari Gopalakrishnan and Dr. Matthieu Bal from Philips Radiation Oncology Systems for providing a Pinnacle workstation and technical support. I thank Dr. Frédéric Tessier and the National Research Council of Canada for providing the VMC++ software, and CliQr Technologies for providing cloud computing resources. I would also like to thank Dr. Tianye Niu, Xue Dong, Jaewon Yang, Dr. Billy Loo, Dr. Tokihiro Yamamoto, Dr. Edward Graves, Dr. Paul Segars, Dr. Youngho Seo, Dr. Xun Jia, Dr. Norbert Pelc, Dr. David Townsend, Dr. Charles Pelizzari, Dr. Chin-Tu Chen, Dr. Ralph Weichselbaum, Dr. Paul Keall, and Dr. James Welsh for generous help and useful discussions.

In addition, I want to give sincere gratitude to my dissertation reading committee members, Dr. Xiangyang Tang, Dr. Chris Wang, Dr. Dingkang Zhang, and Dr. John Oshinski, for their helpful comments and suggestions that have substantially

improved the quality of this dissertation.

Last, I would like to express deepest appreciation to my advisor Dr. Lei Zhu, without whom I could not have made it this far in my life. Dr. Zhu has always been there to help with his incredible talent and never-ending guidance. I am extremely grateful for all the knowledge and experience he has given to me, all the research skills he has taught me, and his ever-present willingness and remarkable efforts to guide me through all possible challenges. I could not feel luckier to have him as my mentor during the past four years.

TABLE OF CONTENTS

LIST OF TABLES

LIST OF FIGURES

LIST OF ACRONYMS

3DCRT 3D conformal radiation therapy.

4DCT four dimensional computed tomography.

ABC active-breathing control.

BEV beam's eye view.

bMLC binary multileaf collimator.

CBCT cone beam computed tomography.

CT computed tomography.

CTV clinical target volume.

DIBH deep-inspiration breah-hold.

DMLC dynamic multileaf collimator.

DVH dose volume histogram.

EBRT external beam radiation therapy.

ECT emission computed tomography.

EGRT emission guided radiation therapy.

FDG 2-[^{18}F]fluoro-2-deoxy-D-glucose.

FSB forced shallow breathing.

GATE Geant4 Application for Tomographic Emission.

GTV gross tumor volume.

HDR high dose rate.

hIMRT helical IMRT.

IGRT image guided radiation therapy.

IMRT intensity modulated radiation therapy.

IRB institutional review board.

ITV internal target volume.

LDR low dose rate.

Linac linear accelerator.

LOR line of response.

MC Monte Carlo.

MLC multileaf collimator.

MRI magnetic resonance imaging.

MVCT megavoltage computed tomography.

OARs organs at risk.

PET positron emission tomography.

PTV planning target volume.

RPM real-time position management system.

RT radiation therapy.

SAD source-to-axis-distance.

SBRT stereotactic body radiation therapy.

SPECT single photon emission computed tomography.

SRS stereotactic radiosurgery.

VMAT volumetric modulated arc therapy.

VMC++ voxel based Monte Carlo.

SUMMARY

The effectiveness of cancer treatment is compromised by the need to reduce the uncertainties originating from a variety of factors including tumor volume delineation, patient setup, and irregular physiologic motion. In particular, effective yet practical tumor motion management remains a major challenge in current external beam radiation therapy. Many strategies such as motion encompassment, breath-hold techniques, and respiratory gating have been proposed in the literature and implemented clinically. These methods have shown success in certain situations with different limitations. With the advent of image guided radiation therapy, real-time tumor tracking methods have become popular in clinics to proactively address the challenge with on-board tumor localization. Nevertheless, such techniques rely on surrogate signals and have been reported vulnerable to errors. In this dissertation, emission guided radiation therapy (EGRT) is proposed as a new modality for effective and practical management of cancer treatment uncertainties. One implementation of EGRT is to use positron emission tomography (PET) emissions in real-time for direct tumor tracking during radiation delivery. Radiation beamlets are delivered along PET lines of response by a fast rotating ring therapy unit consisting of a linear accelerator and PET detectors. A complete treatment scheme with capabilities of accurate tumor tracking and dose planning is proposed to implement this EGRT concept. Simulation studies with a physical phantom, 4D digital patient model, and clinical patient data are carefully designed to evaluate the feasibility and performance of EGRT. We show that with the capabilities of achieving both tumor tracking and sophisticated intensity modulation, EGRT has the potential to enable an effective implementation of 4D radiation therapy with true biological targeting and other advantages.

CHAPTER I

INTRODUCTION

1.1 Radiation Therapy

This work focuses on proposing and demonstrating the concept of emission guided radiation therapy (EGRT) [30, 67, 68, 28] for potential personalized cancer treatment. EGRT is proposed as a new modality of radiation therapy (RT), or specifically external beam radiation therapy (EBRT) for the scope of this dissertation. This section first gives an introduction to the general background of cancer treatment using radiation and then describes modern therapy techniques as well as radiation delivery machines which are widely used in current clinical practice.

1.1.1 General Background

The three most common cancer treatment techniques are: surgery, chemotherapy, and RT. About half of cancer patients receive RT during their treatment course [2]. RT uses high-energy radiation (e.g. x-rays, gamma rays, and charged particles) to damage the DNA of malignant cancer cells so as to kill them. This is achieved directly or indirectly with charged particles or free radicals within the cells [38]. RT can be used alone or in combination with other treatment methods such as surgery and/or chemotherapy. Depending on the stage of a tumor, RT can be given with curative intent of eliminating it, or palliative intent of preventing the patient from suffering caused by the tumor. For example, it is often used to shrink a tumor that is pressing on the spine which causes pain or near the esophagus which prevents the patient from eating [2].

Since RT may also damage normal cells based on the same principle, the delivery

of the radiation needs to be properly planned to achieve the best outcome with minimal side effects. A basic RT chain includes the sequential procedures of simulation, treatment planning, and radiation delivery, as illustrated in Figure 1.1.

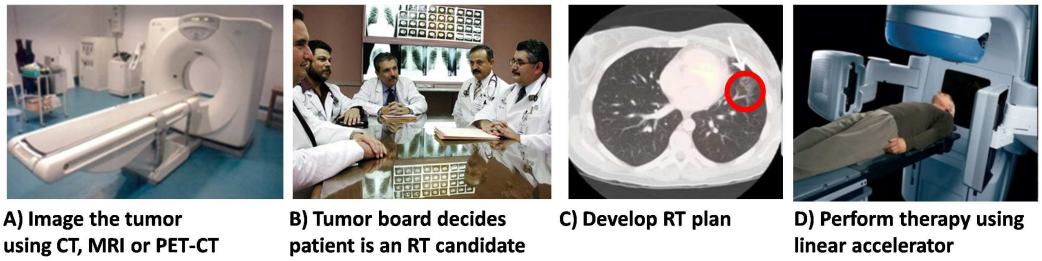

Figure 1.1: A typical radiation therapy chain.

In the simulation step, patients are imaged with diagnostic scans including computed tomography (CT), which is most commonly used, magnetic resonance imaging (MRI), PET, and ultrasound to identify useful information such as tumor location, size, and shape. The image scans are then used for treatment planning where tumors and organs at risk (OARs) are contoured, the dose prescription is determined, and the delivery plan of the radiation beams is optimized. The prescribed radiation can vary depending on many factors such as the type of cancer, the proximity of radiosensitive normal tissues, and the patient's age as well as medical conditions. The resultant treatment plan is finally used for daily radiation delivery after proper patient setup which aims to ensure that patients can be treated exactly as planned.

Radiation can be delivered outside the patient body by a linear accelerator (Linac), inside the patient by placing a radiation source near the tumor, or by administration via mouth/vein, referred to as EBRT, brachytherapy, and systemic radiation therapy, respectively. Among them, EBRT and brachytherapy are the most widely used in clinical practice.

1.1.2 Brachytherapy

Brachytherapy or internal radiation therapy is defined as a short-distance treatment of malignant disease with radiation emanating from small sealed sources, referred to as seeds [79]. The seeds are placed directly into or near the treatment volume using specialized delivery devices including needles, catheters, or other carriers that are specific to certain tumor sites. Figure 1.2 illustrates an example of source placement into a prostate tumor using needles under the image guidance of ultrasound.

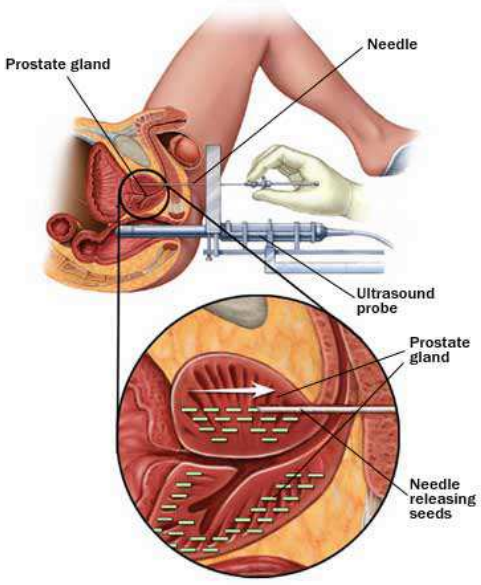

Figure 1.2: Seed implant into prostate with ultrasound guidance [1].

Brachytherapy can be implemented as a low dose rate (LDR) or high dose rate (HDR) treatment. In LDR treatment, low-dose radiation emitted from the source continuously irradiates the cancer cells over a period of several days or even longer. In HDR treatment, radiation sources are loaded into or near the cancer sites typically by a robotic machine at the beginning of each treatment session and removed once the session is finished.

The radiation source placement in brachytherapy is either temporary or permanent. Permanent placement techniques surgically seal the seeds within the patient

body without removing them even after the radiation has completely decayed. Due to this fact, permanent placement is only applied in LDR brachytherapy. Temporary placement techniques use specific carriers to load the sources, which are removed at the end of the treatment in the reverse order of source loading. Temporary placement can be applied in either LDR or HDR treatment.

Brachytherapy can be used alone or in addition to EBRT to boost radiation within a tumor [103]. As compared to EBRT, the advantage of brachytherapy is that it may deliver higher doses of radiation to certain types of cancers while causing less healthy tissue damage. However, it is only good for well localized small lesions and the procedure is very labor intensive. Brachytherapy is rarely used for tumors with significant motion such as those in the lung.

1.1.3 External Beam Radiation Therapy

EBRT is the most common form of RT. It can be delivered with beams of electrons, photons (e.g. x-rays, gamma rays), and protons/heavy particles. Among these, a photon beam is the most widely used clinically. Proton beam deposits much of its energy at the end of the beam path (called the *Bragg peak*) while a photon beam deposits energy in small packets all along the way through human tissue. Electron beams have much less penetration ability into tissue and therefore are often used to irradiate superficial tumors (e.g. skin cancer).

Cancer patients usually receive EBRT over a period of several weeks, divided into many daily treatment fractions [63], referred to as fractionated radiation therapy. Many factors will affect the total number of treatment fractions. For example, the total target prescription dose to be delivered is one of the most important factors. Such fractionated treatment schemes minimize the damage to normal tissue and increases the likelihood of irradiating cancer cells at their most radiosensitive periods of the cell cycle. Other fractionation schemes including accelerated fractionation,

hyperfractionation, and hypofractionation are being investigated and may be used toward applicable patient cases [22].

1.1.4 Modern Therapy Techniques

In the early days of RT, a tumor was targeted based on the bony structures in the 2D transmission images of the patient. Radiation delivery was planned using the planar radiographs by collimating rectangular fields that circumscribe the inferred tumor location [110]. RT advanced into the era of 3D with the advent of CT in the 1970s which allowed physicians to use x-ray projection data to build a 3D patient model for more accurate tumor targeting. Since then, the frontier of RT has been pushed forward again and again due to the fast development of many technologies such as the invention of advanced computers and the multileaf collimator (MLC). In particular, the following modern therapy techniques are being widely used in daily radiation treatments: 3D conformal radiation therapy (3DCRT), intensity modulated radiation therapy (IMRT), image guided radiation therapy (IGRT), and stereotactic treatments.

- **3DCRT**

  3DCRT shapes the profile of each radiation beam/field using a MLC to fit that of the target from a beam's eye view (BEV) (see Figure 1.3). The MLC is typically made of lead or tungsten which highly attenuate the photon beam. When the resultant treatment volume conforms to the tumor shape, the radiation toxicity to the surrounding healthy tissue is significantly reduced as compared to the previous generations of RT. The target prescription dose can therefore be increased.

- **IMRT**

  In addition to the shaping of each radiation field, IMRT further modulates the beam intensity within each field to allow increased flexibility to control the dose

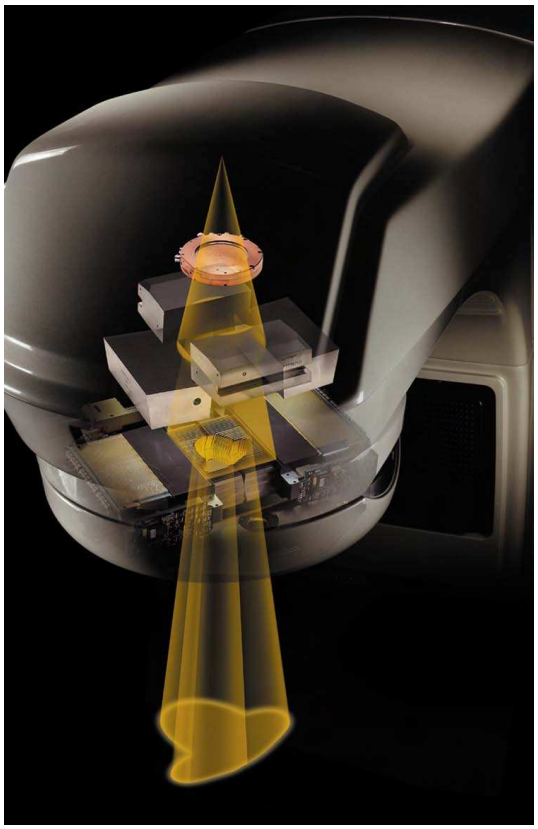

Figure 1.3: The treatment beam passes through the primary collimator and is shaped by a device called a MLC so that it conforms to the tumor profile. Adapted from Varian Medical website.

distribution. This is usually accomplished by the movement of MLC leaves. IMRT can be delivered in a step-and-shoot mode or a rotational mode which is often independently referred to as volumetric modulated arc therapy (VMAT). Figure 1.4 shows an illustration of a step-and-shoot IMRT treatment with nine fields.

To calculate the beam intensities across all fields so as to achieve a desired dose prescription, inverse treatment planning is commonly used. Inverse planning is a process of finding the optimal beam intensity distribution given certain dose constraints for both the target and OARs. This is different from the traditional forward treatment planning where the radiation oncologists select the number and angles of the treat beams in advance and computers then calculate how

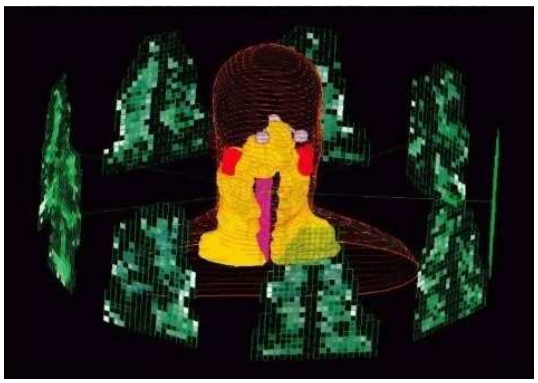

Figure 1.4: Illustration of a nine-field IMRT treatment for a head and neck case. 3D view of nine IMRT beams are shown with the gray levels representing the intensity values to be applied. Adapted from [3].

much dose will be delivered from those beams. Compared with 3DCRT, IMRT possesses more flexibility for delivering highly conformal treatments and performs better in cases where OARs that are close to the target need sparing. For example, IMRT is commonly used in head and neck cancer cases to control the risk of some side effects by minimizing the damage to the salivary glands.

- **IGRT**

  IGRT aims to provide image guidance to eliminate the cancer treatment uncertainties for better RT treatment outcomes. This is achieved by integrating cutting-edge image guidance into each step of the RT treatment. It includes image-based tumor definition during the treatment planning stage, image-based patient positioning devices for patient setup, and image-guided tumor targeting tools during radiation delivery. Guidance provided by different types of imaging scans including fluoroscopy, cone beam computed tomography (CBCT), MRI, or PET has been proposed in the literature. Radiation treatment can benefit significantly from such treatment guidance. For example, the on-board imager could identify tumor size and location changes due to irradiation. It allows the corresponding repositioning of the patient or the adjustment of the radiation

beam during treatment. IGRT may also address the problem of tumor motion and shorten the duration of treatment due to improved targeting accuracy. Therefore, IGRT plays an increasingly important role in modern RT.

- **Stereotactic Treatments**

  Stereotactic treatments here refer to stereotactic radiosurgery (SRS) and stereotactic body radiation therapy (SBRT). SRS gives a relatively large single radiation dose to a small target area. It thus requires great targeting accuracy which is achieved by using an external head frame for 3D target localization and immobilization. SRS can be performed with charged particles, Gamma Knife, CyberKnife, or modified Linac. These systems can give a high dose of radiation without excess damage to healthy tissue. However, SRS is typically limited to the treatment of small tumors with well-defined contours. For example, it is most commonly used in the treatment of brain tumors, spinal tumors, and brain metastases from other cancer types.

  Different from either SRS or 3DCRT, SBRT delivers radiation therapy in several sessions to tumors which are outside the brain and spinal cord. Compared with 3DCRT, SBRT usually uses smaller radiation fields and higher fraction doses. One of the major reasons for more than one fraction in SBRT is that the above tumors can move with the patient body and cannot be targeted as accurately as tumors within the brain or spine. SBRT is also limited to treat only small and isolated tumors (e.g. cancers in the lung and liver).

1.1.5 Radiation Delivery Machines

EBRT is typically delivered using a machine called a Linac. Back in 1953 when the first cancer patient was treated with a Linac, the radiation delivery machine was very bulky preventing its widespread use. With the development of radiation therapy technologies over the past several decades, the Linac has become more and

more compact, advanced, and readily available to the public. It is now capable of delivering highly conformal radiation to the target with great accuracy, precision, and efficiency given the exact tumor location.

The essential component of a medical Linac is the linear accelerator that accelerates electrons to kinetic energies from 4 to 25 MeV using microwave radiofrequency fields of 103 MHz (L band), 2856 MHz (S band), or 9350 MHz (X band). Treatment photon beams are produced when the accelerated electrons strike the x-ray target. Currently there are three major types of medical Linacs in the clinic. They are typically categorized based on the dose delivery geometry: conventional, helical, and robotic. Although different in radiation delivery geometry, these Linacs follow the same principle of photon beam generation and the corresponding treatment follows the same basic therapy chain as discussed above.

- **Conventional**

  The modern conventional Linac is usually built on a C-arm gantry that rotates precisely around a treatment couch with the mechanical isocenter maintained to within a sphere of 1 mm radius. The Linac head on the gantry's C-arm can deliver the radiation beam with 360 degrees of rotation around the patient. The photon beam is shaped before irradiating the patient with a combination of several collimating structures. High-density field blocks and additional edge blocks first produce beams of square fields with a size up to 40 cm by 40 cm at the patient. The computer controlled MLC is then used to further shape the beam to fit the profile of the specific target from the BEV at the selected treatment angles.

- **Helical**

  A helical Linac delivers the radiation slice-by-slice rather than irradiating the entire tumor volume at one time as in a conventional Linac. The accelerator,

photon-producing target, and collimation systems are mounted on a ring gantry. The part of the machine that delivers radiation can thus rotate completely around the patient in the same manner like a typical diagnostic CT scanner. As the gantry rotates, the patient simultaneously slides through the system bore to achieve the full coverage of the target. The primary collimator of the helical Linac produces a fan beam of photons, which can be further collimated by a binary multileaf collimator (bMLC). CT-guided IMRT can therefore be implemented in such a helical delivery geometry.

- **Robotic**

  A robotic Linac delivers radiation by making use of an industrial robot to hold a compact accelerator. There is no isocentric rotation of the compact Linac. Rather, the Linac is controlled by the computer to irradiate the tumors from many angles in 3D space (except from below the patient). To fully exploit this flexibility, field sizes are kept very small to reduce the bulk of the system. Such robotic delivery schemes allow the selection and use of many noncoplanar beam angles to build up dose within the tumor volume.

1.2 Treatment Uncertainties

Despite the different geometries in radiation delivery, all types of Linac machines face the same challenge of reducing the treatment uncertainties in RT. Treatment uncertainties can originate from a variety of factors which exist in each step of the RT workflow. For example, the uncertainty of tumor volume delineation during simulation, patient setup uncertainty prior to treatment, irregular physiologic tumor motion during treatment, interfraction tumor motion between treatment sessions, and unpredictable tumor response to radiation such as tumor volume shrinkage over the course of treatment [70]. Moreover, there are even more treatment uncertainties when the

patient has two or more moving tumors. As an example, Figure 1.5 illustrates the severe uncertainty in delineation of lung target volumes using only CT versus PET/CT among radiation oncologists.

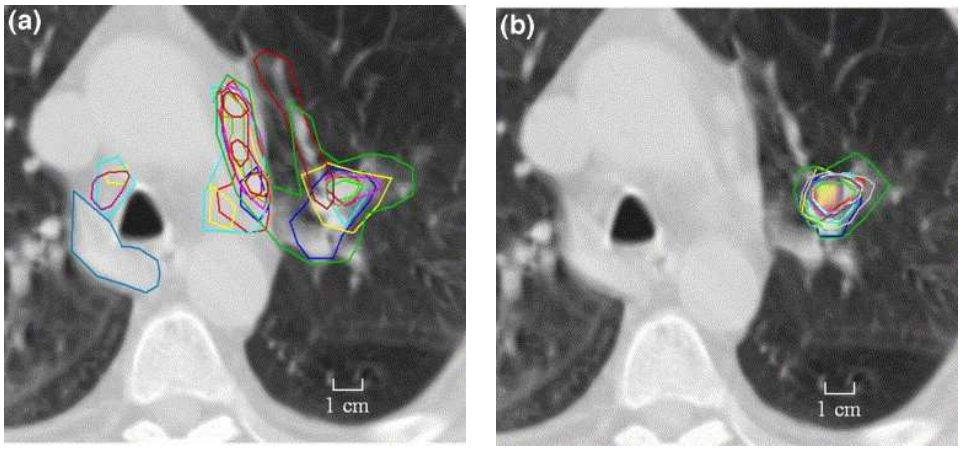

Figure 1.5: Comparison of tumor volume delineation using (a) CT only and (b) matched PET/CT by the same 11 radiation oncologists (Figure from [92]).

As a result, even though advances in image-based radiation treatment planning and delivery have greatly improved the ability to conform the radiation dose to the tumor, the effectiveness of cancer treatment is significantly compromised by the need to reduce the above treatment uncertainties. For example, IMRT is capable of generating highly conformal dose distributions to the target while sparing healthy tissue [27, 56]. However, IMRT treatment performance is heavily determined by the accuracy of tumor tracking, which cannot be guaranteed in the presence of intrafractional organ motion [37, 11, 45] and interfractional patient setup errors [11, 25, 58]. Also, in the treatment of thoracic or abdominal tumors using SBRT, extremely precise localization of the tumor is required to avoid irradiating nearby critical structures. This precise localization is challenged by the need to account for the movement of tumors in the body caused by respiration.

Among all treatment uncertainties, intrafractional tumor motion is one of the biggest challenges. It has cast significant limitations on radiation treatment outcomes

at each step of the RT chain: image acquisition, treatment planning, and radiation delivery (see sections below). Motion amplitude can be as high as 5 cm in the lung region [49]. Frequency variations, amplitude changes, and baseline shifts occur on a regular basis both interfractionally and intrafractionally [80, 86, 78, 89], and are difficult to predict [93]. Figure 1.6 illustrates such an example. The tumor trajectory can be highly irregular across different patients and hysteresis (different inhale and exhale paths) can occur. Plus, motion is independent of size, location, and pulmonary function [93]. Therefore, accurate tumor tracking and effective yet practical tumor motion management remain major challenges in current RT practice.

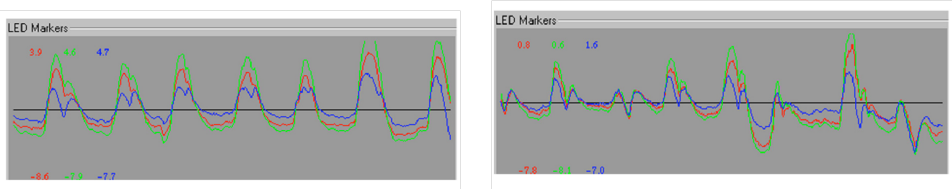

Figure 1.6: Variations in respiratory patterns from the same patient based on data measured 3 minutes apart (Figure from [49]). Motion is measured using infrared reflectors placed on the patient surface. Three color curves correspond to motion in the superior-inferior (SI), anterior-posterior (AP), and medial-lateral (ML) directions, respectively.

- **Image acquisition**

  When target motion is not accounted for, severe artifacts may appear in the images acquired during simulation or the on-board imaging process. These artifacts typically present themselves as distortions of the tumor volume and/or incorrect positional and volumetric information. This is commonly observed for thoracic and abdominal tumors. The resultant artifacts will generate target/normal tissue delineation errors and adversely affect the dose calculation accuracy. In addition, small mobile tumors may not even be detected due to such motion artifacts.

- **Treatment planning**

Treatment planning can be greatly influenced by tumor motion, setup error, and other uncertainties since it naturally requires accurate knowledge of tumor location. A common solution is to define a planning target volume (PTV) that covers the full motion extent. This is suboptimal since it increases the volume of healthy tissue to be irradiated and consequently the likelihood of treatment-related complications. However, if motion is not taken care of, the target will not receive adequate dose coverage which may significantly deteriorate the treatment benefits. Furthermore, the image artifacts in the simulation step will generate additional errors for the planning process.

- **Radiation delivery**

  Without an effective method to account for organ motion and setup error, the actual delivered dose distribution may severely deviate from the planned one. As a result, either the target may receive inadequate dose coverage or the sensitive OARs may not be successfully spared, or both. As compared to conventional 3DCRT treatments, dose performance can be even more severely impacted in IMRT treatments since dose gradients within the treatment fields are very sensitive to tumor location uncertainty.

1.3 Motion Management Strategies

With more and more advanced techniques applied in clinics to tackle the non-motion related issues, the challenges brought by motion have therefore become the bottleneck of radiation cancer treatments. As the fatality of lung cancer is still the highest among all cancer types in the U.S., and as many non-lung cancers metastasize to the lung and liver where motion is a significant problem, this has spurred a flood of research activities over the past decade for each step of a complete motion management scheme including imaging, planning and delivery, well documented in AAPM TG-76 report [49]. Four main categories of strategies can be summarized as breath-hold,

gating, tracking, and motion encompassment.

1.3.1 Breath-hold

Breath-hold methods aim to reduce the respiration motion effect via active or passive breath-holding which may freeze the tumor motion to the maximum possible extent. This is typically achieved with the following techniques:

1. Deep-inspiration breah-hold (DIBH): In a DIBH technique, the patient is verbally coached to breath through a mouthpiece connected to a spirometer that measures air flow [39]. The volume of air breathed in and out is calculated and displayed as a function of time. The therapist can then help the patient to maintain a reproducible state of maximum breath-hold for 10 to 20 seconds during which radiation is delivered.

2. Active-breathing control (ABC): ABC apparatus can suspend breathing at any predetermined position and is often used at 75% of deep inhale for best balance between reproducibility of the breathing trace and patient comfort [107]. The device is mainly composed of a digital spirometer connected to a balloon valve. Real-time lung volume is monitored during the entire respiratory trace. Once a specified lung volume value is reached, the valve is inflated with an air compressor for a predefined duration of 15 to 30 seconds. During this period, the patient's breath is being actively held.

3. Self-held breath-hold: In this technique, the patient is given a hand-held switch that is connected to a Linac interlock circuit. When the patient holds his/her breath, he depresses the switch to clear the interlock allowing the therapist to activate the beam for radiation delivery. When the patient needs breath, he can release the switch which will turn the beam off through the interlock.

4. Forced shallow breathing (FSB): FSB employs a stereotactic body frame with an

attached plate for abdominal compression. The respiratory/diaphragm motion is reduced due to the applied pressure and the patient can have limited normal respiration throughout the whole treatment.

1.3.2 Gating

The essential principle of motion gating is to irradiate the moving tumor within only a small portion of the motion path. In other words, gating techniques turn the beam on only when the target is determined to be traveling within a pre-planned area, referred to as the gating window. Some gating techniques can be applied in both simulation and delivery steps to treat the tumor as if there were no motion.

Gating techniques rely on a surrogate signal of the motion, either external or internal, to determine whether the tumor is within the desired gating window [53, 17]. Such determination can be based on the displacement of the measured surrogate signal. The radiation beam is activated whenever the surrogate signal is within a pre-set window of relative displacement. If the motion can be assumed periodic, the determination can also be based on the phase of the surrogate signal. The radiation beam is turned on when the phase of the respiration signal is within a pre-set phase window. In either case, respiratory gating typically relies on an indirect tracking method where the correlation between the tumor and the surrogate motion is not guaranteed [42, 97].

1. **External respiration signal**: The commercially available and most widely discussed gating system is the Varian real-time position management system (RPM) (Varian Medical Systems, Palo Alto, CA) [102]. It is mainly for respiratory motion and is based on an external respiration signal. During treatment, an infrared reflective plastic box serving as the external fiducial marker is placed on the patient's anterior abdominal surface. The inroom camera is able to accurately detect the reflective markers and display the corresponding motion signal

as a function of time. Once a stable respiration trace has been established, gated simulation and radiation delivery can be initiated.

2. **Internal respiration signal**: The major principle of gating using an internal respiration signal is to obtain the surrogate signal of tumor motion by implanting internal fiducial markers into the patient and then tracking the positions of these markers based on their radiopaque properties with x-ray [34]. The fiducials (e.g. 2-mm-diameter gold spheres) can be implanted in or near the tumor using a percutaneous or bronchoscopic implanting technique. A pair of stereotactic kilovoltage x-ray imaging systems is typically in place to monitor the positions of fiducials in all three dimensions several times a minute. The beam is turned on when each fiducial is found to be within the pre-defined gating window. Such procedures can also be applied to set up the patient.

1.3.3 Real-time Tracking

Real-time tumor tracking addresses the motion problem more proactively by repositioning the radiation beam or the patient dynamically to ensure that the beam and the target are matched as planned all the time. Continuous real-time tracking ideally can eliminate the need of a tumor-motion margin, while maintaining a 100% duty cycle for efficient dose delivery. To succeed, the following major challenges need to be properly tackled.

1.3.3.1 Determine The Tumor Position

Localizing the tumor during treatment is the most important and challenging task in real-time tracking. The most direct way is to image the tumor itself in real time with a sufficiently high frequency using fluoroscopes (typically a pair of fluoroscopes are mounted in the treatment room) [88]. For example, lung tumors sometimes can be visualized directly in fluoroscopic images at a certain exposure level depending on their location. More often though, tumors in the body will not have well-defined contours

and sufficient contrast for image segmentation and therefore the use of fiducial markers as surrogates for localization is necessary. These markers can be the same as those used in the gating technique. They are usually high-Z materials implanted in or near the mobile tumors, which can be readily identified in x-ray images to determine their 3D coordinates. These coordinates are finally used for the calculation of tumor translation, rotation, and marker migration.

Due to motion irregularity, the tumor needs to be imaged many times a second in the above tracking methods, which is a major limitation with x-ray imaging that can result in excessive imaging dose to the patient [87]. Non-radiographic tumor tracking methods have been developed to avoid this issue [105, 54]. In this type of method, miniature radiofrequency coils are implanted into the patient and tracked electromagnetically in three dimensions from outside the patient. The real-time tumor position can then be monitored at a sufficiently high frequency.

However, the above methods are invasive procedures and they are not only costly, but also sacrifice patient comfort and may cause severe side effects such as pneumothorax [33]. Moreover, implanted internal markers cannot accurately depict the whole tumor volume and shape by showing only several points on the tumor, and marker migration is also an issue [66]. Some researchers have proposed direct tumor targeting methods using fluoroscopic images without implanting markers [20, 8]. In these studies, tumor motion phase or position is determined by matching the real-time acquired fluoroscopic images with the pre-built templates, which may fail when the tumor boundary is unclear in fluoroscopic images [57].

1.3.3.2 Treatment System Response

With the tumor position properly monitored in real time, a further challenge of high performance radiation therapy is to accurately deliver the dose to a fast moving target based on the tumor location information. Typical methods of dynamic motion

compensation include gating [43], couch shifting [104, 7], dynamic multileaf collimator (DMLC) tracking [69, 48, 81], and robotic tracking [15]. Gating delivery has been discussed in the previous section 1.3.2. Couch correction repositions the patient to align with the beam by an amount of translation determined from the difference of the planned and actual tumor position. The disadvantage is that it may introduce continuous back-and-forth patient motion, which leads to problems of patient discomfort and low treatment tolerance [70].

A more popular approach is DMLC repositioning. Rather than reposition the patient, DMLC tracking repositions the beam so as to follow the real-time tumor position by correspondingly moving the MLC leaves. The new spatial distribution of MLC leaves is calculated based on the deviation of the actual tumor position from the planned one. DMLC tracking may require leaf speeds that may at times exceed the MLC speed limit [70]. It also involves non-trivial adjustments to the base treatment plan for satisfactory performance [50].

Another advanced method of tumor tracking uses the robotic Linac to flexibly reposition the beam to follow the tumor's motion (e.g. CyberKnife system by Accuray). With the robotic Linac controlled to move in six degrees of freedom, this approach has the advantage of adapting to the full 3D motion of the tumor. However, it usually requires the implantation of fiducial markers for image guidance.

No matter which method to use, they all face the same issue: system latency. That is, after the detection of the tumor position, there is a significant time delay before the system can make any response. This can be due to many factors such as the processing of tracking images, the calculation of actual translation, movement of the couch to a new position, or repositioning of the MLC aperture. For example, it is reported that a delay of 90 ms between identification of fiducial marker coordinates and radiation response is observed in a gating system [49].

Therefore, without an effective method that is able to tolerate the system latency,

the tumor position needs to be predicted in advance so that the synchronization of the beam with the tumor's varying position is possible. This is necessary regardless of the method used and it applies to both gating and real-time tracking systems. However, as discussed earlier, the human breathing cycle can have significant cycle-to-cycle and long-term fluctuations in both displacement and frequency. This makes the tumor position very difficult to predict and thus leaves the latency challenge not fully tackled. Another concern with the dynamic motion compensation method is that the beam may pass through a sensitive critical structure that is to be avoided in the original treatment plan.

1.3.4 Motion Encompassment

Although the motion problem has caused a series of issues that may degrade the benefits of RT, many radiotherapy facilities are not equipped with sophisticated therapy machines or other resources to explicitly account for tumor motion according to the above strategies. In this case, motion encompassment is another option to proceed without enormous resources and personnel requirements. The principle of motion encompassment makes it feasible to be implemented similarly as the therapy of a static tumor. Motion encompassment mainly involves imaging the moving tumors properly to obtain the internal target volume (ITV) that covers the full extent of the tumor motion, subsequent definition of PTV as the expansion of the ITV, and final treatment planning and dose delivery based on a static PTV.

1.3.4.1 Imaging

To image a moving tumor, various types of CT scanning including slow CT, breath-hold CT, and four dimensional computed tomography (4DCT) can be used. Slow CT is generally the method most available to obtain the motion-encompassing volume and commonly used for lung tumors in the high-contrast area. In slow CT, the scanner is operated very slowly and multiple CT scans can be averaged such that multiple

respiration phases are recorded per slice. Hence, the reconstructed image of the tumor should show the full extent of motion that has occurred during the scan.

Acquiring separate inhale and exhale gated/breath-hold CT scans is another common solution to obtain the ITV volume. The method requires a step of image fusion on both scans and consequent contouring to delineate the desired ITV [99]. As compared to slow CT, this method needs longer imaging time and relies on the patient's ability to hold his/her breath reproducibly. To save time, one can apply this method only within the tumor travel region while for other patient areas a free-breathing CT can be used.

The most advanced solution for obtaining high-quality CT data in the presence of tumor motion is 4DCT or respiration-correlated CT [91, 24]. Four dimensional data can be analyzed to accurately determine the tumor trajectory and ITV volume. Retrospectively correlated CT is closest to an ideal 4D imaging modality as it captures the whole breathing cycle and provides reconstructed images for all motion phases of the period. This is achieved by sorting all acquired projections to each phase of the motion with the help of a surrogate signal. A limitation of 4DCT is that it assumes the motion is periodic and it can be divided into certain phases. However, this is not guaranteed due to common variations in respiratory patterns.

1.3.4.2 Planning and Delivery

After the ITV volume is determined using the proper type of CT scan, the subsequent process of treatment planning and delivery will be similar as that for static tumors. Specifically, adequate margins are added to the ITV to account for patient setup uncertainty, the motion changes between imaging and treatment, etc. The amount of margin added depends on the specific patient case. With the motion and other treatment uncertainties taken care of by the ITV volume and the additional PTV margin, IMRT planning and delivery can be implemented without major modification

from the therapy of static tumors as in current clinical practice.

As discussed previously, one of the major disadvantages of the gating concept is that it results in a treatment with low duty cycle, and even frequent interruptions due to the irregularity of tumor motion. As for 4D tracking methods, the complexities of 4D planning, the invasiveness of necessary internal fiducial marker implantation, and additional uncertainties of coordinating 4D planning with 4D delivery prevent their widespread use clinically. As a result, the motion-encompassing methods still have vast popularity due to their high efficiency, ease of implementation (requires least amount of resources), and compliance with current 3D therapy protocols and guidelines. It fits very well the needs of those RT facilities in which advanced tracking or gating systems are not readily available.

As a sacrifice, as pointed out in section 1.2, due to the usage of the ITV rather than the clinical target volume (CTV) for planning, more normal tissues are exposed to radiation as compared to gating and tracking methods. This limits the highest dose that can be prescribed to the PTV and GTV, resulting in lower tumor control [64]. Figure 1.7 illustrates that the toxicity may be increased significantly with increased mean lung dose. Thus, to improve upon the ITV approach, it is crucial to lower the mean lung dose.

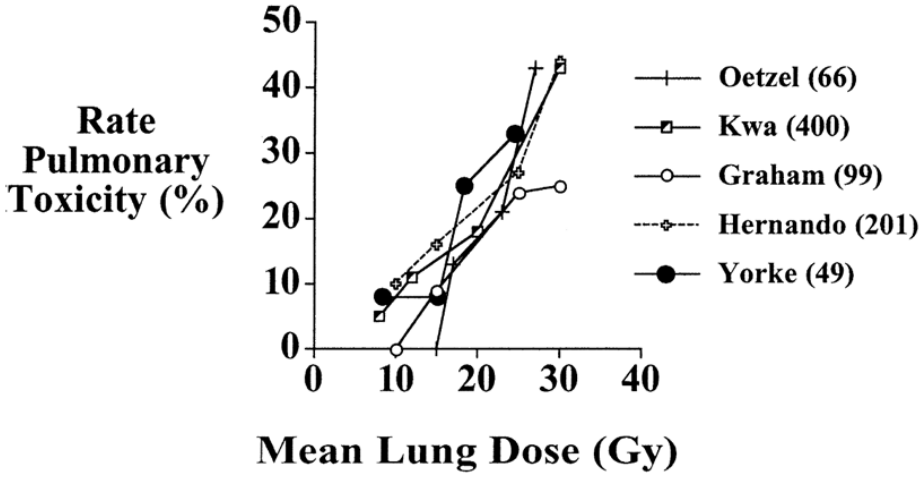

Figure 1.7: Pulmonary toxicity as a function of mean lung dose (Figure from [64]).

1.4 Emission Computed Tomography

Emission computed tomography (ECT) is a type of tomography based on radioactive emissions within the image subjects. ECT includes PET and single photon emission computed tomography (SPECT) based on how emissions are generated. PET and SPECT images are both representations of a patient's biological state. In this section, we will take PET as an example to introduce ECT imaging principles.

Although CT can provide good anatomic information about the patient, very often one has to rely on PET imaging to delineate the gross tumor volume (GTV) extent and provide other useful biological information of the tumor. This is because a tumor can have low contrast in CT images, which make it barely distinguishable from other surrounding normal tissues. Figure 1.8 shows an example of locating a tumor using commercially available PET/CT technology.

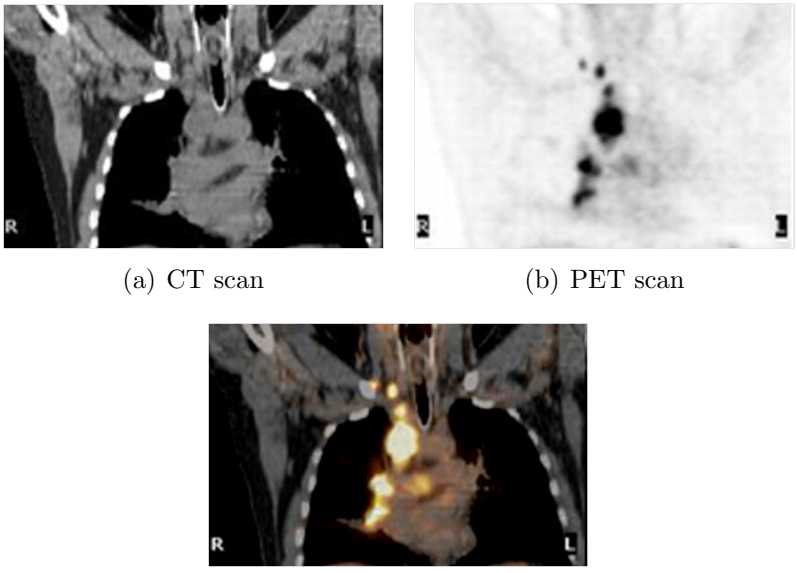

(a) CT scan (b) PET scan

(c) PET/CT scan

Figure 1.8: (a) CT scan provides good anatomic details about patient. (b) PET scan delineates tumor metabolic activity distribution. (c) PET/CT fusion indicates metabolic tumor volume with respect to surrounding normal tissues.

1.4.1 Principle

PET is extensively involved with cancer detection, staging, treatment decision-making, and assessment of therapeutic response in radiation oncology. It uses positron emissions as a signaling mechanism. Positrons are generated from radioactive decay of atoms in the molecular probe transported into the patient usually via injection. The following isotopes are typically used in PET imaging because of suitable decay times: ^{11}C, ^{13}N, ^{15}O, ^{18}F, ^{64}Cu, ^{82}Rb, and ^{124}I. The molecular probe that contains these atoms interacts with a living subject in the same way as a chemically identical molecule made of the corresponding stable isotopes. In addition, extremely small concentrations of the probe are used to generate an adequate PET signal. PET can therefore track cancer cells without affecting their behavior.

One of the most successful and widely used PET probes has been 2-[^{18}F]fluoro-2-deoxy-D-glucose (FDG). It consists of a modified molecule of glucose in which a radioactive fluorine isotope (^{18}F) substitutes for a hydroxyl group. After injection into the patient through a vein, FDG is transported from the blood stream into the cells by glucose transporters. In the cell, phosphorylation prevents the glucose from being released, resulting in FDG accumulation within the cell. Since FDG does not have the hydroxyl group as in normal glucose for further glycolysis, it cannot be further metabolized before radioactive decay. Hence, the FDG concentration can indicate the local rate at which the cells consume glucose. Higher concentration means higher intensity in reconstructed PET images. Since tumor cells typically have abnormally high metabolism, the tumor lesions usually appear brighter than background tissue on PET scans.

When trapped in cells, ^{18}F decays to emit a positron which annihilates with an electron within tens of microns to a few millimeters of the decay location. The annihilation results in the simultaneous emission of two back-to-back 511 keV photons, called annihilation photons. The major process can be represented using the following

formulas:

$$^{18}F \rightarrow ^{18}O + e^{+} + \upsilon \tag{1}$$

$$e^{+} + e^{-} \rightarrow \gamma + \gamma \tag{2}$$

When two annihilation photons are recorded by the detectors around the object, it can be inferred that a positron was emitted along the line that connects the two detectors involved, called the line of response (LOR), see Figure 1.9. The LOR also forms the basic unit of information for reconstructing PET images, often referred to as a coincidence event or coincidence count. Note that without advanced techniques such as time-of-flight PET, the exact location of emission on the line cannot be determined.

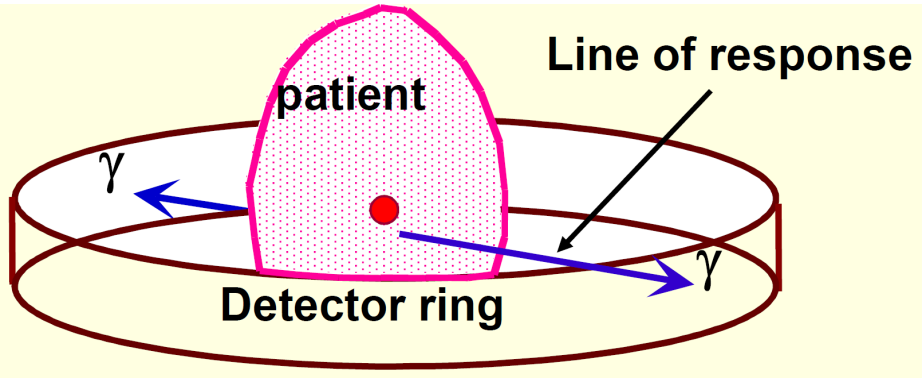

Figure 1.9: Illustration of LOR for detection.

There are two physical limitations that degrade the spatial resolution of PET imaging even if the scanner is perfect. The first one is that the positron travels a small distance (e.g. 0.22 mm full width at half maximum for ^{18}F) before it annihilates with an electron. Thus, the emission location may not be exactly on the line but rather in its proximity. The other major factor is the residual momentum carried by the positron when annihilation occurs. Due to this fact, the two annihilation photons are not emitted exactly 180° apart. There is a 0.3° uncertainty which translates to a spatial resolution loss of a few mm for clinical scanners.

1.4.2 Detection and Reconstruction

Annihilation photons are detected using radiation detectors that surround the subject, which are typically arranged in a ring structure. Since the photons must travel along the LOR or equivalently, the photon source must locate on the LOR, no additional transverse collimation is needed in a PET imaging system. 511 keV photons are very penetrating as compared to photons in the diagnostic energy range (60-140 keV). This is an advantage for PET imaging because they can easily escape from the patient body and hence yield a high photon count rate for detection. However, annihilation photons are hard to stop and detect for the same reason. Hence, PET radiation detectors are usually made from dense materials with high atomic number.

Most PET radiation detectors are composed of scintillation crystals, which convert the annihilation photon energy into light, and photodetectors. The most commonly used scintillation crystals are Lu_2SiO_5 (LSO), Gd_2SiO_5 (GSO), and $Bi_4Ge_3O_{12}$ (BGO). These crystals are cut in small, discrete elements and put together to form 2D arrays. Crystals are then linked through a light guide to a sensitive photodetector such as a photomultiplier tube to amplify the signal for processing.

During detection, there will be thousands of annihilations ongoing at the same time and hence lots of LORs can be formed. Incorrect pairing of photons that come from different annihilation events can occur, called false coincidence. This includes scattered coincidences and random coincidences. It is then crucial to determine the true LORs so that the correct information can be used for image reconstruction. Current PET imaging systems rely on an energy window and a time window to discriminate photon counts. An energy window of $511 \pm 30\%$ keV is typically enforced to reject scattered photons, which typically lose significant amount of energy, from being recorded. A time window is then used to select two single counts to form a coincidence event. Only two photons that are detected within the same time window can be used to form a LOR. The width of the time window is typically 6 or 12 ns for

current commercial systems. Figure 1.10 illustrates the essential components of PET imaging.

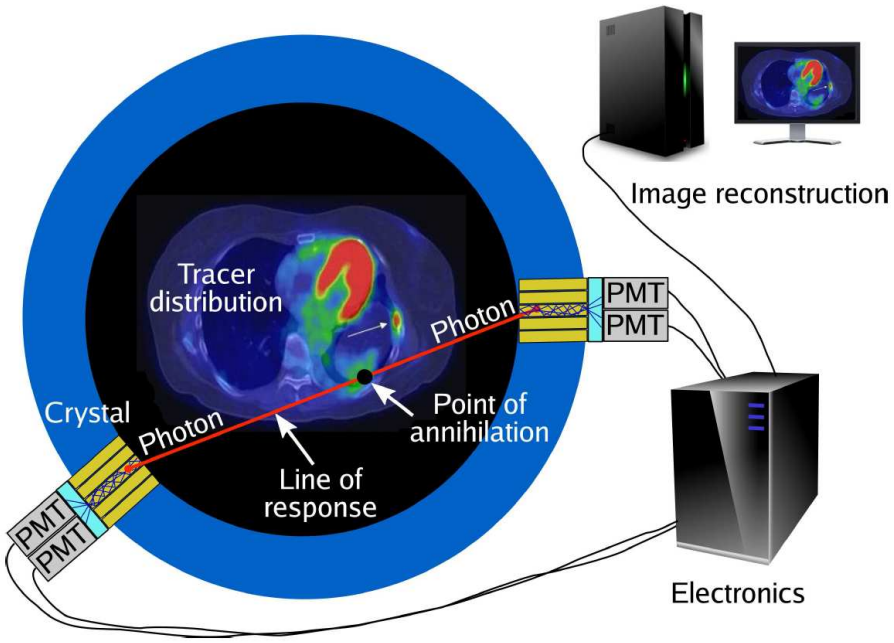

Figure 1.10: Essential components of PET imaging [75]. Anticollinear 511 keV photons are first generated and then detected by a combination of scintillation crystals (yellow) and photomultiplier tube. When the electronics records two photons in near coincidence, a coincidence event is generated forming the corresponding LOR (red line), which is stored in a computer for image reconstruction.

After the list of LORs which pass both the energy and time window is obtained, there are still corrections needed to be made before final image reconstruction. For example, attenuation correction is necessary to correct for the effect that photon pairs experience non-uniform attenuation when traveling within the patient (see Figure 1.11).

With necessary corrections done, there are mainly two types of algorithms available to reconstruct the desired PET images for diagnostic purposes: filtered back-projection and iterative reconstruction. The first one is faster since it is an analytic algorithm but has poorer noise characteristics while the latter is slower but typically yields better image quality.

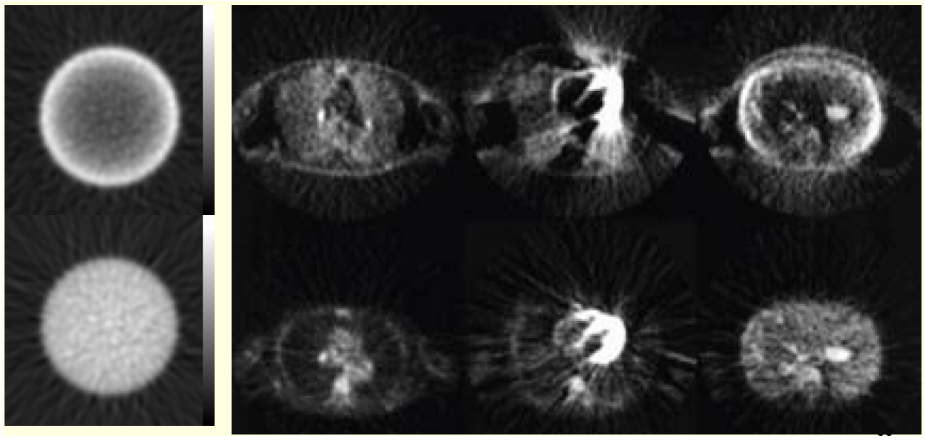

Figure 1.11: PET images before (top row) and after (bottom row) attenuation correction. Adapted from [98].

1.5 Motivation and Organization

1.5.1 Motivation

Tumor location uncertainties are common in radiation therapy due to treatment setup errors, tumor motion, and many other factors (see section 1.2). To alleviate this problem, many motion management strategies have been proposed, as described in section 1.3. Image guidance techniques, such as respiratory gating, are commonly used in the presence of large target motion. Fiducial markers are also frequently implanted into the disease sites to further improve the treatment guidance accuracy. Despite the demonstrated success under certain circumstances, these methods are still sub-optimal with respect to tumor tracking accuracy, treatment efficiency, patient comfort, complexity and cost effectiveness.

The ITV approach uses a very large margin to compensate for tumor motion and patient setup error to ensure dose coverage of the tumor. It has been widely used despite its limited ability to prescribe high dose to the GTV for better tumor control. Such limitation is due to the fact that the motion-encompassing methods do not explicitly incorporate any form of tumor tracking. A natural thought to improve upon the popular ITV approach is to develop a method that combines the strategies of

motion encompassment and tumor tracking. In addition, the tumor tracking method needs to be accurate, non-invasive, simple, and efficient. The current tumor tracking methods, which relies on external or internal surrogates, are essentially indirect approaches and therefore the tracking accuracy cannot be guaranteed all the time. Internal fiducial-based tracking are reported less vulnerable to errors however they are invasive and can cause significant patient discomfort as well as severe complications.

In search of an alternative method for real-time tumor tracking, ECT imaging becomes a viable approach. As indicated in section 1.4, ECT imaging is an effective method for cancer detection and tumor delineation. The tumor can be easily distinguished from background tissues using direct biological signals. Due to the fact that these signals are coming from the tumor itself, the ECT imaging makes itself an excellent candidate for direct and accurate tumor tracking. In addition, since the tumor tracking is based on the emission signals and no fiducial markers will be needed, ECT-based tumor tracking is non-invasive. The signals are emitted continuously and no gating techniques are necessary so that such tumor tracking can be very efficient as well. Unfortunately, there are currently no methods which are able to integrate ECT imaging for real-time tumor tracking purposes. This is because it usually takes minutes to collect enough emissions for image reconstruction. However, although ECT image-based guidance is slow, individual emissions can instantaneously reflect tumor location information.

In this dissertation, we propose, for the first time, a new RT modality which integrates direct emission guidance into radiation delivery for accurate and personalized RT treatment. We refer to it as *emission guided radiation therapy* or EGRT. This dissertation presents a comprehensive summary of our investigations on EGRT.

1.5.2 Organization

This dissertation is divided into six chapters. Chapter 1 gives background information on radiation therapy, RT treatment uncertainties, current major motion management strategies, ECT imaging in oncology, and the main motivation of this work.

Chapter 2 illustrates the proposal of the general EGRT concept, system design, and treatment planning approach. The implementation of the EGRT concept based on PET emission guidance is explained in detail. This includes a proposed EGRT system geometry, the basic EGRT algorithm to ensure tumor tracking, and a primitive dose modulation method.

Chapter 3 presents three EGRT applications to demonstrate the feasibility of EGRT for improved radiation therapy outcomes. This includes the application of tumor tracking, simultaneous tracking of multiple tumors, and treatment of a non-PET-avid target. Detailed simulation workflow and evaluation studies are presented.

Chapter 4 investigates the impact of major treatment parameters on EGRT treatment performance. Parameters including the number of firing points, PTV margin size, treatment time, EGRT spatial and time window size, and rotation period are discussed.

Chapter 5 proposes a treatment planning scheme that enables EGRT's capability of incorporating sophisticated planning modulation. This planning scheme is demonstrated with detailed simulation studies involving clinically acquired patient imaging data.

Chapter 6 further discusses the image-based implementation of the EGRT concept and other considerations, and concludes the dissertation with suggestions of future work.

CHAPTER II

EGRT TREATMENT

EGRT is a new concept for radiation treatment. Unlike conventional RT treatments where the tumor is not targeted or targeted based on a surrogate signal or anatomic structure, EGRT utilizes the biological signal emitted from the tumor itself to guide the delivery of radiation. Such emission guidance makes the often invisible tumor light up during radiation delivery and help deliver the radiation to the right position at the right time, especially in the presence of tumor motion or setup error.

This chapter mainly discusses the proposed EGRT system and treatment scheme and answers the following questions: What essentially is EGRT? How is radiation delivered based on emission guidance? What kind of treatment system is used? What are the procedures for simulation and patient setup? How is treatment planning performed?

2.1 EGRT Concept

2.1.1 General Considerations

EGRT broadly refers to any radiation treatment that directly uses emission guidance to facilitate dose delivery. It can be in the form of internal or external beam radiation therapy, depending on the specific design of EGRT. It is not limited to any specific type of radiation delivery geometry. The EGRT system can be based on a conventional C-arm, helical or robotic gantry geometry. In addition, EGRT does not conflict with any type of modern therapy techniques. IGRT and IMRT can be incorporated into EGRT after necessary modifications. The emission guidance can be from single photon emissions or positron emissions. The essential mechanism in an EGRT treatment is the use of emission signals as the guidance for dose delivery. This guidance

needs to be involved in a real-time fashion during actual radiation delivery. However, this does not mean that the possibility of utilizing emission guidance before or after RT treatment for other useful purposes should be eliminated.

Two types of EGRT treatments can be conceived based on how emission guidance is utilized: image-based EGRT [28, 112] and LOR-based EGRT. Image-based EGRT aims to reconstruct an image using collected LOR counts within subsecond time scales and then apply a tumor localization algorithm to identify the tumor location for conventional on-board treatment guidance. Promising results have been obtained for image-based EGRT, however, there are still challenges to tackle. This will be further discussed in Chapter 6.

LOR-based EGRT is instead a new treatment paradigm based on positron emissions (for the concept of positron emission, please see section 1.4). In PET, each detected LOR gives an approximate line-of-sight to the emission source almost instantaneously due to the intrinsic collimation effect of coincidence detection [18]. Instead of waiting minutes for enough LORs to form PET images, an LOR-based EGRT system delivers beamlets of therapeutic radiation along LOR paths individually as they are detected to achieve a helical dose delivery. The nearly real-time LOR response is made possible with a fast rotating Linac and collimation system to align the beam along the LOR path with a minimal lag time. The feasibility of rotating a Linac and a bMLC has been previously demonstrated, as well as a rotating PET system [60, 61, 13, 59, 9].

With the integration of real-time emission detection and radiotherapy, tumor localization and dose delivery are more naturally unified. Tumor tracking is inherent, automatic, and direct. This work is specifically on the feasibility demonstration of LOR-based EGRT, which will be referred to simply as EGRT for the remainder of this dissertation. The emission guidance of EGRT stems from the physical principle of positron annihilations in PET imaging. Therefore, EGRT can be classified as a

new type of broadly defined IGRT method. It should be noted that the treatment guidance in EGRT is not provided by PET images, but rather by individual emissions.

2.1.2 Positron Emission Based EGRT

One major application of EGRT is to achieve accurate tumor tracking in current RT to significantly reduce or eliminate the treatment uncertainties. Positron emission based EGRT or LOR-based EGRT integrates PET imaging for near real-time tumor tracking and thus is a perfect fit for this application. It can also be implemented as a feasible and novel solution to solve the dilemma of the ITV approach discussed in Chapter 1.

Other groups have investigated emission based tracking methods where positron sources are implanted as fiducial markers [111, 14]. EGRT is unique in that it involves administration of positron emitting radiotracers into the patient and uses the signals from the radiotracer that is concentrated in the target for true biological tracking. Such signals are able to locate the tumor accurately in a non-invasive way with a high temporal resolution. The LOR detected for one positron event naturally defines the line of sight which passes through the uptake site. Enlightened by this physical principle, we mount a positron imaging system on a radiation therapy machine (compact Linac) and perform radiation therapy and real-time tumor tracking simultaneously (to be discussed in detail in the following sections). The schematic diagram of this EGRT concept is shown in Figure 2.1.

The gamma-ray detectors as used in a PET scanner detect the LORs generated from positron events. Once the positron event is determined to be likely coming out of the treatment target, the corresponding LOR will be enqueued into a list of beamlets waiting for dose delivery. At the first time when the rotating Linac aligns with the enqueued LOR, radiation will be delivered along the LOR passing through the target.

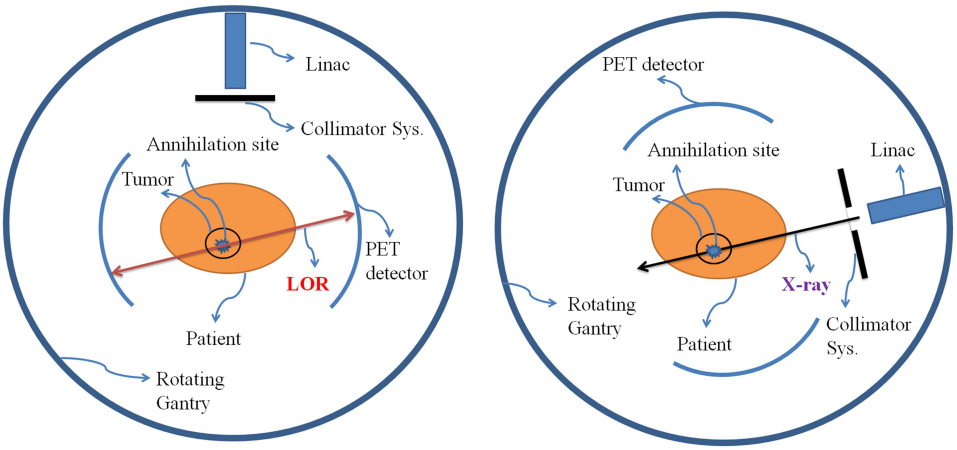

(a) LOR Detection (b) Dose delivery

Figure 2.1: The schematic diagram of the proposed EGRT treatment. (a) LOR detection using PET detectors, (b) Dose delivery along the detected LOR path.

As can be appreciated from the above scheme, there are two major difficulties in the implementation of EGRT. The first is how to design a delivery algorithm to ensure tumor tracking given the system latency. The second is how to invent a planning scheme to incorporate desired intensity modulation as in IMRT treatments. A major contribution of this work is to provide and demonstrate viable solutions to the above two challenges.

2.2 System Design

2.2.1 General Considerations

As mentioned in section 2.1.1, the design of EGRT system depends on how the emission guidance is used. For example, an EGRT system that uses single photon emissions (e.g. SPECT) will require gamma-camera-type detectors and that which uses positron emissions will need PET detectors. Regardless of the type of emission used, the EGRT system should be properly designed to fully exploit the provided guidance mechanism and achieve tumor tracking. At the same time, the design needs to be practical for system manufacturing purposes. For example, for image-based EGRT, the system should at least have two components: PET detectors and a Linac. The

PET detectors are used to collect LORs for image reconstruction and the Linac is used to deliver dose based on the real-time acquired tumor location estimated from reconstructed PET images. Since 3D location is needed, the PET detectors should be able to cover the entire moving tumor at all times during RT and thus the longitudinal extent should be more than several centimeters. Such a system can be based on a conventional Linac geometry where rotation speed is limited.

For LOR-based EGRT, the system also needs to have both PET detectors and a Linac. However, since radiation is delivered beamlet-by-beamlet along each individual LOR, a helical dose delivery geometry is more suitable. To achieve tumor tracking with a high temporal resolution, the system needs to rotate fast enough to effectively freeze tumor motion. This can be made possible with a small longitudinal extent of PET detectors and a compact Linac mounted on a closed ring gantry. The following section presents such a detailed EGRT system design for the LOR-based concept, which is used throughout the following chapters.

2.2.2 Proposed EGRT System

Figure 2.2 shows the proposed LOR-based EGRT treatment system design.

The system is composed of two major components: two arcs of symmetrically opposed PET detectors and a compact Linac equipped with both a primary collimator and a rapidly switching bMLC. The Linac design is based on current technology [55], with a photon beam energy of 6 MV and a maximum dose rate delivery capability of 800 MU/min. The bMLC system is also based on a current pneumatic-driven system with 64 binary leaves made of 10-cm-thick tungsten. The Linac, collimation system, and PET detectors are mounted together on a fast rotating slip-ring gantry in the same transverse plane. The primary collimator defines the slice-width of the fan beam of radiation and the bMLC selects among individual beamlets within this fan beam in order to direct radiation along the detected LOR paths.

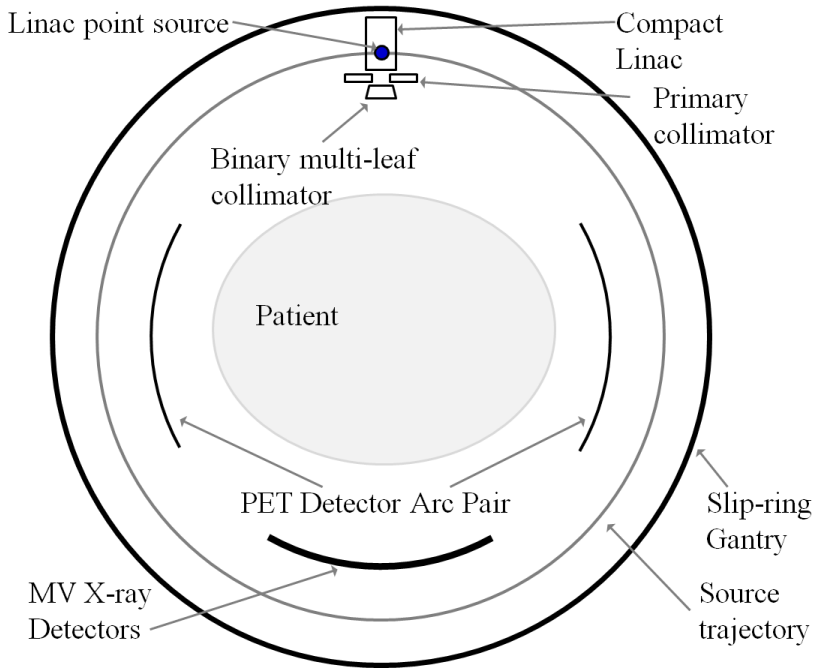

Figure 2.2: Cross-sectional diagram of the proposed treatment system geometry for EGRT. The PET detector arcs are symmetrically opposed, with a span of 2 cm in the longitudinal direction. During treatment, the PET detectors, Linac system and MV x-ray detectors rotate together around the system isocenter on a slip-ring gantry. The patient table moves so that the treatment is delivered helically.

In EGRT, only LORs that meet pre-defined criteria may be responded to, noted as qualified LORs. Pre-defined criteria are specified by the EGRT algorithm and designed to ensure accurate tumor tracking. The Linac responds to the qualified LORs at designated points referred to as *firing positions*, which are equally spaced around the circle. During treatment, the system rotates around the system isocenter with a constant rotation period while the patient is translated slowly through the system bore with a fixed translation speed, resulting in a helical dose delivery scheme. In order to compensate for tumor motion, the rotation period should be small relative to the respiratory cycle or the motion period of the tumor in consideration. In this work, we model a constant rotation period of 1 second. For the proposed system, if the PET activity distribution is relatively uniform and if the PET detector arrays are symmetrically opposed, then the average angular separation between a detected

LOR and the Linac position at any given time is a quarter of a rotation or 90°. With a 1 second rotation period, the expected average lag time is 250 ms. This inherent latency in the system is modeled in simulations to assess the ability of EGRT to compensate for tumor motion.

In this work, we model 256 firing positions around the circle, which is similar to the number of angular bins assigned to LOR data in conventional clinical PET imaging. At a 1 second revolution period, there is a travel time of about 4 ms between firing positions and we assume the bMLC can switch to a new configuration within this travel time to prepare for dose delivery at the next firing position. Current high speed pneumatically driven tungsten leaves can switch as fast as 10-20 ms [106]. If 4 ms cannot be achieved for our proposed system, either a slower rotation rate or fewer firing positions or a combination of both would be employed to ensure the feasibility of the designed bMLC configurations. In this work, bMLC configurations refer to the set of information that defines beamlet responses, including the spatial coordinates of the firing points, the leaf numbers that are opened, and the phase number of the phantom when a leaf is opened (for evaluation purposes). Current medical Linacs operate in a pulsed mode, with a very low duty cycle. Each pulse is on for a few microseconds, with a few milliseconds between pulses, yielding duty cycles on the order of 0.1%. Thus the bMLC will most likely be the main limiting component with respect to timing in the system design.

Figure 2.3 shows a simplified 3D rendering of the treatment geometry, with Figures 2.3 (a) and (b) showing LOR detection and radiation response, respectively.

2.3 Treatment Preparation

Treatment preparation is an important component in any type of RT treatment. For conventional CT-based radiation treatment, it typically includes CT simulation and

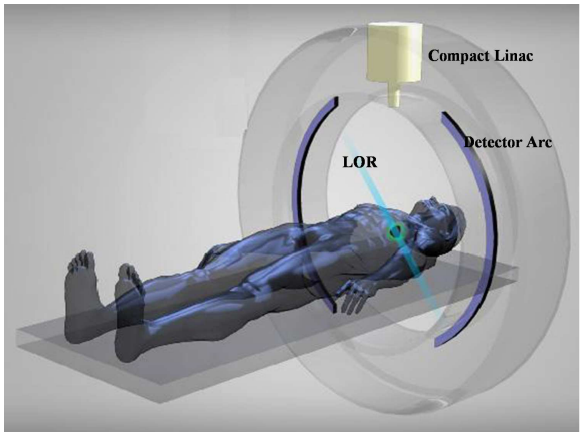

(a) LOR Detection

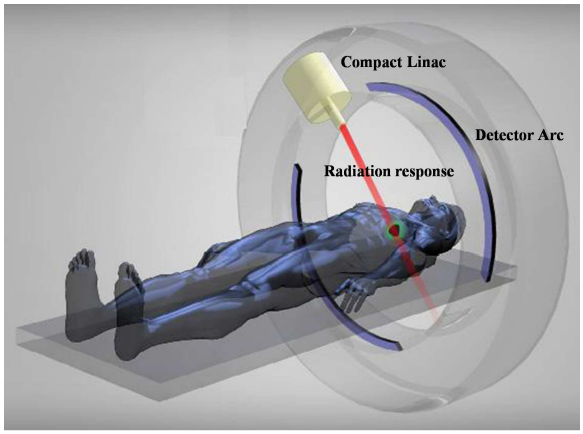

(b) Radiation Response

Figure 2.3: Snapshot of a LOR being detected and radiation response in a simplified 3D rendering of the EGRT system.

patient setup before delivery. CT simulation collects CT data for imaging and treatment planning. Patient setup aims to set up the patient exactly as in the simulation so that the patient receives radiation as planned to the maximum extent.

Due to the introduction of positron emission guidance into RT, simulation needs to be modified accordingly in EGRT. Take the LOR-based EGRT as an example, a PET/CT scan instead of a single CT scan is needed. The standard PET/CT scan protocol applies. Since not every cancer patient receives PET scan during conventional RT treatment, the PET scan may introduce additional cost. However, the PET/CT scan provides more accurate information for the radiation oncologist to

diagnose and stage cancer and monitor radiation therapy, which may dramatically improve the treatment outcome. In addition, a PET scan can also provide essential information for treatment planning.

Patient preparation and setup on the treatment day will also be different from conventional treatments. Since an EGRT treatment depends on the guidance from the distribution of the emission radiopharmaceutical throughout the patient's body, correct preparation is more important than that for conventional therapy. Again take the LOR-based EGRT as an example. On the treatment day, intravenous injection of the positron tracer (e.g. FDG) is required for EGRT treatment. The amount of activity injected will be determined as in the standard PET imaging protocol. After the injection of the radioactive glucose, the patient will be asked to rest quietly for approximately an hour. This allows the glucose to circulate throughout the body and concentrate within the tumor volumes. For a diabetic patient, a nurse may need to check his/her blood sugar level before injecting the radioactive glucose. After the resting period the patient will empty his/her bladder and the radiation therapist will escort the patient into the treatment room to lie down on the treatment couch. The patient will need to lie as still and comfortably as possible for the entire treatment, which may take up to 20 min. Before dose delivery, a PET scan can be done to update the initial treatment plan and a megavoltage computed tomography (MVCT) scan can be used to align the patient to the planned position similarly as in a conventional treatment.

2.4 Radiation Delivery

2.4.1 General Considerations

Radiation delivery in EGRT treatment should fully make use of the emission guidance to ensure that tumor motion is accounted for. For example, in image-based EGRT,

when tumor translation is determined, the radiation beam should be re-aligned accordingly so that it can follow the target motion or alternatively the treatment plan should be transformed to reflect the tumor location change. The beam alignment can be achieved via couch correction or alternatively repositioning of the MLC.

For LOR-based EGRT, as long as the radiation beamlet is backprojected along the detected LORs, basic emission guidance is achieved. However, such a scheme of radiation delivery is not sufficient on its own due to, for example, the existence of background emission signal. Algorithms need to be designed to filter out such background interference. In addition, many other practical issues need to be addressed for the implementation of the radiation backprojection concept such as the rotation speed of the gantry, spatial error tolerance level for backprojection, and the scheme to ensure near real-time tracking. The EGRT basic algorithm, described in the next section, answers the above questions and is used to implement the LOR-based EGRT concept.

2.4.2 Basic EGRT Algorithm

The EGRT algorithm is based on the concept of backprojecting beamlets of radiation along detected LOR paths. An illustration of the proposed algorithm is shown in Figure 2.4. Figure 2.4 (a) shows two distinct events during EGRT treatment: the moment when one LOR is detected (Linac and PET detector arcs are displayed with solid lines) and the moment when this LOR is responded to (Linac and PET detector arcs are displayed with dotted lines).

The sequence of events of the treatment scheme depicted by Figure 2.4 (a) is: (1) PTV is defined, at the tumor contouring stage, to contain the GTV motion, with additional margins as in the case of conventional radiation therapy. The patient is administered with a PET radiotracer and undergoes setup and registration using MVCT images after the patient is positioned on the table to align the PTV. MVCT

can provide sufficient image quality for tumor identification and patient setup [31]. (MVCT x-ray detectors and patient table are shown in Figure 2.2 but not in Figure 2.4 for simplicity). (2) The EGRT system performs in-plane rotation continuously with a constant period on the slip-ring gantry while the patient bench undergoes through-plane translation for a helical treatment. (3) LORs are detected. (4) Assuming this shown LOR meets certain criteria specified below, when the Linac arrives at the firing position for this LOR, the corresponding collimator leaf is opened, resulting in a radiation beamlet delivered along this particular LOR path. LOR detection and selective LOR response (steps (3) and (4)) are repeated to achieve the full helical treatment covering the PTV.

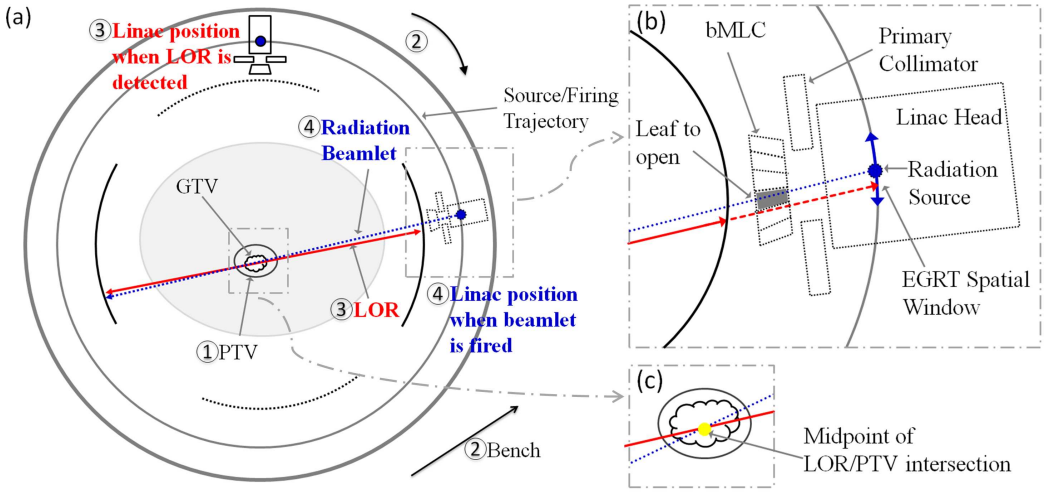

Figure 2.4: (a) shows the process of LOR detection and response by the bMLC selected beamlets of radiation. (b) and (c) are enlarged views of the corresponding blocks as labeled in (a). (b) shows the EGRT spatial window, one of the LOR response criteria of the basic EGRT treatment scheme. The LOR (red solid line) that intersects with the source trajectory at a point that falls within the EGRT spatial window (blue arc) is qualified for radiation response. (b) and (c) together show the collimator leaf (shaded) closest to the line that connects the source and the midpoint of the LOR-PTV intersection (yellow point in Figure 2.4 (c)).

The margins added to the CTV to define the PTV account for tumor location uncertainties including intrafractional/interfractional motion and setup errors, such that the tumor is always inside the PTV during treatment. The PTV is assumed

to be static throughout the treatment and provides an approximate region in which the GTV is contained. Only the LORs intersecting the PTV are used for treatment guidance, so that the EGRT system can track and locate the GTV for dose delivery with minimal interference from background emissions.

Besides the PTV criterion, other pre-defined criteria are also used in EGRT to optimally use the LORs in guiding radiation beamlets, which include: the EGRT time window and the EGRT spatial window. To ensure nearly real-time tracking, the Linac only responds to LORs that are detected within a short period of time relative to the current firing time, referred to as the EGRT time window. In this work, the EGRT time window is fixed to be 500 ms. In addition, the LORs whose intersection with the source trajectory is more than a pre-determined distance away from the closest firing position are also excluded to minimize azimuthal error. This small tolerance is referred to as the EGRT spatial window, specified using angular separation along the source/firing trajectory (see Figure 2.4 (b)).

It should be noted that due to this spatial tolerance, beamlets may not be back-projected exactly along the corresponding LOR paths. Figure 2.4 (b) shows, in an enlarged view, the deviation of the actual delivery path (blue dotted line) from the detected LOR path (red solid/dashed line). The actual path of delivery is selected along the line that passes through the source point and the midpoint of the LOR-PTV intersection, as illustrated together by Figures 2.4 (b) and (c). Figure 2.4 (b) also illustrates the LOR passing the EGRT spatial window criterion (blue arc), as well as the shaded leaf that will be opened. Note that at each firing position, a set of leaves may be opened for a set of qualified LORs. In all simulations presented in Chapter 3, the EGRT spatial window is fixed at ± 0.5 degrees. We find that the average leaf openings for each of the 256 firing positions, accumulated over all rotations within a 2 mm slice, is within a range of 2-6 for the PTV sizes used in the 4D patient model studies presented in section 3.1.

2.5 Treatment Planning

2.5.1 General Considerations

Treatment planning extends the capability of achieving a desired dose distribution and is crucial to any treatment modality. In current RT practice, treatment planning is mainly CT based and it typically does not take into account any tumor biology information or tumor response to radiation. However, biological information can significantly help with the treatment planning process. For example, PET imaging can improve the accuracy and consistency of tumor volume delineation. Also, the current most widely used IMRT inverse planning techniques typically try to produce a homogeneous target dose under the assumption of uniform biology within the target volume. However in reality, the spatial biological distribution (e.g. radiosensitivity, tumor proliferation rate, functional importance) in most tumors is heterogeneous. Such information should be taken into account to produce more effective and personalized treatment plans for better treatment outcomes. Fortunately, incorporating emission imaging into treatment planning has been reported possible.

The development of a treatment planning system that fully incorporates biological information is beyond the scope of this dissertation and will be a major focus in the future development of EGRT. Instead, this work mainly focuses on development of a scheme to incorporate a conventional planning technique into this new type of emission guided treatment. For image-based EGRT, since the emission guidance is used for tumor tracking purposes and not integrated with radiation delivery, the same conventional IMRT treatment planning can be directly applied. For LOR-based EGRT, the emission guidance links together tumor tracking and dose delivery in a non-conventional way. Conventional IMRT planning cannot be directly incorporated and needs to be modified based on the characteristics of LOR-based radiation delivery. Chapter 5 discusses a complete treatment planning scheme based on the current IMRT planning technique. In the next section, we discuss the method of modulating dose

delivery in LOR-based EGRT, which reveals the basic principle for the full planning scheme.

2.5.2 EGRT Modulation

The basic EGRT algorithm enables dynamic tumor tracking but has limited ability to optimize the dose distribution given the treatment planning dose constraints. However, the ability to modulate the dose distribution according to specific treatment goals is highly desirable. We propose here EGRT modulation methods in addition to the basic EGRT treatment scheme to demonstrate the potential of dose planning. Since the basic EGRT algorithm translates all detected LORs into a set of bMLC configurations, i.e. a sequence of leaf openings, we use modulation of actual leaf opening probabilities to achieve EGRT modulation. In the future, the beam intensity and/or duration for each leaf opening could also be modulated to provide more flexibility for dose control.

Although the LOR data is randomly generated so that the beamlet radiation response is inherently stochastic, modulation of the response probabilities is based on deterministic weights from the planning process. In the proposed helical geometry, with fast rotation, slow translation and small PET detector extent in the longitudinal direction, the LORs are approximately detected and responded to in a series of 2D slices. This particular *3D parallel* geometry samples the delivery space into a stack of 2D fan-beam sinograms, referred to as sinogram space. Each bin in sinogram space corresponds to a spatial orientation of a beamlet response path for a specific slice. Every detected LOR path can then be mapped into one of the sinogram bins according to a nearest neighbor approximation.

Under such geometric approximation, the traditional inverse planning formulation can be adapted for EGRT as

$$minimize \quad \|D \cdot \Sigma \cdot \Psi(b_{woa}) - d\| \tag{3}$$

$$subject\ to \quad 0 < \Sigma < 1 \tag{4}$$

where d is the prescribed 3D dose distribution in vectorized form, and b_{woa} is the expected distribution of the number of LORs that will be detected in sinogram space given the tracer activity distribution and EGRT treatment settings (i.e. treatment time and table speed) in the absence of attenuation. Ψ, the attenuation operator, represents the change made to b_{woa} by the attenuation effect. $\Psi(b_{woa})$ is in the diagonal matrix form whose diagonal elements are the number of LORs in sinogram space after attenuation while Σ is the modulation matrix, of the same size, whose diagonal elements specify the probability of opening a leaf for a particular sinogram bin. Σ is analogous to the intensity modulation parameter in conventional IMRT, and is what must be determined to solve the inverse optimization problem. Each column of matrix D is a beamlet kernel, corresponding to the 3D dose distribution imparted by one unit beamlet. Based on this formalism, we develop attenuation correction and integrated boost schemes as two specific EGRT modulation applications to demonstrate its feasibility.

2.5.2.1 Attenuation Correction

In PET imaging, attenuation of the annihilation photons within the subject leads to lower signal along highly attenuating paths. If not accounted for, the reconstructed image will reflect this attenuation bias with lower activity estimates within the attenuating regions, as illustrated in Figure 1.11. Attenuation correction is now routine in PET/CT imaging by using the CT scan to estimate the attenuation map of the subject at photon energies in the PET range[1], followed by using this estimate to weight LORs according to the attenuation along their individual paths.

[1] i.e. 511 keV

In EGRT, the same issue arises where the LOR detection rate is inversely proportional to the attenuation of the two annihilation photons. Attenuation can be highly non-uniform across all directions, resulting in non-uniform LOR detection rates and therefore a non-uniform radiation response distribution. To correct for this effect, the analytic solution could be approximated from Eqn. 3 as $\Sigma \approx \Psi^{-1}$. That is, the attenuation effect can be removed by applying a modulation probability vector in sinogram space that is inversely proportional to resultant LORs detection rate. Specifically, the attenuation, i.e. line integral, is first pre-calculated using Siddon's algorithm [90] from the planning patient CT images for all sinogram bins. The leaf opening probability is a value between 0 and 1, calculated from the attenuation of the associated bin. Let us denote the maximum attenuation across all bins as a_{max} and jth bin as a_j. Since the maximum attenuation would yield the smallest number of leaf openings, the opening probability should be preserved as 1. The jth bin should have an opening probability of,

$$p_j = e^{-a_{max}+a_j} \tag{5}$$

Depending on the strength of the attenuation, the leaf open probability for each bin will range from 0 to 1 to compensate for that bin's LOR detection rate. Figure 2.5 illustrates how the response to an individual LOR is adjusted when attenuation correction modulation is enabled.

2.5.2.2 Integrated Boost

Target dose boosting is often utilized in current radiation therapy to ensure that the target receives adequate dose [108]. In an integrated boost scheme, a sub-volume within the PTV is prescribed a higher dose than the remaining PTV. Note that the sub-volume is defined at the tumor contouring stage and is assumed static during the treatment as it is defined relative to the PTV. To achieve a target dose boost

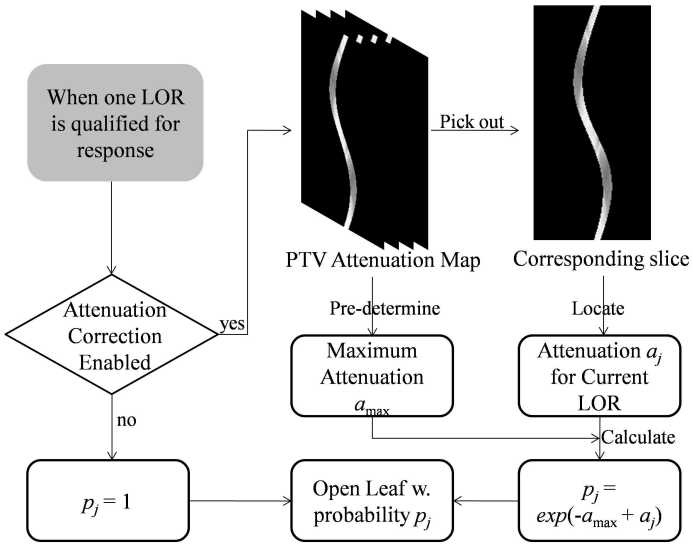

Figure 2.5: An example illustration of EGRT modulation in the case of attenuation correction. The workflow starts with the shaded module. When one LOR is qualified for response, i.e. it passes the three criteria of the basic EGRT algorithm, the leaf will be opened if the attenuation correction algorithm is not enabled. However, if the modulation algorithm is enabled, the open probability will not be 1. Rather, this LOR will first find its corresponding bin in terms of its spatial orientation in the pre-calculated attenuation map and the response probability of this LOR, p_j, is determined as shown. Note that since only LORs that intersect the PTV may be responded to, the attenuation map is only calculated for the PTV region.

in EGRT, the same boost region is constructed within the PTV. Using Eqn. 3, we can construct a modulation matrix Σ whose diagonal elements corresponding to the boost region (i.e. in the beamlet directions which intersect the boost sub-volume) are larger than those which correspond to the non-boost PTV region. In this work, the ratio of the boost and non-boost modulation values (diagonal elements of Σ) is the ratio of the prescription dose to these two regions and the modulation matrix is scaled to a range of [0 1]. In the case where both modulation methods are applied, the final modulation matrix is obtained by component-wise multiplication of the individual modulation matrices from each method.

CHAPTER III

EGRT APPLICATIONS

Due to the novel approach of delivering radiation based on biological guidance, EGRT can have many applications. For example, EGRT is a good option to implement stereotactic treatments (or ablative radiotherapy). Ablative radiotherapy is a concept to improve tumor control by delivering small numbers of large doses over shorter periods [73], as mentioned in section 1.1.4. In early-stage cancers such as lung and prostate, current ablative radiotherapy has shown excellent local control rates [96, 6, 51]. Control rates achieved in the lung with ablative radiotherapy are rivaling those that can be obtained with surgery [35, 72]. However, ablative radiotherapy requires precise localization of the tumor to avoid irradiating nearby critical structures. As previously mentioned, this precise localization is challenged by the need to account for the movement of tumors in the body caused by factors such as respiration. EGRT can therefore provide a feasible solution in this particular case.

In this chapter, we mainly discuss three major EGRT applications: tumor tracking, tracking of multiple targets, and treatment of non-PET-avid volumes.

3.1 Tumor Tracking

As introduced in section 1.2, treatment uncertainties especially those due to tumor motion and patient setup error significantly limit the effectiveness of RT treatment. Hence, one of the most important applications of EGRT is to effectively and practically tackle the tumor tracking problem. This is also the major motivation that has inspired the EGRT concept.

In this section, we aim to demonstrate EGRT's superior capability of tumor tracking using carefully designed simulation studies. Typical intrafractional lung tumor

motion and interfractional setup errors are simulated in various situations. They are major sources of tumor location uncertainty and also the most commonly observed cancer treatment uncertainties in current clinical practice. A simple water phantom, physical phantom experiments, and a 4D digital patient model have been used for demonstration. The simulation workflow will first be discussed, followed by evaluation details pertaining to specific simulation studies and associated results. Note that the simulation workflow with related simulation parameters presented below (i.e. section 3.1.1) takes the study of the digital patient model as an example for illustration. The workflow for the studies of water phantom and physical phantom experiments is similar. Their simulation details including simulation parameters are listed in their own sections.

3.1.1 Simulation Workflow

An anthropomorphic digital patient model, the 4D XCAT phantom [85], is used in our studies for demonstration. Both cardiac and respiratory motion are simulated. The phantom consists of an attenuation distribution and an activity distribution with the same anatomical geometry, and it is constructed based on real patient anatomy and typical radiotracer uptake distributions measured in nuclear medicine imaging. The activity distribution specifies how the radioactive tracers are distributed inside the phantom, and the attenuation distribution is used in the calculation of radiation dose distributions. The XCAT phantom used has a voxel resolution of 2 mm for all simulation studies included in this work. Scenarios of lung and prostate cancers are simulated. Other major XCAT phantom simulation parameters can be found in Table 3.1.

To simulate a dynamic EGRT treatment and examine the feasibility of EGRT, the following simulation workflow that completely simulates the proposed EGRT dynamic treatment has been designed and is shown in Figure 3.1.

Table 3.1: Major XCAT phantom simulation parameters

Scenario	Parameter	Value	Parameter	Value
Lung	Respiration period	4.2 s	Phantom size	$256 \times 256 \times 35$
	Respiration phases	12	Voxel resolution	2 mm
	GTV size	9.40 cm^3	Sinogram bin size	$256 \times 64 \times 35$
	PTV size	153.90 cm^3	Tracer uptake ratio	8 : 0.5 : 1
Prostate	PTV margin	6 mm	Phantom size	$256 \times 256 \times 39$
	Setup error	6 mm	Voxel resolution	2 mm
	GTV size	33.27 cm^3	Sinogram bin size	$256 \times 64 \times 39$
	PTV size	71.73 cm^3	Tracer uptake ratio	8.5 : 1

The LOR detection and dose delivery processes are separately simulated for convenience. Both the activity and attenuation XCAT phantoms are input into the Geant4 Application for Tomographic Emission (GATE) package (see Appendix A.0.2). The output coincidence data are stored in *list-mode* form. In this format, each recorded coincidence event includes its timestamp and 3D coordinates of the two LOR endpoints. Note that these data contain both the scattered and random coincidence events. Since the GATE simulation adopts the full ring geometry, the events that do not intersect the actual PET detector arcs in the proposed system are discarded. The filtered coincidence list forms the LOR queue for dose delivery.

Dose delivery estimation involves two processes: the determination of bMLC configurations and subsequent Monte Carlo dose calculation. When dose delivery starts, the Linac rotates around the circle and goes through different firing positions. At each firing position, it scans through the current LOR queue and checks whether each individual LOR meets the three necessary criteria. If at least one LOR is determined to be eligible for response, the EGRT modulation algorithms such as attenuation correction, incorporation of planning, or others may be enabled to determine its response probability. The final probability is used as a coin-flip for each leaf opening. Once all firing positions have been processed, the final set of bMLC configurations is obtained and subsequently the voxel based Monte Carlo (VMC++) (see Appendix A.0.3) dose calculation engine calculates the final dose map for evaluation.

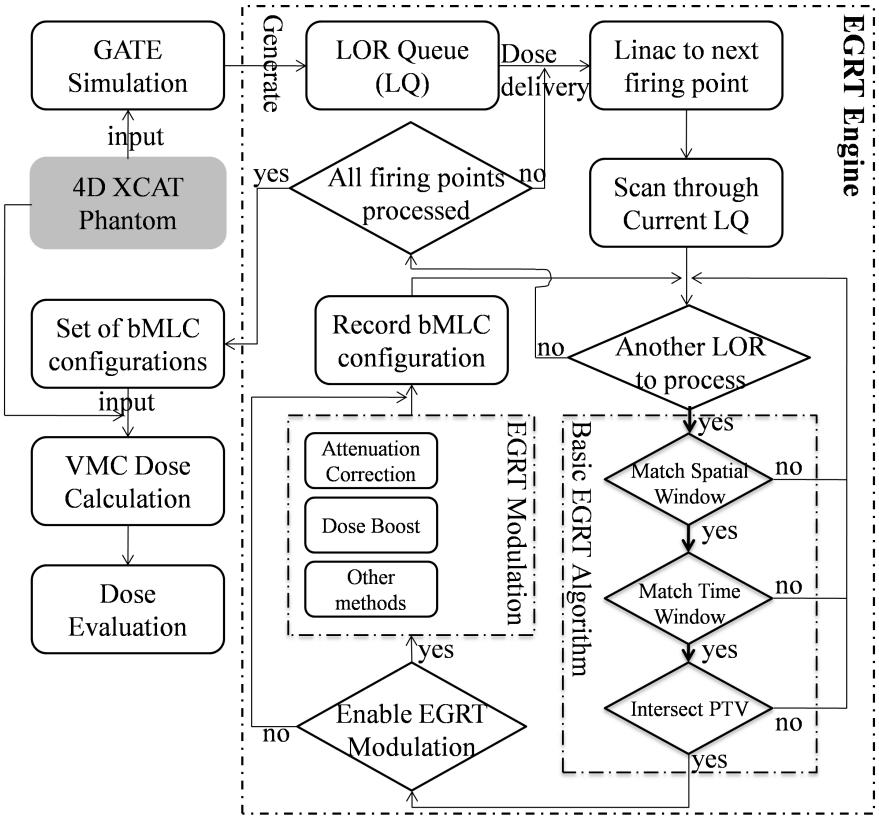

Figure 3.1: The simulation flow chart (starting from the shaded module). In an EGRT treatment, there are two major processes to simulate: positron emission and dose delivery. For simulation of the positron emission and detection process, the 4D XCAT phantom is input into the GATE package to obtain the LOR data for dose delivery. The LOR data are used as input for the basic EGRT algorithm and optional EGRT modulation algorithms such as attenuation correction and integrated dose boost. The resultant set of bMLC configurations is used as inputs to the VMC++ dose calculation engine. The components that enable dynamic EGRT delivery are collectively referred to as *EGRT Engine*, as labeled in the figure.

In the case of a moving phantom, the dose is first estimated separately for each phase of motion. To calculate the total dose of a moving structure, dose maps of different phases are registered to the same reference phase through rigid image registration. The multiple dose maps are then summed to produce a *point-of-view* map relative to the moving structure. A detailed description of the dose evaluation scheme for a moving phantom is shown in Figure 3.2.

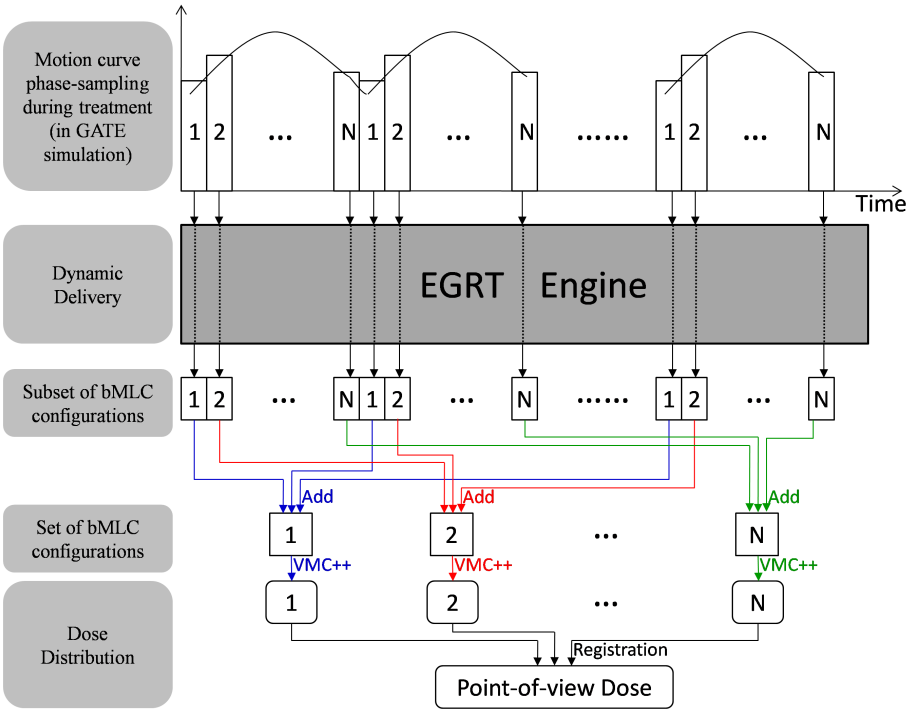

Figure 3.2: The dose evaluation scheme for a moving phantom. The periodic motion curve is sampled into N phases. The number (i.e. 1, 2, $\cdots$, N) in this figure indicates the corresponding phase index.

The EGRT engine refers to our dynamic EGRT delivery algorithm used to determine the qualified LOR responses. The included components of the EGRT engine are labeled in the simulation workflow (Figure 3.1). While the gantry and couch are constantly moving in one direction, subsets of bMLC configurations are generated continuously until the treatment ends. Note that these subsets of bMLC configurations are phase-labeled, i.e. each subset belongs to a particular phase. To evaluate the dose that has been accumulated in each phase during the whole treatment, the set of bMLC configurations for each phase is obtained as a summation of subsets of bMLC configurations that correspond to that particular phase. To evaluate the dose accumulated for a specific moving structure (e.g. GTV) during the whole treatment, rigid image registration is used.

A summary of the main EGRT simulation parameters is shown in Table 3.2[1].

Table 3.2: Major EGRT and GATE simulation parameters

Category	Parameter	Value	Parameter	Value
EGRT	Detector extent	2 cm	iso leaf aperture(x-y)	0.5 cm
	Detector coverage	180° arc	iso leaf aperture (z)	1 cm
	PET ring radius	50 cm	EGRT spatial window	±0.5° arc
	Rotating frequency	1 Hz	EGRT time window	500 ms
	Linac radius	60 cm	Helical pitch	0.2
	Background activity	3 kBq/cc	Radiotracer	FDG
	Collimator radius	50 cm	Firing positions	256
	Collimator leaves	64		
GATE	Version	V5.0.0.p01	Light decay time	40 ns
	Coincidence window	10 ns	Energy resolution	0.26
	Scatter threshold(keV)	350,650	Coincidence policy	TWG

Choices of parameters take into account typical engineering design considerations and actual clinical uptake of the FDG radiotracer [19, 40]. For performance evaluation, we compare the proposed EGRT method and a conventional helical IMRT method without optimized intensity modulation. Both simulations use nearly the same system settings (i.e. the same MLC system, the same number of 256 firing positions and the same firing geometry with a more suitable helical pitch). The main difference is that EGRT opens the leaves that correspond to qualified LORs from the tumor, while the conventional treatment opens the leaves that intersect the PTV without tracking the tumor position.

3.1.2 Preliminary Study: Water Phantom

3.1.2.1 Simulation Details

The preliminary water phantom study is conducted for the very initial concept and feasibility demonstration. In this study, both the hot source and the warm background are modeled as water. Simulations included three cases: 1) No motion; 2) Target in-plane (x) motion; 3) Target through-plane (z) motion. The simulated list-mode data

[1]TWG = takeWinnerofGoods.

are input into the EGRT simulation framework, using a PTV corresponding to the specific motion case. Table 3.3 outlines the parameters for the simulations.

Table 3.3: Simulation parameters for water phantom study.

Parameter	No Motion	X Motion	Z Motion
Target diameter (cm)	3.7	3.7	3.7
Target activity (kBq)	24	24	24
Background diameter (cm)	20	20	20
Background activity (kBq)	3	3	3
Motion amplitude (cm)	0	1.0	0.65
Motion period (s)	0	3.7	4.84
PTV diam/axial extent (cm)	5/6	6/6	5/6
Rotation period (s)	1	1	1
PET axial coverage (cm)	2	2	2
PET circular coverage (%)	50	50	50
bMLC x/z leaf at iso (mm)	5/10	5/10	5/10
Firing positions	256	256	256
LOR angular threshold (°)	±0.5	±0.5	±0.5
Lag threshold (ms)	500	500	500
Treatment time (s)	600	600	600
Table speed (cm/s)	0.01	0.01	0.01

As a comparison, the same cylindrical PTV in each case is uniformly irradiated using a helical IMRT delivery scheme. The point-of-view dose maps for the EGRT and IMRT methods are both normalized with the same integral dose to the phantom. The dose volume histogram (DVH) is calculated based on the point-of-view dose maps to compare the two methods for each of the motion cases.

3.1.2.2 Results

The GATE simulations resulted in 91677, 105669 and 91353 beamlet responses for the no motion, x-motion and z-motion cases, respectively. After 600 s of treatment, this translates to, on average, between 150 and 175 beamlet responses per second, or in this case per rotation. Figure 3.3 depicts dose maps of three different phases of motion for both of the simulated motion cases. Dose concentration in the moving target can be seen in both the x-motion and z-motion scenarios.

Figures 3.4, 3.5, and 3.6 show GTV point-of-view dose maps assembled from all

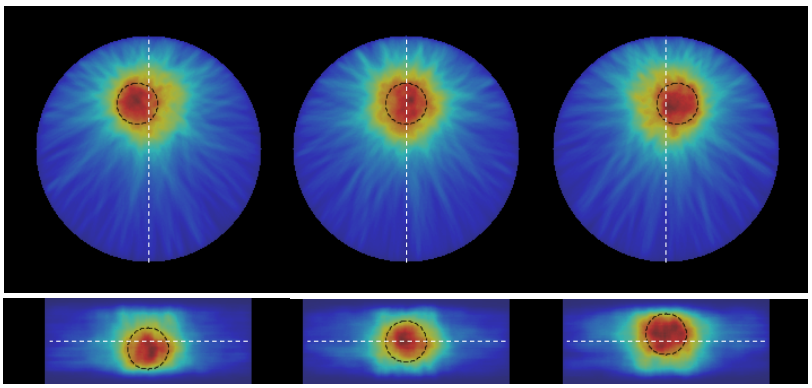

Figure 3.3: (Top) Axial dose maps for three different phases for the simulated x-motion case. (Bottom) Coronal dose maps of three phases from the z-motion case. The dashed black lines indicate the GTV position. Dashed white lines are overlaid for positional reference.

12 simulated motion phases for each scenario, as well as the associated DVH curves comparing EGRT with IMRT. In all cases, there is a peaking of dose in the center of the GTV, discussed below. However, even with this inhomogeneity, there is a 17%, 21% and 17% relative increase in dose to 95% of the GTV for the static, x-motion and z-motion scenarios, respectively, when comparing the EGRT and IMRT methods normalized for the same integral dose to the phantom (denoted as healthy tissue).

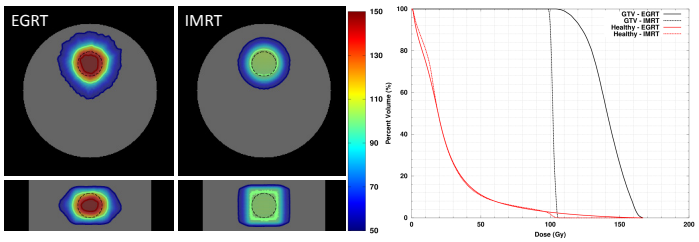

Figure 3.4: (Left) Axial and coronal point-of-view dose maps for the GATE simulated case with no motion comparing EGRT and IMRT methods. The dashed black lines indicate the GTV position. (Right) Associated DVH curves.

3.1.3 Preliminary Study: Physical Phantom Experiments

3.1.3.1 Simulation Details

Phantom experiments are conducted using a GE Discovery PET/CT scanner (GE Healthcare, Waukesha, WI). A cylindrical phantom and six spherical inserts (37, 28,

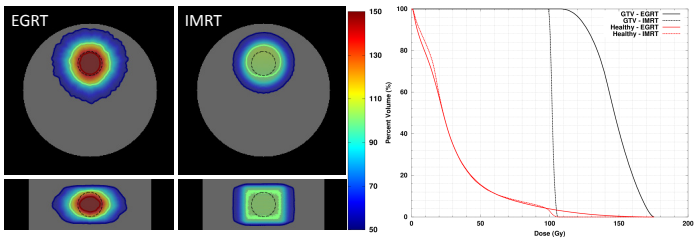

Figure 3.5: (Left) Axial and coronal point-of-view dose maps for the GATE simulated x-motion case comparing EGRT and IMRT methods. The dashed black lines indicate the GTV position. (Right) Associated DVH curves.

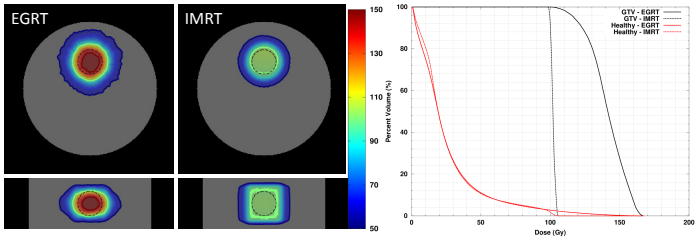

Figure 3.6: (Left) Axial and coronal point-of-view dose maps for the GATE simulated z-motion case comparing EGRT and IMRT methods. The dashed black lines indicate the GTV position. (Right) Associated DVH curves.

22, 17, 13, and 10 mm in diameter) were filled with FDG for a target-to-background ratio of 8:1 with activity level based on 10 mCi of injected activity for a 70 Kg subject. The phantom is affixed to a motion stage and situated inside the scanner (Figure 3.7).

The motion stage used is the 4D Phantom that was developed at Washington University as a quality assurance (QA) tool designed to position a radiological phantom with sub-millimeter accuracy [62]. It consists of two parts. One part is a 3D motion platform that can move a phantom independently along all axes to simulate internal 3D motion of a target. The other part is a 1D motion stage that moves an optimal marker vertically to simulate external abdominal respiratory motion. The motion stage is programmed with breathing trajectories acquired from volunteers using the Varian RPM system. The RPM system employs an external optical marker on the abdomen that is tracked by a camera. This system is used to acquire a one-dimensional breathing trajectory from a volunteer who is instructed to breath normally. We denote this as the *free breathing* scenario. For better comparison with

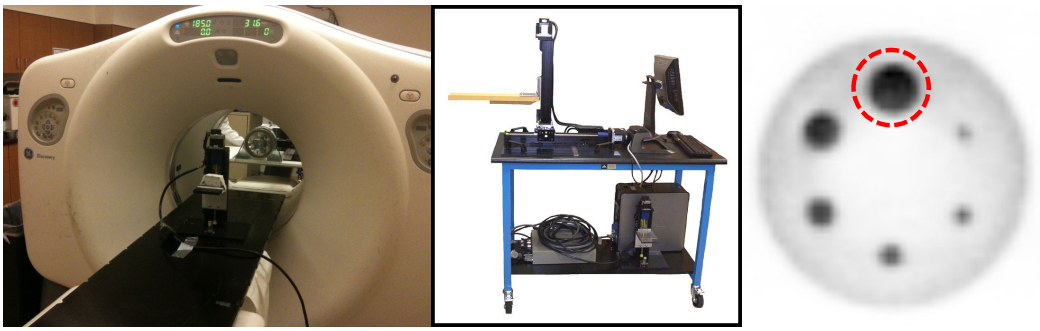

Figure 3.7: FDG phantom experiment setup. (Left) GE Discovery PET/CT system. (Middle) 4D Phantom (image from http://radonc.wustl.edu/–md/pparikh/4dphantom.html). (Right) FDG phantom reconstruction. The dashed line is a cylindrical planning target volume (PTV) which includes the motion trajectory of the largest sphere.

the GATE simulations, a periodic motion trajectory was constructed based on the free breathing motion path by calculating an average period and amplitude. We denote this motion pattern as the *periodic breathing* scenario. The two motion trajectories are depicted in Figure 3.8.

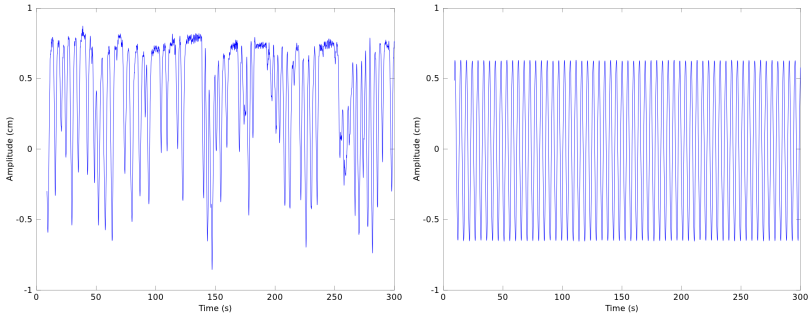

Figure 3.8: (Left) Free and (Right) Periodic breathing motion trajectories used in the phantom experiments. Peak exhalation, which reflects the lowest point of the abdominal marker during measurement, is defined to be positive in this case to correlate with the positive z translation of the motion stage.

The recorded vertical motion from the RPM system is used to drive the motion stage in a purely superior/inferior (z) direction. After FDG filling, the PET phantom is secured to the 3D portion of the stage and the stage motion is either turned off or programmed with the periodic or free breathing trajectories. The 1D portion of the stage is also programmed with the corresponding scenario. The PET data are

recorded in raw list-mode form so that the timestamp of each recorded LOR event is known. The RPM system is used to track the 1D motion stage so that triggers from the RPM system could be synchronized with the list-mode data from the PET scanner. The raw LOR list-mode data are not corrected for scatter or randoms. The list-mode data are used as input into the EGRT simulation framework described above.

A cylindrical PTV is designated around the largest 37 mm sphere and fully contains its motion trajectory in the z direction (see Table 3.4 for the experimental parameters including PTV sizes).

Table 3.4: Simulation parameters for physical phantom experiments.

Parameter	No Motion	Periodic Z	Free Z
Target diameter (cm)	3.7	3.7	3.7
Target activity (kBq)	41.44	41.44	41.44
Background diameter (cm)	20	20	20
Background activity (kBq)	5.18	5.18	5.18
Motion amplitude (cm)	0	0.65	0.875
Motion period (s)	0	4.84	N/A
PTV diam/axial extent (cm)	5/6	5/6	5/7
Rotation period (s)	1	1	1
PET axial coverage (cm)	2	2	2
PET circular coverage (%)	50	50	50
bMLC x/z leaf at iso (mm)	5/10	5/10	5/10
Firing positions	256	256	256
LOR angular threshold (°)	±0.5	±0.5	±0.5
Lag threshold (ms)	500	500	500
Treatment time (s)	600	600	600
Table speed (cm/s)	0.01	0.01	0.01

The EGRT algorithm uses this PTV as a mask, rejecting all LOR events that do not intersect the PTV. Uniform coverage of the same PTV is simulated for comparison. The VMC++ simulation of the EGRT system calculates the resultant dose distribution in a cylindrical water phantom with the same dimensions as the PET phantom. The point-of-view dose map is estimated by calculating 12 dose maps for 12 distinct motion phase bins that are based on displacement rather than time. 12 displacement-based bins in each of the free and periodic motion scenarios are spaced

uniformly between the minimum and maximum trajectory displacements across the full time course. The free breathing scenario has bins spanning 1.75 cm peak-to-peak, while the bins for the periodic case span 1.3 cm peak-to-peak. The dose maps for each bin are shifted based on their displacement relative to a reference bin and then summed to produce a single point-of-view dose map. The associated DVH curves are calculated based on the point-of-view dose maps for the target volume and full phantom.

3.1.3.2 Results

The phantom experiments resulted in 154142, 184979 and 243842 beamlet responses for the no motion, periodic and free-breathing scenarios, respectively. The differences in the number of counts is likely due to the differences in the delay between FDG filling and the starting of experiment for each scenario. After 600 s of treatment, this translates to between 250 and 400 beamlet responses per rotation.

Figures 3.9, 3.10 and 3.11 depict the dose distributions for the EGRT and IMRT (uniform PTV coverage) methods from the moving spherical target's point of view, with associated DVH curves. As in the simulation results, the dose peaks in the center of the target for the EGRT method, which yields a 18%, 17%, and 23% relative increase in dose to 95% of the target volume compared with uniform PTV coverage IMRT method when both are normalized for the same integral dose to the phantom.

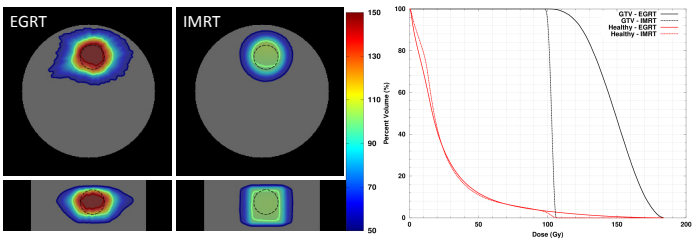

Figure 3.9: (Left) Point-of-view dose maps for the phantom study no-motion case comparing EGRT and IMRT methods. The dashed black lines indicate the GTV position. (Right) Associated DVH curves. The arrow indicates relatively higher dose in the direction of the second largest sphere.

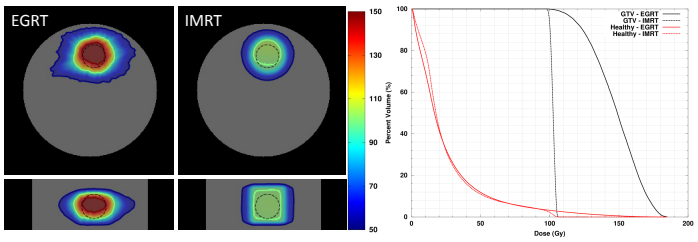

Figure 3.10: (Left) Point-of-view dose maps for the phantom study periodic breathing scenario comparing EGRT and IMRT methods. The dashed black lines indicate the GTV position. (Right) Associated DVH curves.

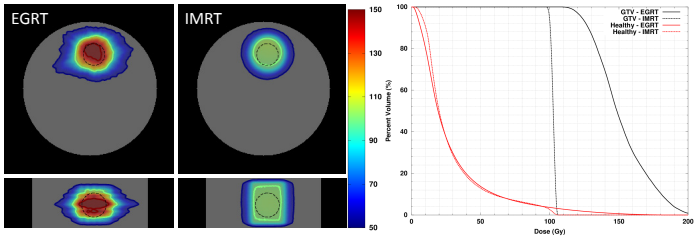

Figure 3.11: (Left) Point-of-view dose maps for the phantom study free breathing scenario comparing EGRT and IMRT methods. The dashed black lines indicate the GTV position. (Right) Associated DVH curves.

3.1.4 Preliminary Study: Discussion

We have demonstrated a proof of principle for responding to individual PET emissions with radiation beamlets along the emission paths. In this section we discuss limitations of the current work, as well as areas of future work.

The observed dose peaking in the center of a uniformly avid target can be explained by the backprojection effect. There are more LORs that intersect the center of the GTV than the edge, as the detected LOR rate spatial profile is the projection of the sphere onto the PET detector array. In filtered-backprojection image reconstruction, the peaked projection is first filtered so that the backprojected image intensity of the GTV is reflective of its original activity distribution. EGRT, however, results in radiation backprojection (no filtering) along the LOR paths and therefore preserves the peaking from the original projection.

Due to the dose peaking effect, one may think that a more fair comparison between

the IMRT and EGRT methods would be to integrate a boost in the IMRT plan, as is commonly done for stereotactic hypofractionated treatments. However, the same deterministic boost can be applied to the EGRT plan. In other words, all planning weights that are a result of IMRT planning should be incorporated into the EGRT plan for a fair comparison. In the following example, the IMRT boost is implemented by boosting a sub-volume in the PTV, which we denote as the Boost volume, that has the same size as the GTV and receives twice the intensity as the non-Boost portion of the PTV. We incorporate this same boost in the EGRT scheme by assigning a probability to beamlet-responses based on their intersection with the PTV and Boost volumes. Beamlets that intersect the Boost volume were delivered with twice the probability as those that intersect the PTV volume but do not intersect the Boost volume. Figure 3.12 depicts the dose maps and DVH curves comparing the IMRT-Boost and EGRT-Boost methods for the case of the GATE z-motion simulation.

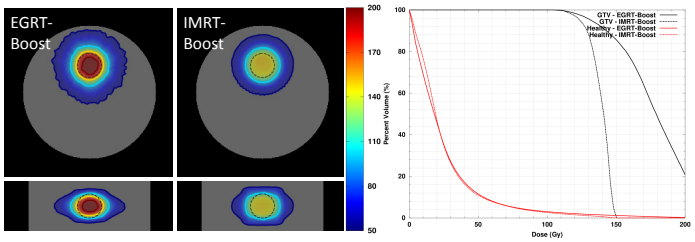

Figure 3.12: (Left) Axial and coronal point-of-view dose maps for the GATE simulated z-motion case comparing EGRT and IMRT methods with a simultaneous integrated boost. The dashed black lines indicate the GTV position. (Right) Associated DVH curves.

In this case, both scenarios have been normalized for the same absolute integral dose to the phantom as the non-boost cases for a direct comparison. The IMRT-Boost method achieves a 24% and 40% increase in dose to 95% and 50% of the GTV volume, respectively, compared to the original IMRT method. The EGRT-Boost method achieves a 32% and 76% increase in dose to the GTV compared to the original IMRT method. The relative gain of EGRT over IMRT is not as high as in the non-boost cases, likely due to the fact that the boost volume largely overlaps the

GTV volume in all phases of motion and therefore the deterministic benefit of the treatment plan is competing with EGRT's stochastic benefit. Nonetheless, it can be seen that IMRT planning weights can be employed within the EGRT framework to take advantage of a priori information.

In all phantom experiments presented above, there is an increase in dose in the direction from the largest sphere to the second largest sphere (indicated by the arrow on Figure 3.9). This is due to radiation delivery along LOR paths that originated from the second largest sphere but whose paths also intersect the PTV. As the EGRT algorithm is blind to the origin of each LOR, all LORs that intersect the PTV can be responded to, irrespective of their source. This effect can be mitigated in future work through prior knowledge of the PET distribution of the subject.

An interesting effect can be seen in the free breathing scenario (Figure 3.11). A ripple pattern of the dose distribution appears in the longitudinal (z) direction. At first this was thought to be due to the reported *thread* effect of a helical delivery system [16]. The thread effect is known to be strongly dependent on the pitch of the treatment delivery, where the pitch is defined as the number of rotations per table traversal of a slice-width. However, when the pitch was varied in the free breathing scenario there was little change in the ripple pattern. It is hypothesized that the observed ripple effect in this case is due to the erratic free breathing motion path. The full analysis of this effect will be the subject of future work. Even in its presence, the DVH curves for the free breathing scenario demonstrate a 23% relative increase in dose to 95% of the target volume when compared with the IMRT approach.

Oncologic applications of PET continue to evolve as new radiotracers are developed that target various aspects of cancer biology and function. PET is a molecular imaging modality that is able to detect and image a broad range of biological processes. ^{18}F-Fluorodeoxyglucose (FDG)-PET, which measures the metabolic activity of glucose, is currently the gold standard in noninvasive cancer detection, with higher

sensitivity and specificity than CT or MRI across a broad range of cancers [32]. In addition to FDG for metabolic activity, other PET radiotracers have been used to image cellular proliferation (^{18}F-fluorothymidine [26]), hypoxia (^{18}F-fluoromisonidazole [71, 76]), and amino acid transport (^{18}F-fluoroethyltyrosine [36], 18F-FACBC [84]). These imaging applications can potentially translate into PET-based treatment where EGRT becomes a tool to achieve biologically adaptive therapy.

3.1.5 Preliminary Study: Conclusions

The feasibility of emission guided radiation therapy has been demonstrated using the principle of radiation backprojection along detected LOR emission paths. Dose peaking in the center of a PET-avid volume is a consequence of the technique, and a thread-like effect is observed in the free breathing scenario. However even in the presence of these inhomogeneities the simulations and experiments performed in this study have demonstrated at least 15% relative increase in dose to 95% of the target volume when compared to uniform irradiation of the same planning target volume. EGRT has the potential to enable true biologically guided and biologically adaptive treatment.

3.1.6 Patient Model Study: 4D XCAT Phantom

Six simulation studies have been conducted to validate the feasibility of EGRT for two clinical cases. Two typical disease sites are studied: a lung tumor scenario and a prostate tumor scenario.

3.1.6.1 Simulations Details

- Lung tumor scenario

  The lung tumor simulation includes both respiratory motion and heart motion, with periods of 4.2 s and 1 s, respectively, sampled in 12 phases. The GTV is modeled using an ellipsoid with a set of semi-axis lengths of 1.5, 1, 1.5 cm and

placed in the right lung. The GTV motion path is based on an XCAT built-in 3D periodic tumor motion trajectory with typical lung motion behavior and amplitude. The trajectory of the lung tumor motion is shown in Figure 3.13. The PTV is modeled using a cylinder that contains the full range of GTV motion with a total height of 7 cm and an ellipsoidal cross section whose set of semi-axis lengths are 2 and 2.5 cm. Two cases, with and without attenuation correction, are evaluated. 100 Gy is prescribed to 95% of the GTV volume. For the case without attenuation correction, the EGRT treatment time is 300 s with a table speed of 0.023 cm/s; for the case with attenuation correction, the EGRT treatment time is 1000 s with a table speed of 0.007 cm/s. The mean of 12 phases of the XCAT attenuation phantom is used for the PTV attenuation map calculation. The tumor, lung and background activity uptake ratio is assumed to be 8:0.5:1. The phantom geometry can be seen in Figure 3.15.

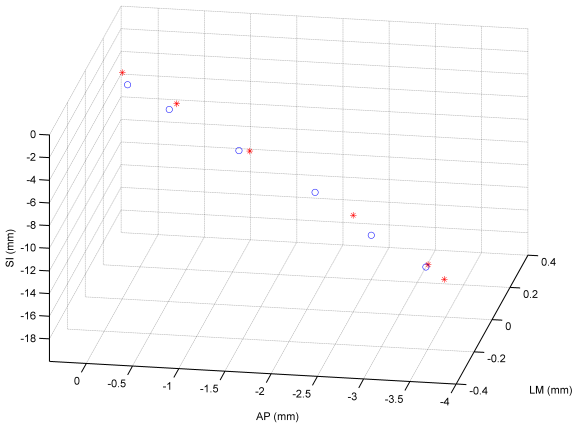

Figure 3.13: The 3D lung tumor trajectory (first phase at the origin). The red and blue markers depict each way of the tumor round trip respectively. The peak-to-peak tumor motion amplitude is 16.6 mm, 3.5 mm and 0.02 mm for superior-inferior (SI), anterior-posterior (AP), lateral-medial (LM) directions respectively.

- Prostate tumor scenario

  To evaluate the feasibility of EGRT treatment in a different disease site, more studies have been conducted for a prostate tumor case. In this work, four

prostate cases are modeled: with and without setup error and with and without an integrated boost. The GTV is modeled using the XCAT built-in prostate profile with a size of 33.27 cm^3. Since no motion is modeled in the prostate case, the PTV is constructed with a 6 mm margin around the GTV in all directions, resulting in a size of 71.73 cm^3. Due to strong inhomogeneous attenuation, all cases of prostate cancer have been simulated with the attenuation correction EGRT modulation algorithm enabled. 6 mm setup error is simulated in the lateral-medial direction. In order to make use of the same set of GATE data, the setup error is simulated by shifting the PTV in the corresponding direction. The boost region is set to be the GTV if there is no setup error and is shifted with the PTV in the presence of setup error. 78 Gy is prescribed to 95% of the GTV volume. When the integrated boost algorithm is enabled, the same amount of dose is prescribed to the boost region. The treatment time is 1000 s for all cases, with a table translation speed of 0.007 cm/s. The XCAT attenuation phantom is used for the PTV attenuation map calculation. The tumor to background activity ratio is selected to be 8.5:1. The phantom setup including the contouring of the GTV, PTV and important OARs can be found in Figures 3.16 (b) and 3.17 (b).

3.1.6.2 Results

- Lung Results

  The GATE simulation results in 39084 and 47925 beamlet responses in 300 s and 1000 s of treatment for the cases without and with attenuation correction, respectively. Figure 3.14 depicts the dose maps of all 12 simulated phases for the EGRT algorithm in both coronal and sagittal views in the absence of attenuation correction. Dose concentration in the moving target can be observed, which indicates that the EGRT method is able to track the tumor's motion.

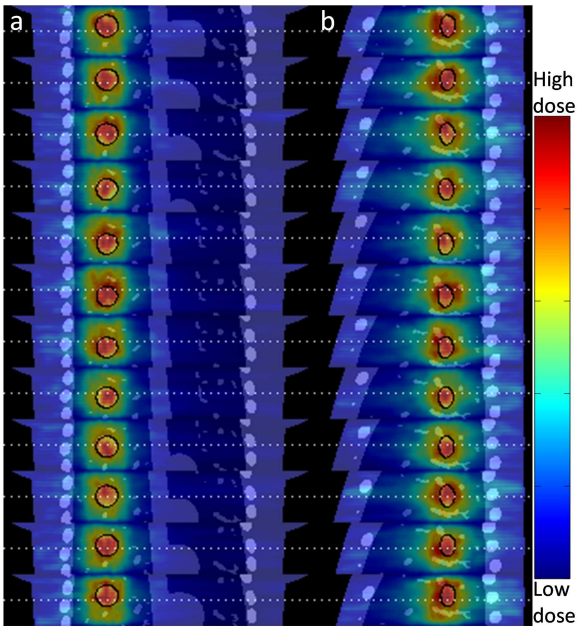

Figure 3.14: Dose maps of all 12 simulated phases in both (a) coronal and (b) sagittal views. Red means high dose and blue means low dose. Dashed lines are overlaid for positional reference. Each image is using a window of [min max] of itself.

Figure 3.15 shows the GTV point-of-view dose maps assembled from all 12 motion phases for each case, as well as the associated DVH curves comparing the conventional method with EGRT in the cases with and without attenuation correction. In both EGRT cases, there is a peaking of dose in the center of the GTV, discussed below. However, even with this inhomogeneity, there is a 31%, 41% relative increase in dose to 95% of the GTV and a 44%, 55% relative increase in dose to 50% of the GTV for the cases without and with attenuation correction, respectively, when comparing the EGRT methods with the conventional method. All dose distributions were normalized for the same integral dose to the lung.

The GTV dose relative increase is higher when attenuation correction is enabled in the EGRT method. This is due to the fact that after attenuation correction, dose is redistributed more towards the heart rather than the lung to which

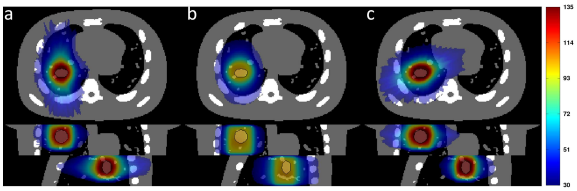

(a) Dose Distribution

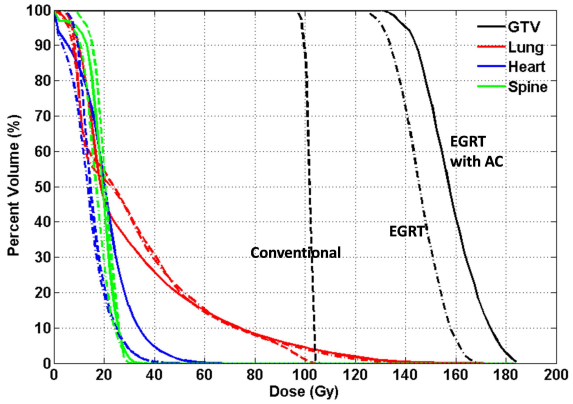

(b) Radiation Response

Figure 3.15: Point-of-view dose maps and associated DVH for the lung case with (a) EGRT, (b) conventional method and (c) EGRT with attenuation correction. The GTV is contoured using a black solid line.

the dose distribution is normalized. In other words, the GTV dose increase is achieved at the price of heart dose increase. This may be favored in the case where the heart dose increase is still within the planning limit. This study also demonstrates that EGRT modulation through customization of the response probabilities can be used to optimize the dose distribution.

- Prostate Results

  – Without Setup error

    The GATE simulation results in 22231 and 19128 beamlet responses in 1000 s of treatment for the cases without and with the integrated boost, respectively. The number of beamlet responses is reduced for the boost case due to the probability scheme in EGRT modulation. Figure 3.16 depicts the DVH and the dose distributions for all four scenarios comparing the

original EGRT case, the boosted EGRT case, the conventional case and the boosted conventional case in the absence of a setup error.

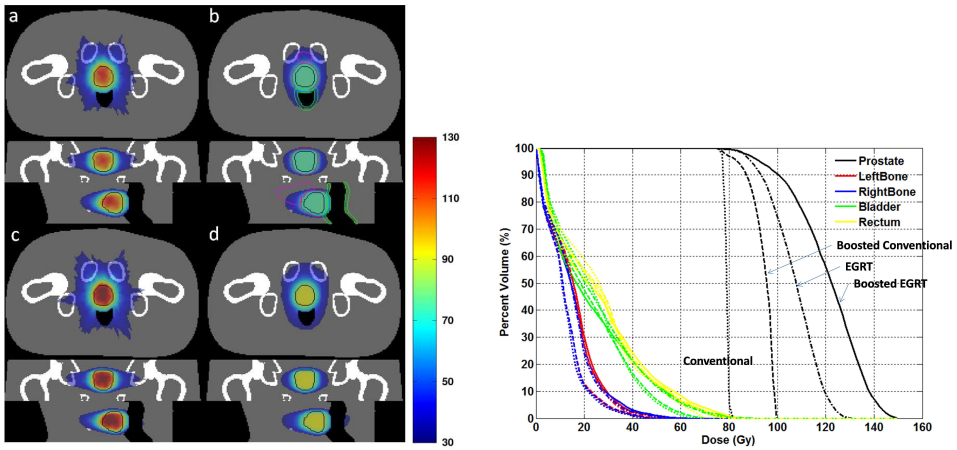

(a) Dose Distribution (b) Radiation Response

Figure 3.16: The dose distributions for (a) original EGRT, (b) conventional method, (c) boosted EGRT and (d) boosted conventional method with the associated DVH. The GTV is contoured with a black solid line in all scenarios. Contoured PTV (red), bladder (magenta), and rectum (green) are shown only in (b) for simplicity. The boost region is equivalent to the GTV in this case (without setup error).

Using the conventional method without boost as a basis for comparison, the boosted conventional method resulted in a 8% and 20% relative dose increase to 95% and 50% of the GTV, respectively. The EGRT method yielded a 14% and 36% increase, while the boosted EGRT method resulted in a 19% and 55% relative dose increase to 95% and 50% of the GTV, respectively. All methods were normalized for the same integral dose to the rectum.

– With Setup error

When setup error is simulated by shifting the PTV, the GATE simulation results in 22172 and 18929 beamlet responses in 1000 s of treatment time for the cases without and with integrated boost, respectively. Figure 3.17 depicts the DVH and the dose distributions for all four scenarios comparing the EGRT case, the boosted EGRT case, the conventional case and the

boosted conventional case in the presence of setup error.

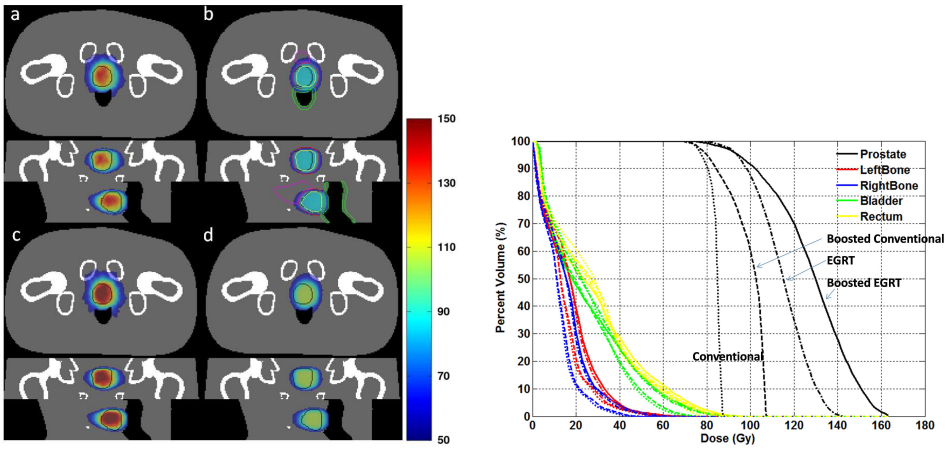

(a) Dose Distribution (b) Radiation Response

Figure 3.17: The dose distribution for (a) original EGRT, (b) conventional method, (c) boosted EGRT and (d) boosted conventional method with the associated DVH in the presence of simulated setup error. The GTV is contoured with a black solid line in all scenarios. Contoured PTV (red), bladder (magenta), rectum (green) and boost region (yellow) are shown only in (b) for simplicity.

Compared with the conventional method, the boosted conventional method results in a dose increase of 2% and 21% to 95% and 50% of the GTV, respectively. The EGRT method yields a 19% and 35% and the boosted EGRT yields a 21% and 52% relative dose increase to 95% and 50% of the GTV, respectively. All methods are normalized for the same integral dose to the rectum.

3.1.7 Patient Model Study: Discussion

In this work, we integrate positron emission into the process of radiation therapy dose delivery for treatment guidance by directing radiation beamlets along detected LOR paths in near real-time. Since PET imaging serves as the gold standard for non-invasive cancer detection and staging [32], and is increasingly being used for treatment planning [95, 21], this proposed biological targeting method may provide a way to close the loop between detection and radiation treatment.

In the current implementation of EGRT, a few items require further consideration. First, we want to discuss several issues on the EGRT results. It should be noted that the EGRT dose increase in the prostate case is smaller than that observed in the lung case, which could be explained by the PTV-ITV ratio used. As EGRT is able to concentrate the dose to the PET-avid region while the conventional method irradiates the whole PTV, the larger the PTV-ITV ratio used, the larger the anticipated advantage. The advantage of EGRT still exists when the boost scheme is implemented, which indicates that the dose increase in EGRT is due to the inherent tumor targeting.

Also, as indicated by the results, both the positron range uncertainty and angle divergence in PET do not compromise the accuracy of emission guidance. There are two possible reasons for this. One is that the uncertainty due to the positron range and angle divergence is small compared to the treatment beam resolution. The other is that the uncertainty has a zero-mean stochastic nature and while it may add a small blurring component, there should be no bias in the tumor tracking accuracy.

Besides, the results take into account the decay of PET signals during treatment. Given current simulation settings, treatment time can be generally controlled to be less than 20 minutes. Most clinical PET tracers are ^{18}F based, which has an approximate half life of 110 min. Therefore, at the end of a 20 min treatment, the activity remains 88% of the maximum, which have casted little effect on the treatment delivery efficiency.

Furthermore, unlike in the conventional method, dose peaking is observed in the center of a uniformly PET-avid target. This phenomenon is due to the backprojection effect. There are more LORs that intersect the center of the GTV than the edge, as the detected LOR rate spatial profile is the projection of the target onto the PET detector array. Therefore, more beamlet responses will be directed towards the center of the target. Due to the dose peaking effect, the results are presented in the form of

dose escalation. Note that the EGRT dose benefits due to inherent tumor tracking are generic and thus will not vanish if assessment criteria are changed. For example, if the results are normalized to the target (GTV) dose, the benefit may be in the form of reduced dose to critical structures. However, given the current EGRT algorithm design, the benefits may not be in the form of some particular criteria such as target dose uniformity without modification of the current algorithm.

Secondly, special care is needed in the practical implementation of EGRT for cancer treatment. For example, EGRT performance is dependent on the target-to-background activity uptake ratio. In the extreme case where there is no significant difference between target and background activity, there would be no advantage of EGRT over other methods. Also, although the attenuation correction EGRT modulation algorithm can help to reduce the attenuation effect, a negative consequence is an increase in treatment time if approximately the same number of beamlet responses is to be maintained since many beamlet responses are suppressed. In addition, patient and therapist are expected to receive similar levels of dose as in a standard clinical PET exam. Studies have shown that a conventional whole-body ^{18}F-FDG PET/CT examination gives an average effective patient dose equivalent to 2.5 cGy [12]. This dose should be taken into account when evaluating patient or therapist dose. It is also worth noting that the selection of radioactive tracers for different tumor sites is possible in EGRT. EGRT can benefit from new radiotracers that are developed to target various aspects of cancer biology and function. ^{18}F-Fluorodeoxyglucose (FDG), which measures the metabolic activity of glucose, is currently the gold standard in noninvasive cancer detection, with higher sensitivity and specificity than CT or MRI across a broad range of cancers. FDG is effective for many lung tumors. However, for prostate cancer, ^{18}F-Fluorocholine (FCH) and ^{18}F-fluorocyclobutane-1-carboxylic acid (FACBC) may be more effective [82, 84].

Finally, EGRT performance could be further improved by better engineering and

algorithm designs in several aspects. For example, no attempt has been made to compensate for both the scattered and random events from the raw PET coincidence dataset. Although the PTV intersection requirement reduces the error that these false events introduce, correction for scatter and random events should be implemented to further improve EGRT performance. Moreover, simulation settings are not optimized. Each beamlet response is assumed to have the same beam intensity and duration. The patient couch also has a constant translation speed. To achieve more degrees of freedom for a more optimized delivery or shorter treatment time, it is viable to modulate the intensity or duration of each beamlet, or apply a variable couch speed to allocate more treatment time for desired regions. Most of all, current EGRT algorithm design does not incorporate a conventional treatment planning component. The EGRT modulation simulations have demonstrated the feasibility of dose modulation by making use of leaf opening probabilities. The overall leaf opening probability distribution resembles the beamlet weighting distribution in conventional inverse planning. In the future development of EGRT treatment planning where a detailed plan is specified, the conventional weighting distribution may first be calculated using inverse optimization and then converted into a corresponding leaf opening probability distribution. This future work will enable a fair comparison of planned EGRT with current state-of-the-art conventional external beam therapy.

3.1.8 Patient Model Study: Conclusion

In the patient model study, we introduce EGRT as a new radiation therapy technique to improve treatment performance. The feasibility of EGRT has been demonstrated using the XCAT digital phantom as well as Monte Carlo simulations of PET acquisition and radiation delivery. An EGRT treatment scheme with attenuation correction and boost algorithms are proposed as an implementation of the EGRT concept in two clinical scenarios. The treatment scheme and associated algorithms are designed

based on realistic hardware and software technology. Compared with a conventional method, dose concentration is observed for both moving and static targets. EGRT has the potential to enable true biological targeting and guidance in radiation delivery.

3.2 Simultaneous Tracking of Multiple Targets

3.2.1 Motivation

It is known that cancer cells tend to migrate from one organ or part to another non-adjacent organ or part (called metastasis). This brings additional difficulty for cancer treatments, which is usually much more than that of treating one single localized tumor. Hence, besides tumor tracking, another major challenge in current RT is how to efficiently and effectively treat multiple targets or metastases in a single patient. When combined with the tumor tracking issue, i.e. in the situation where one or all of these targets have significant intrafractional motion, treating multiple targets can be even more challenging.

The need of an approach that can efficiently and simultaneously track multiple targets has therefore become increasingly important. This is true especially under the background that the death rates have been significantly reduced for patients with single primary tumors (thanks to the development of advanced RT techniques such as IMRT and IGRT), while they are still much higher for patients with metastatic disease. For example, it is reported that brain metastases can develop in up to half of all patients with cancer and therefore have become a serious health problem [74]. In addition, more than 100,000 patients are diagnosed to have solitary brain tumors in the United States each year and even more patients have multiple metastases [52]. Such brain tumors are usually not amenable to surgical resection and it is concluded that whole brain radiation therapy does not actually provide lasting and effective care for most patients [52].

Being able to treat multiple targets in a single patient with ease is a great benefit

of EGRT. This is because EGRT algorithms need no major modifications at all for this type of treatment while conventional methods typically have to treat the targets sequentially with multiple isocenters and plans, which can impact the overall time, cost, and complexity of treatment. More importantly, tumor tracking problem can potentially be inherently and simultaneously addressed for all the targets in EGRT. The resultant target dose escalation can therefore provide great tumor control. In this section, we investigate the feasibility of treating multiple targets using both the 4D XCAT phantom and clinical patient data.

3.2.2 Digital Patient Model

The same XCAT phantom as in previous tumor tracking section is used, except that two additional targets have been added to the left lung for a multiple-target simulation. Please refer to Figure 3.19 for an illustration of the phantom setup of all three simulated targets. The identification number of each target (i.e. GTV1, GTV2, and GTV3) is also labeled in this figure. Major motion directions for each target are marked on the coronal view (the simulation is designed such that the major motion of all targets can be observed in the same coronal image). The two added targets are of similar size as the original GTV (specific sizes are not listed here for simplicity, please refer to Table 3.1). Each PTV is made from the corresponding ITV with the same amount of margin as in the original simulation. Note that due to the fact that the two extra targets are close to each other, their PTVs are merged.

The same major EGRT and GATE simulation parameters are used. GATE simulations are conducted for the three targets with the same activity level. EGRT simulation time is reduced to 15 min. Attenuation correction algorithm is applied to correct for the corresponding effect. Exactly the same EGRT algorithms are implemented except that the PTV intersection criterion has been extended due to the increased number of PTVs: as long as the LOR intersects at least one of the PTVs,

it is eligible for response. The same conventional algorithm as in the previous tumor tracking section has been used for dose performance comparison.

Figure 3.18 shows the DVH comparison.

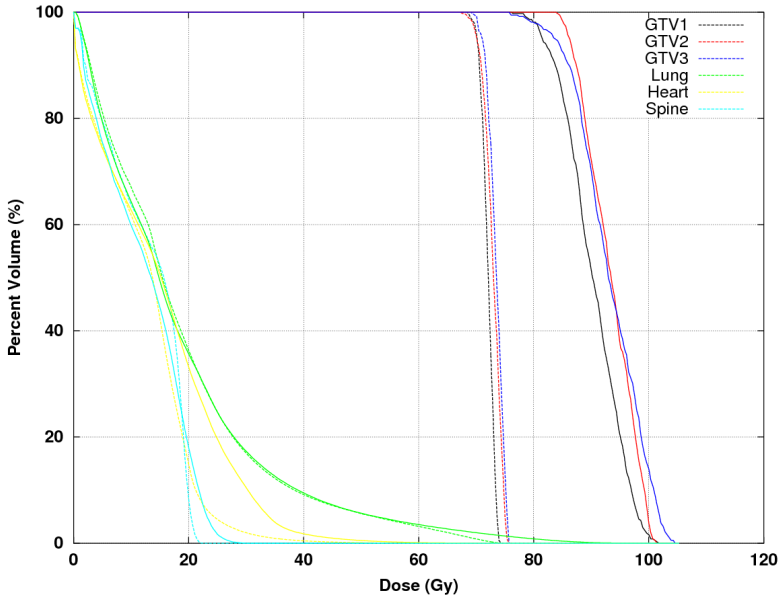

Figure 3.18: DVH comparison of EGRT and conventional treatments in the multiple-target simulation.

Note that all dose distributions are normalized for the same mean dose to the lung. The DVH comparison shows that compared to a conventional helical treatment, for 95% of the GTV, EGRT achieves a 16%, 22%, 18% relative increase in dose while for 50% of the GTV, EGRT achieves a 25%, 28%, 26% dose increase, for targets 1, 2, and 3 respectively. Same level of dose increase is achieved for all three targets. This is likely due to the fact that all GTVs have the same simulated activity level yielding a similar number of emission counts for radiation response. This may not be true in real EGRT treatments and the activity distribution for different targets are probably different. Further algorithm work is needed to enable flexible control of the dose levels of different targets given the prior knowledge of their activity distributions.

Figure 3.19 depicts the GTV point-of-view dose distribution comparison for target 1.

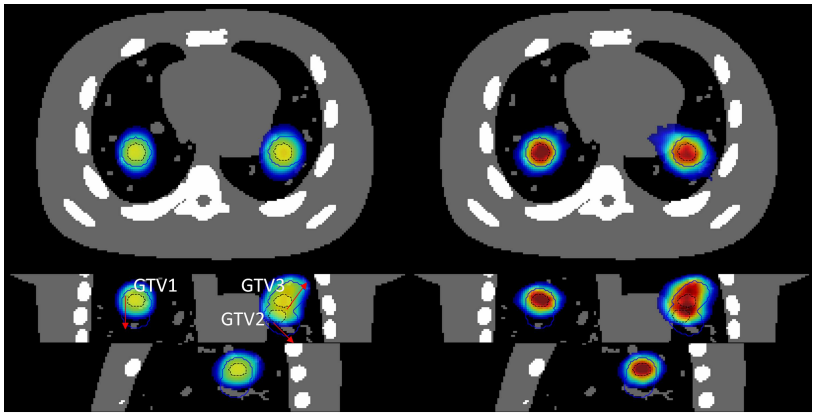

Figure 3.19: GTV point-of-view dose distribution for target 1. The red arrows on the coronal view point out the major motion direction for each of the three targets. PTV and GTV are contoured using blue solid and black dashed lines, respectively.

Similarly, Figure 3.20 and 3.21 depict the GTV point-of-view dose distribution comparison for target 2 and 3, respectively.

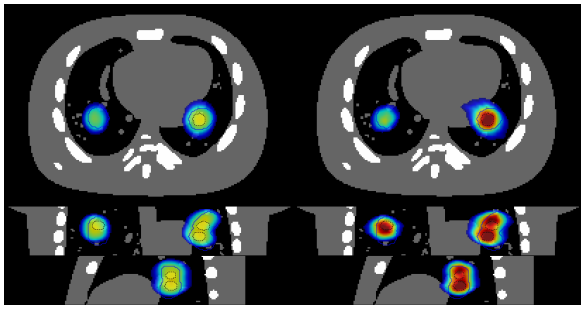

Figure 3.20: GTV point-of-view dose distribution for target 2. PTV and GTV are contoured using blue solid and black dashed lines, respectively.

Figure 3.22 shows the dose tracking of all 12 motion phases from the coronal view. It can be seen that tumor tracking is achieved simultaneously for all three targets.

3.2.3 Clinical Patient

EGRT's capability of simultaneous tracking of multiple targets is further demonstrated using clinical 4DCT and 4DPET data. Similarly like the XCAT phantom scenario, the multiple-target simulation using the clinical patient data is almost the same, in terms of major simulation parameters and processing of clinical PET and

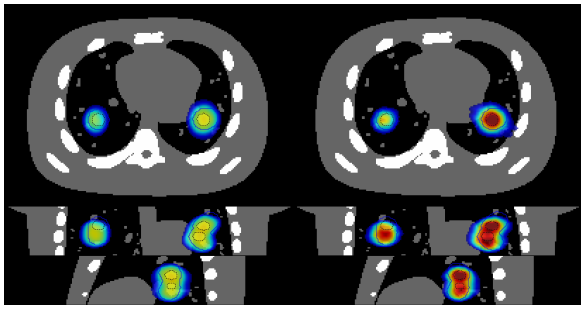

Figure 3.21: GTV point-of-view dose distribution for target 3. PTV and GTV are contoured using blue solid and black dashed lines, respectively.

CT data, as the single-target simulation. Therefore, the simulation details using the clinical patient data are not listed here for simplicity and can be found in Chapter 5.

This patient contains two moving breast cancer metastases in the lung region with a moderate motion amplitude. The identification number of each target (i.e. GTV1, GTV2) is labeled in Figure 3.24. Please refer to Figure 3.24 for an illustration of the clinically delineated GTVs and PTVs. Major motion directions for each target are marked on the coronal view of the same figure. Clinical delineated PTVs are used for the evaluation of eligible beamlet responses. The same EGRT algorithms with attenuation correction are applied. Preliminary results are presented below.

Figure 3.23 illustrates the DVH comparison of EGRT and conventional treatments.

Note that all dose distributions are normalized for the same dose to the lung. The DVH comparison shows that compared to a conventional helical treatment, for 95% of the GTV, EGRT achieves a 6%, 17% relative increase in dose and for 50% of the GTV, EGRT achieves a 15%, 29% dose increase, for targets 1 and 2, respectively. Different levels of dose increase are observed for the two targets. This is likely due to the fact that the two GTVs have different actual activity levels. Another major reason may be that one of the motion phases of target 2 is not fully tracked (to be discussed below).

Figure 3.24 depicts the GTV point-of-view dose distribution comparison for target 1 of the clinical patient case.

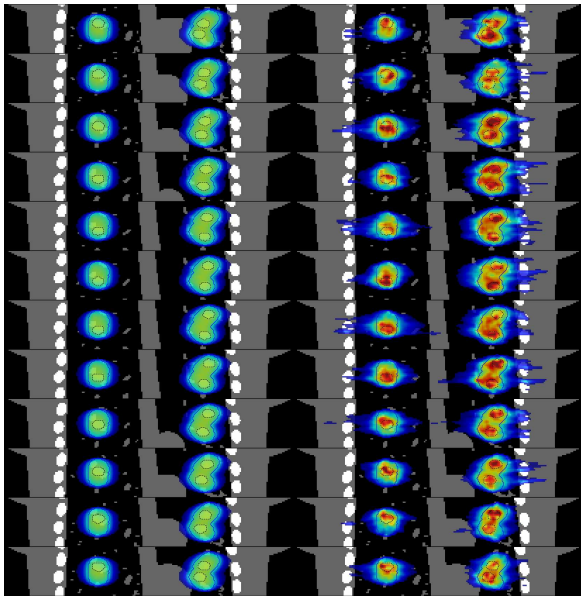

Figure 3.22: Dose maps of all 12 simulated phases in coronal view for both conventional and EGRT treatments. Red means high dose and blue means low dose. PTV and GTV are contoured using blue solid and black dashed lines respectively for positional reference. The dose maps are displayed with the same window [0.2 0.8] relative to the maximum GTV dose across all phases.

Similarly, Figure 3.25 depicts the GTV point-of-view dose distribution comparison for target 2.

Figures 3.26 and 3.27 show the dose tracking of all 6 motion phases from the coronal view for targets 1 and 2, respectively. Note that unlike the XCAT phantom case where the tumor motion of all three targets is on the same coronal plane due to the intentional simulation design, the central coronal views of the two targets in patient case are not on the same plane and thus two motion tracking figures are shown.

The tracking map shows that the last of the six motion phases of target 2 is not tracked. Despite this fact, a dose increase is still achieved for target 2 although in a smaller amount as compared to target 1. This is very likely due to the fact that these two tumors were not imaged in the same PET scan bed position and the last motion phase of target 2 happens to be located at the edge of two PET scan bed positions.

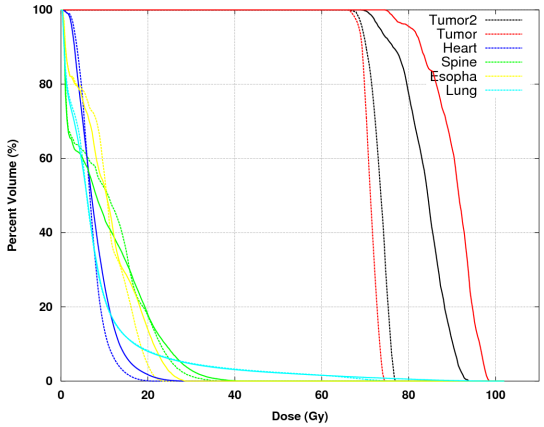

Figure 3.23: DVH comparison of EGRT and conventional treatments in the multiple-target simulation.

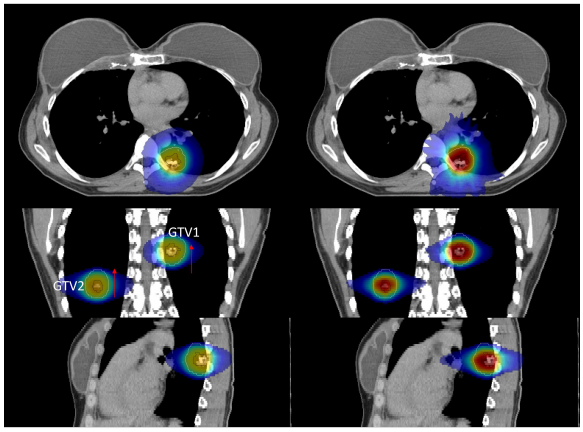

Figure 3.24: GTV point-of-view dose distribution for target 1. The red arrows on the coronal view point out the major motion directions for both targets. PTV and GTV are contoured using white and black dashed lines, respectively.

Hence, the emissions from this last phase have very low chance for detection due to the limited field of view. This is a limitation of the sequential bed position acquisition protocol for PET imaging, which would not be an issue for an EGRT system due to the helical nature of PET emission data collection.

3.3 Treatment of a Non-PET-avid Target

One problem that interests the radiation oncologist is: can EGRT treat tumor areas which do not have specific radiotracer uptake? This is of high interest clinically since

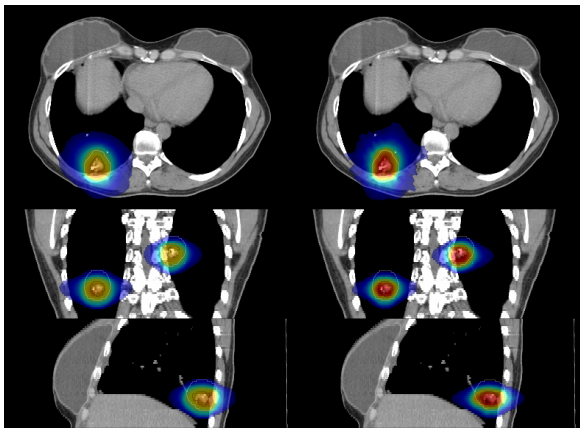

Figure 3.25: GTV point-of-view dose distribution for target 2. PTV and GTV are contoured using white and black dashed lines, respectively.

it is shown by many studies that microscopic disease can extend beyond the region of FDG uptake that is easily visualized in PET. Therefore, it is crucial for EGRT to be capable of delivering radiation to the GTV parts which have little to no avidity in the PET scan. However so far, the proposed EGRT approach is only shown to be able to treat PET-avid regions preferentially.

To address this issue, three methods are proposed, demonstrated, and presented in this section, which are referred to as *margin extension* algorithms. The essential principle of margin extension algorithms is to properly manipulate the LOR response behavior or create/transform LORs such that the GTV parts which are not PET-avid can be treated similarly as PET-avid parts. To explain these methods, please see Figure 3.28. We assume a case where the distribution of the non-PET-avid volume (referred to as *margin* in the following explanation) and GTV is shown as in the following figure. We further assume that the margin motion is very similar to the GTV motion.

Correspondingly, the three methods are named and listed below:

1. **Copy**: The first method is to *copy* the dose from the original GTV to the margin part. This can be achieved by shifting all the LORs toward the margin extension direction in an amount that is appropriate for the margin size in the

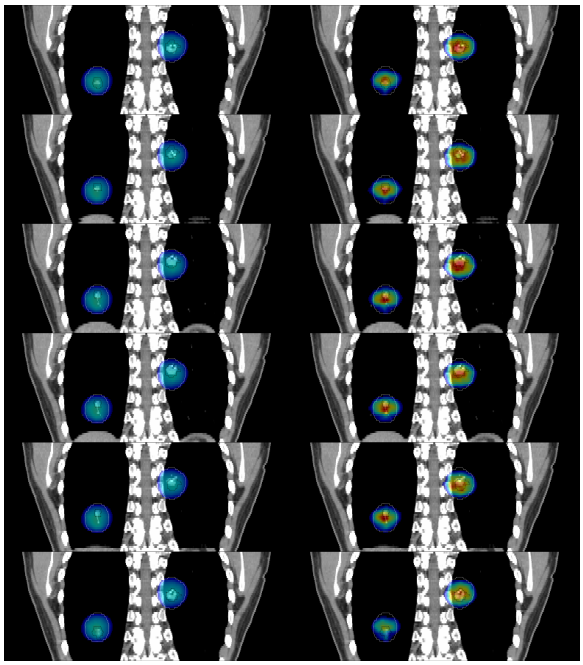

Figure 3.26: Dose maps of all 6 simulated phases in coronal view for both conventional and EGRT treatments for target 1. Red means high dose and blue means low dose. PTV and GTV are contoured using white and black dashed lines, respectively for positional reference. The dose maps are displayed with the same window [0.4 0.9] relative to the maximum GTV dose across all phases.

case of interest. Note that original LORs are still kept. In our implementation, for each LOR, we create a new LOR in addition to the original LOR as shown in Figure 3.28 (a). The spatial coordinates of all created LORs are designed such that the dose distribution deposited for the PET-avid GTV is *copied* to the location of non-PET-avid margin.

2. **Broaden**: The second method is to *broaden* the GTV dose distribution to extend it to the margin portion. This can be achieved by opening adjacent bMLC leaves toward the margin extension direction when the current beamlet-response is substantially perpendicular to the direction of desired margin extension. In our practical implementation, whenever a leaf is opened, the adjacent leaf that extends dose toward the margin direction is opened with a probability. This probability is angle dependent and it has a larger value if the original leaf is

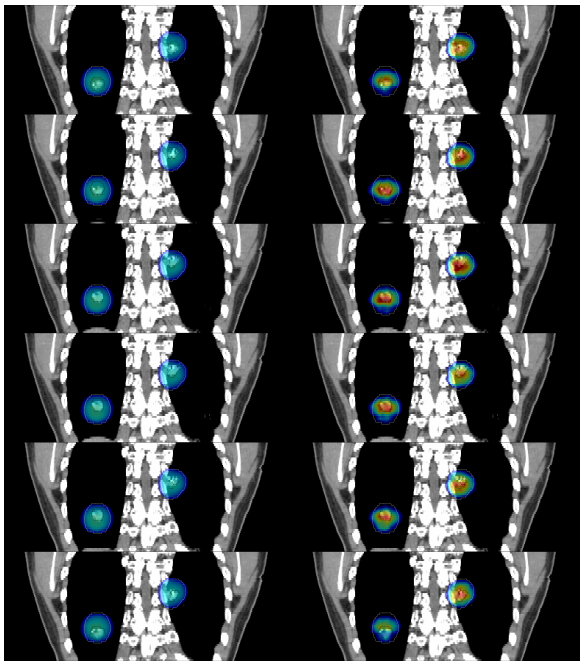

Figure 3.27: Dose maps of all 6 simulated phases in coronal views for both conventional and EGRT treatments for target 2. Red means high dose and blue means low dose. PTV and GTV are contoured using white and black dashed lines, respectively for positional reference. The dose maps are displayed with the same window [0.4 0.9] relative to the maximum GTV dose across all phases.

more perpendicular to the margin extension direction, and vice versa.

3. **Shift and broaden**: In this method, LORs are first shifted to the center of mass of the original GTV and margin combination. Then adjacent leaves are opened to broaden the original dose distribution in both directions (i.e. toward or away from margin) to accomplish the treatment goal.

All algorithms have passed the simulation tests with varying PTV sizes and setup errors in all major directions. This is to demonstrate the algorithms will work regardless of these two factors. Margin extension algorithms demonstrate that EGRT has a lot of flexibility in manipulating the LORs and the behavior of beamlet response to achieve a desired treatment or dose distribution even in the absence of specific guidance from tracer uptake. *Copy*, *broaden*, and *shift and broaden* are three methods of implementation of the margin extension concept. In all methods, prior information

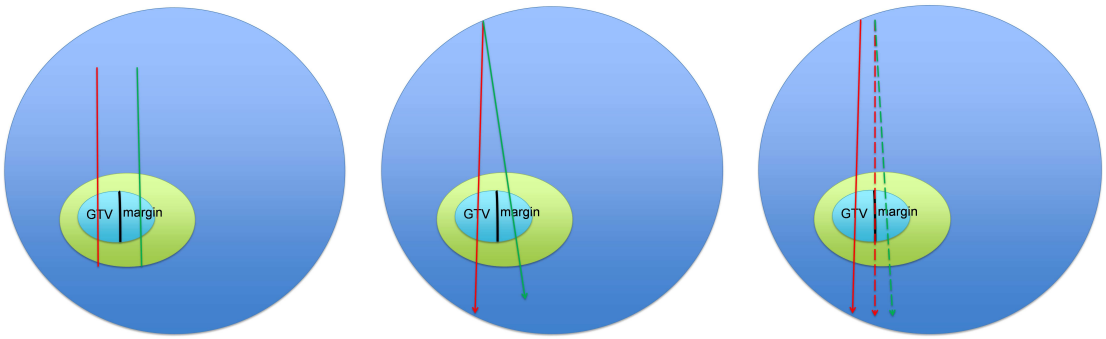

(a) Copy (b) Broaden (c) Shift and Broaden

Figure 3.28: Illustration of margin extension methods.

such as the margin extension direction and position relative to the original GTV are needed as inputs.

The above methods generate similar EGRT dose performance and hence we present the simulation setup and associated results just from the *broaden* method for simplicity, as shown in Figure 3.29. The results indicate that the center of mass of the dose distribution has been shifted toward the margin extension direction.

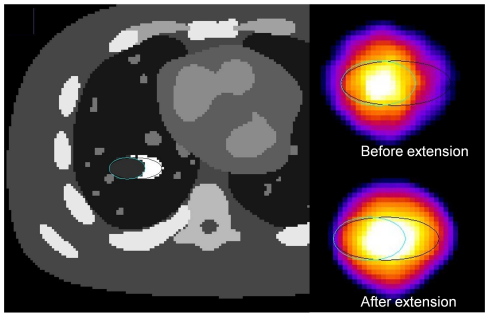

Figure 3.29: Simulation setup and GTV dose distribution for the margin extension algorithm. The GTV is in dark gray and the margin extension is in white. They are both contoured.

Figures 3.30 (a) and (b) show DVH results for EGRT simulations without and with the margin extension algorithm, respectively. In both scenarios, EGRT is compared to the same conventional helical treatment as in the previous tumor tracking section.

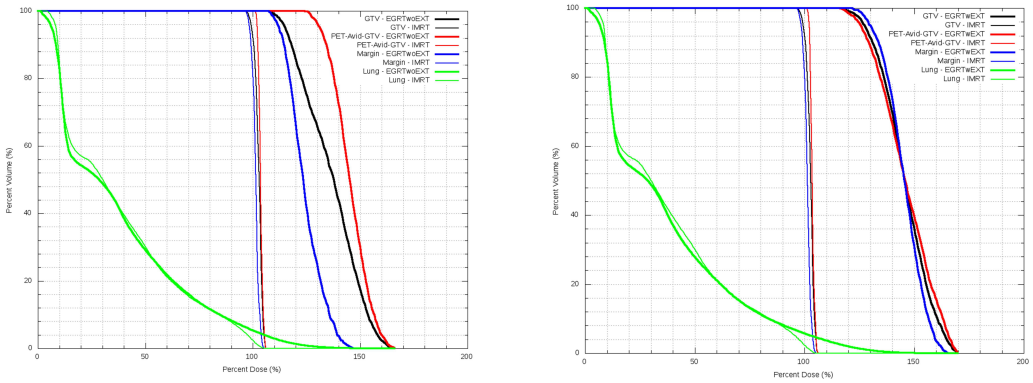

(a) Without margin extension

(b) With margin extension

Figure 3.30: DVH results for EGRT simulations without and with the margin extension algorithm.

CHAPTER IV

THE IMPACT OF MAJOR TREATMENT PARAMETERS

In our previous simulations in Chapter 3, some major simulation parameters are selected mainly based on current existing technologies. For example, part of the system design simulates the current Tomotherapy (Accuray, Sunnyvale, CA) machine such as the number of bMLC leaves, the system radius, or typical treatment time. When determining the activity level to simulate the emission process, values commonly observed in clinical PET imaging are used. For some other parameters which are more related to the EGRT concept, we choose them appropriately by balancing between the considerations of algorithm design and the constraints of hardware manufacturing. For example, ideally the rotation needs to be as fast as possible to *freeze* the tumor motion with small system latency for better tracking performance. However, the faster the rotation, the more difficult the manufacturing of the machine. Therefore, the rotation speed is chosen to be 1 second in previous simulations. Finally, for those parameters which do not have counterparts in current RT practice, we choose them based on our estimation and experience. For example, the number of firing points is chosen to be 256 since we think this would yield a satisfactory EGRT performance.

It is desirable to know how the EGRT performance is dependent on the choices of all major simulation parameters. For instance, if a rotation period of 2 s can yield similar EGRT performance as 1 s, this is very beneficial information since the burden for building the EGRT hardware can therefore be significantly reduced with slower rotation. Also, the answer to whether treatment time can be reduced without the sacrifice of treatment effectiveness is equally important.

In this chapter, we have carried out a large number of simulations to find out

the dependence of EGRT performance on the following major simulation parameters: number of firing points, PTV margin size used, treatment time, EGRT spatial window, EGRT time window, rotation speed, and a combination of rotation speed and EGRT time window. Five to seven representative values within a reasonable range have been selected and simulated for each parameter.

DVH plots, the GTV point-of-view and motion tracking dose maps, and statistics on number of beamlet responses, response time as well as phase lag have been used to analyze the performance dependence. The response time of an LOR refers to the time interval between its detection and response. The response time statistics includes the minimum (min), the mean, and the standard deviation (std) of response times for all LORs which have received radiation backprojection during treatment. In addition to statistics of response time, we have also recorded the phase lag information for each simulation. One beamlet response with phase *Lag N* means that the phase of LOR response is N phases behind its actual emission phase. In other words, *Lag 0* means that the LOR is responded in the same phase of its detection, representing accurate tumor tracking for this LOR. Due to the fact that the motion is periodic, the maximum possible phase lag is half of the total number of phases used in simulation.

For simplicity, all simulations are based on the raw EGRT algorithm. In other words, no modulation or planning algorithms have been applied. Conventional treatments are not simulated either and comparisons are done between EGRT simulations.

Last, conclusions in this chapter are drawn to be as general as possible. It is however worth emphasizing that all the conclusions are based on the XCAT simulation scenario.

4.1 Number of Firing Points

In previous standard simulations, 256 firing points have been used to densely sample the gantry circle so that EGRT could use emission guidance almost from any angle.

However, this only allows a travel time of about 4 ms between firing positions (at 1 s revolution period) and we assume the bMLC can switch to a new configuration within this travel time to prepare for dose delivery. 4 ms is a very challenging requirement for current bMLC hardware. Therefore, it would be desirable to find out whether the number of firing points can be reduced without compromising EGRT performance.

Five simulations with different numbers of firing points of 64, 96, 128, 192, and 256 have been carried out. The number of beamlet responses and associated response time statistics, as well as the statistics of phase lag are listed in Table 4.1 and 4.2.

Table 4.1: Comparison of outputs from simulations with different number of firing points

		Response time statistics		
# of firing points	# of responses	Min	Mean	Std
64	24893	0.135803	0.255117	0.062073
96	37575	0.135986	0.255146	0.061482
128	49932	0.135803	0.254677	0.061572
192	74988	0.135539	0.254593	0.06162
256	99941	0.135681	0.254745	0.061666

Table 4.2: Statistics of lag counts(in hundreds)/ratio for Table 4.1

Lag 0	Lag 1	Lag 2	Lag 3	Lag 4	Lag 5	Lag 6
67/0.27	180/0.72	0/0.00	0/0	0/0	0/0	0/0
104/0.27	270/0.72	0/0.00	0/0	0/0	0/0	0/0
139/0.28	358/0.71	0/0.00	0/0	0/0	0/0	0/0
205/0.27	543/0.72	1/0.00	0/0	0/0	0/0	0/0
275/0.27	722/0.72	1/0.00	0/0	0/0	0/0	0/0

As expected, the number of beamlet responses increases as the number of firing points increases, and with an almost linear relationship, indicated in Figure 4.1.

Response time statistics is almost the same for all simulations as shown in Table 4.1. This is as expected since the number of firing points should have no influence on the temporal aspects of the beamlet response. This is the same case for the statistics of phase lag where the ratio of each Lag N keeps almost constant although the

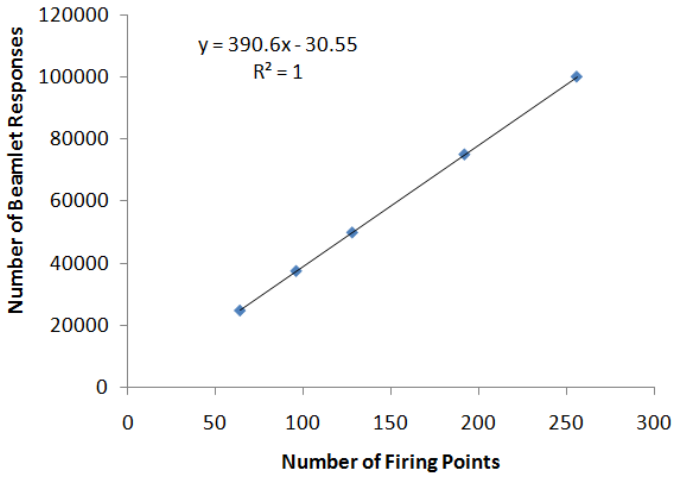

Figure 4.1: Linear relationship between number of firing points and number of beamlet responses.

sheer counts of responses keep increasing with more firing points.

It is worth mentioning that in all simulations where the EGRT time window is 0.5 s and rotation period is twice this value, the mean response time is found to be about 0.255 s, which is approximately half of the time window. This coincides with our prediction in Chapter 2. The response time minimum is about 0.13 s, which represents the minimum inherent EGRT system latency under a rotation frequency of 1 Hz. The standard deviation of 0.06 s shows that the response times of most LORs fall within a window of [0.2 0.3] s.

It is also found out that the percentage of correctly responded LORs (i.e. without phase lag) is about 27% and almost all the remaining responded LORs have a lag of just one phase. Almost none of the LORs has a lag of more than two phases. This is reasonable given that the time interval of a single phase is simulated to be 0.35 s (a motion period of 4.2 s divided into 12 phases). Therefore, it indicates that tumor tracking can be achieved (see Figure 4.3 and 4.4) with a lag of one phase as long as most LORs are responded within a delay time that is less than the time interval of a single phase.

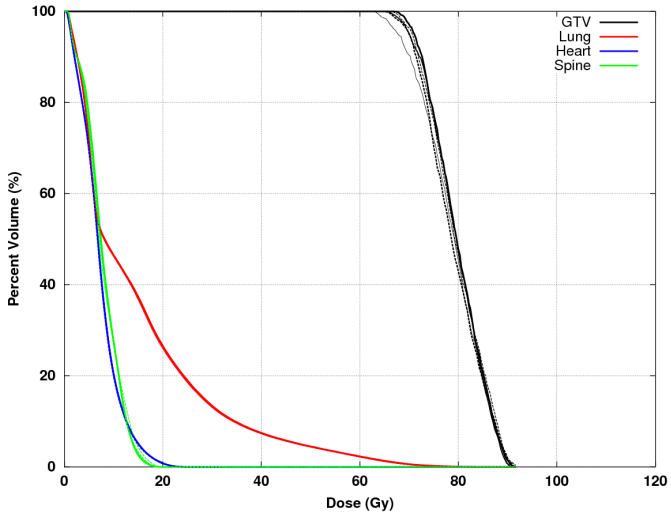

Figure 4.2: DVH comparison of EGRT treatments with different numbers of firing points. DVH curves are distinguished with increasing line width as the number of firing points increases, and with alternating styles of solid and dashed lines (starting from solid line style).

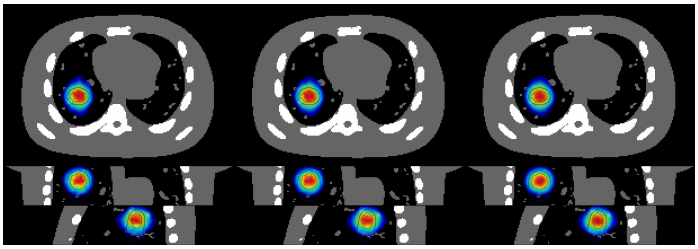

Figure 4.3: GTV point-of-view dose maps for EGRT treatments with different numbers of firing points: 64, 128, and 256 (from left to right).

Figure 4.2 illustrates the DVH comparison of five simulations which are all normalized to have the same mean lung dose. DVH results show that the number of firing points has little effect on the EGRT dose performance except that a smaller number of firing points yields a smaller GTV minimum dose. This is very beneficial for the development of the EGRT hardware since with a reduced number of firing points, the requirement of fast bMLC switching speed can be relaxed.

Figure 4.3 depicts the GTV point-of-view dose distribution comparison for different numbers of firing points: 64, 128, and 256. The GTV dose maps confirm the conclusion drawn from the DVH comparison.

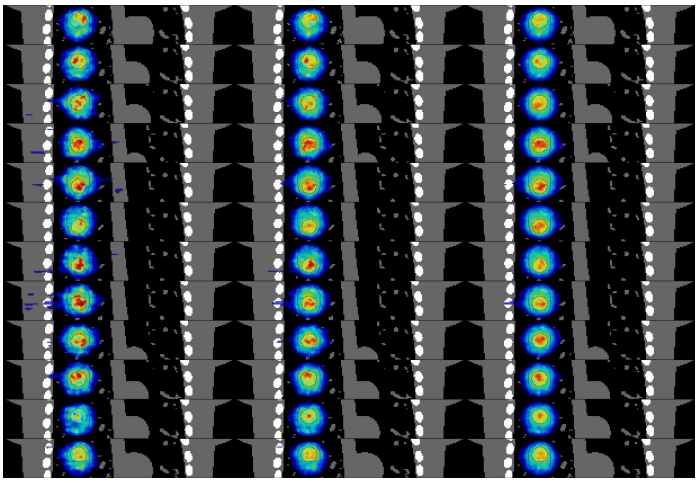

Figure 4.4: Motion tracking maps in coronal view for EGRT treatments with different numbers of firing points: 64, 128, and 256 (from left to right).

Figure 4.4 shows the dose tracking of all 12 motion phases from the coronal view. As shown in the figure, the dose map with the least number of firing points shows the most noisy tracking due to the reduced number of beamlet responses. However, accurate tumor tracking is preserved in all cases.

4.2 PTV Margin Size

The amount of margin to be used is a critical choice in RT treatments. With larger margins, the tumor will be more likely covered all the time during treatment, at the price of more irradiated healthy tissue. Therefore, it is a trade-off between the control of treatment uncertainty and dose to OARs.

Five simulations have been carried out in this section to understand how PTV margin size would affect EGRT performance. In all simulations, the PTV is defined to be the ITV plus margin. Margins of 0, 2, 4, 6, and 8 mm are used while other parameters are kept the same for all simulations.

The number of beamlet responses and associated response time statistics, as well as the statistics of phase lag are listed in Table 4.3 and 4.4. The response time statistics changes little with varying margin sizes since the temporal aspects of EGRT

treatment are not related to the margin size used. The statistics of phase lag remains similar across all simulations as shown in Table 4.12.

Table 4.3: Comparison of output from simulations with different margin sizes

		Response time statistics		
Margin size(mm)	# of responses	Min	Mean	Std
0	45079	0.135681	0.254141	0.061363
2	53483	0.135681	0.254318	0.061387
4	62669	0.135681	0.254572	0.061346
6	75194	0.135681	0.254822	0.061533
8	85580	0.135681	0.254852	0.061667

Table 4.4: Statistics of lag counts(in hundreds)/ratio for Table 4.3

Lag 0	Lag 1	Lag 2	Lag 3	Lag 4	Lag 5	Lag 6
123/0.27	326/0.72	0/0.00	0/0	0/0	0/0	0/0
146/0.27	387/0.72	0/0.00	0/0	0/0	0/0	0/0
172/0.27	453/0.72	1/0.00	0/0	0/0	0/0	0/0
206/0.27	544/0.72	1/0.00	0/0	0/0	0/0	0/0
234/0.27	620/0.72	1/0.00	0/0	0/0	0/0	0/0

As expected, the number of beamlet responses increases with the margin size (which can be easily explained using the PTV intersection criterion), and with an approximate linear relationship, indicated in Figure 4.5.

Figure 4.6 illustrates the DVH comparison of five simulations (i.e. 0, 2, 4, 6, 8 mm margin) which are all normalized to have the same mean lung dose. The DVH shows that the EGRT dose performance is very sensitive to the margin size used. It also implies that the background signal plays a significant role for giving dose to healthy tissue (since if there is no background signal, DVH curves should be very similar for all cases). Therefore, for RT treatments with large uncertainty which entails the use of a larger PTV margin, EGRT can achieve more dose benefits.

Figure 4.7 depicts the GTV point-of-view dose distribution comparing the above simulations with different PTV margin sizes (0, 4, and 8 mm), which supports the

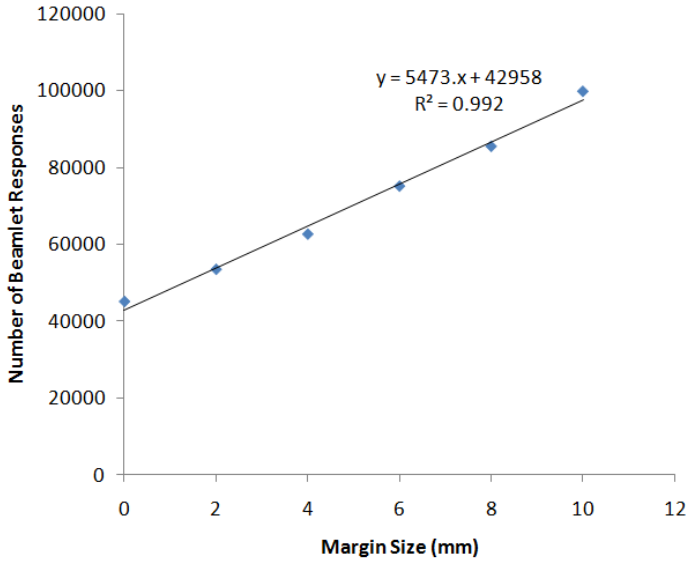

Figure 4.5: Linear relationship between margin size and number of beamlet responses.

DVH result. Note that the PTV contour is chosen from the 8 mm margin case for reference purposes in this figure and Figure 4.8.

Figure 4.8 shows correspondingly the dose tracking of all 12 motion phases from the coronal view. As shown in the figure, healthy tissue will be irradiated to the extent determined by the PTV margin size used, which therefore affects the GTV dose escalation level. However, accurate tumor tracking is preserved in all cases regardless of margin size.

4.3 Treatment Time

Treatment time is a very important consideration for any type of radiation therapy technique since it determines how many patients a hospital can treat each day. Ideally the shorter the treatment time, the more likely it will be favored by the clinical users. In our previous simulations, we simulate a treatment time of about 20 min of beam-on time. In this section, five simulations with treatment time of 400, 800, 1200, 1600, and 2000 s have been conducted to explore its influence on the EGRT treatment performance.

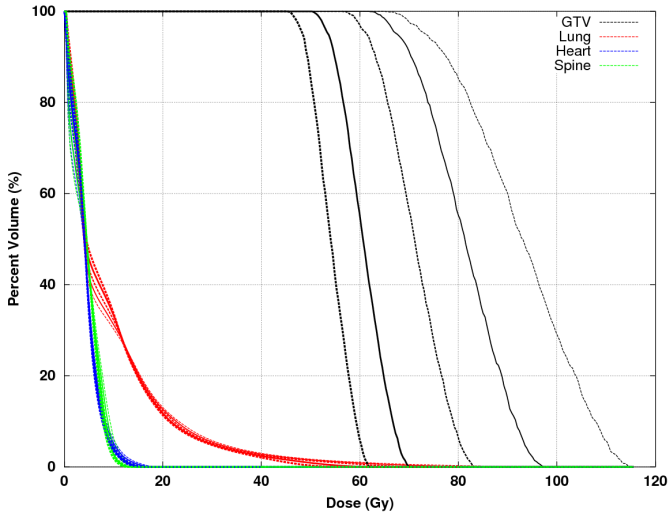

Figure 4.6: DVH comparison of EGRT treatments with different margin sizes. DVH curves are distinguished with increasing line width as the margin size decreases, and with alternating styles of solid and dashed lines (starting from dashed line style).

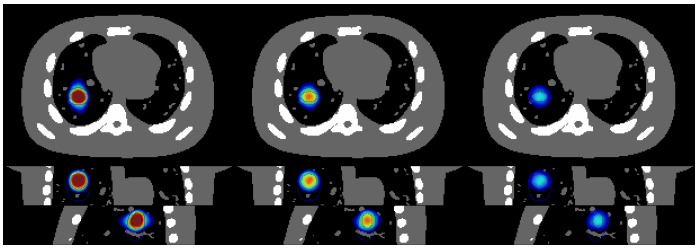

Figure 4.7: GTV point-of-view dose maps for EGRT treatments with different margin sizes: 0, 4, and 8 mm (from left to right).

The number of beamlet responses and associated response time statistics are listed in Table 4.5.

As expected, the number of beamlet responses increases with the treatment time, and with an approximate linear relationship, indicated in Figure 4.9. The response time statistics as well as statistics of phase lag changes little with varying treatment time as shown in Table 4.5 and 4.6. This is due to the fact that different treatment times result in different table speeds however the rotation speed and EGRT time window are kept constant in all cases.

Figure 4.10 illustrates the DVH comparison of five simulations (i.e. treatment time of 400, 800, 1200, 1600, and 2000 s) which are all normalized to have the same

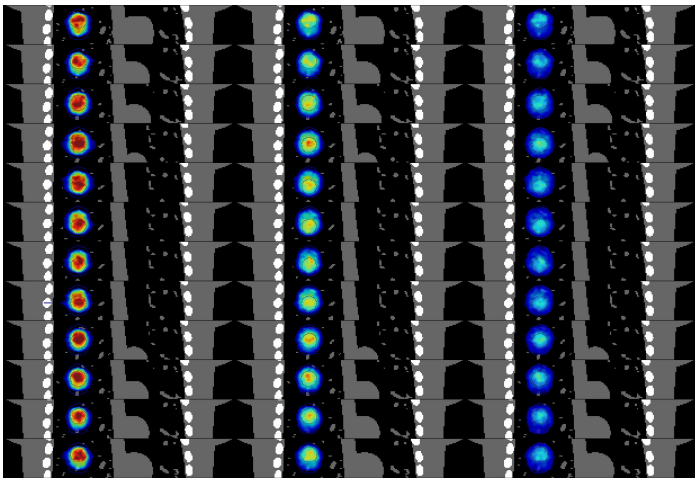

Figure 4.8: Motion tracking maps in coronal view for EGRT treatments with margin sizes: 0, 4, and 8 mm (from left to right).

Table 4.5: Comparison of output from simulations with different treatment times

Treatment time(s)	# of responses	Response time statistics		
		Min	Mean	Std
400	21414	0.136292	0.255297	0.060674
800	42686	0.135986	0.253749	0.061446
1200	63798	0.135803	0.254283	0.061126
1600	85706	0.135864	0.255083	0.061351
2000	106214	0.135864	0.255073	0.061224

mean lung dose. DVH results show that the EGRT dose performance is not sensitive to the treatment time within the range of 400 to 2000 s in this XCAT phantom case. This implies for EGRT treatment, treatment time can be reduced while maintaining dose distribution fidelity.

Figure 4.11 depicts the GTV point-of-view dose distribution comparison for the simulations with treatment times of 400, 1200, and 2000 s.

Figure 4.12 shows the dose tracking of all 12 motion phases from the coronal view correspondingly for Figure 4.11. As it is shown, an aspect of reduced treatment time is nosier dose tracking maps. However, the point-of-view map reflects the true distribution that the tumor sees and is maintained as can be seen from the DVH plots.

Table 4.6: Statistics of lag counts(in hundreds)/ratio for Table 4.5

Lag 0	Lag 1	Lag 2	Lag 3	Lag 4	Lag 5	Lag 6
59/0.27	154/0.72	0/0.00	0/0	0/0	0/0	0/0
117/0.27	308/0.72	0/0.00	0/0	0/0	0/0	0/0
175/0.27	461/0.72	1/0.00	0/0	0/0	0/0	0/0
234/0.27	620/0.72	1/0.00	0/0	0/0	0/0	0/0
291/0.27	768/0.72	2/0.00	0/0	0/0	0/0	0/0

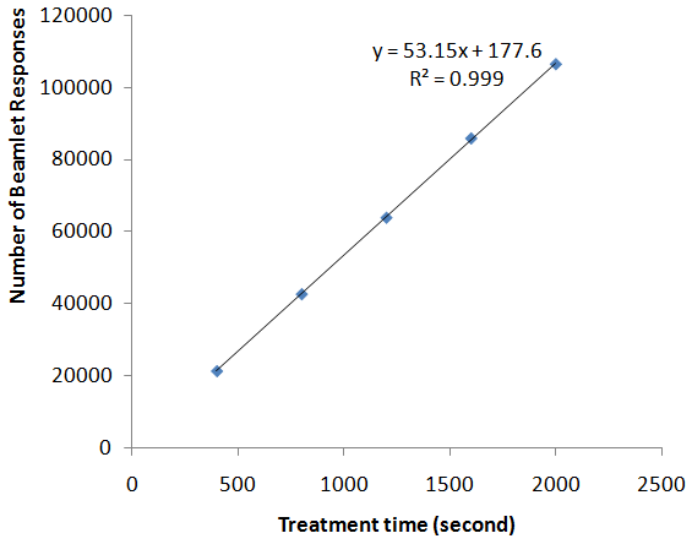

Figure 4.9: Linear relationship between treatment time and number of beamlet responses.

4.4 EGRT Spatial Window

The EGRT basic algorithm says that the LOR must intersect the Linac source within an angle tolerance on the gantry circle specified by the EGRT spatial window. The smaller the EGRT spatial window, the more accurate the beamlet response. Six simulations with different spatial windows of $\pm 0.25°$, $\pm 0.5°$, $\pm 0.75°$, $\pm 1°$, $\pm 2°$, $\pm 5°$ have been carried out to understand how the EGRT spatial window would affect EGRT performance.

The number of beamlet responses and associated response time statistics, as well as the statistics of phase lag are listed in Table 4.7 and 4.8.

As one would expect, the number of beamlet responses increases as the spatial

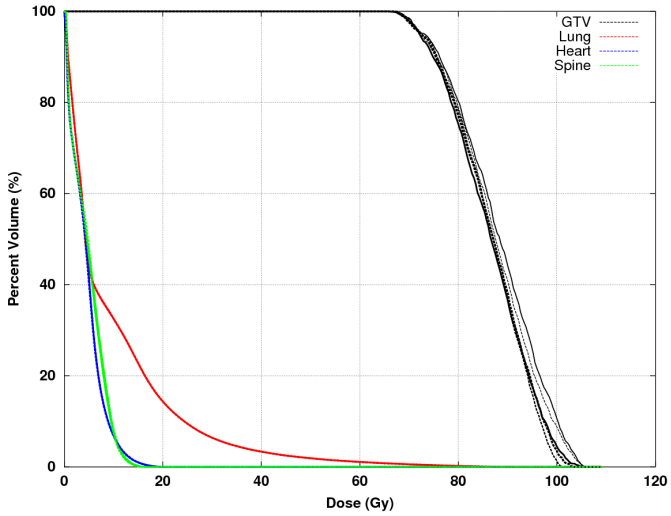

Figure 4.10: DVH comparison of EGRT treatments with different treatment times. DVH curves are distinguished with increasing line width as the treatment time increases, and with alternating styles of solid and dashed lines (starting from dashed line style).

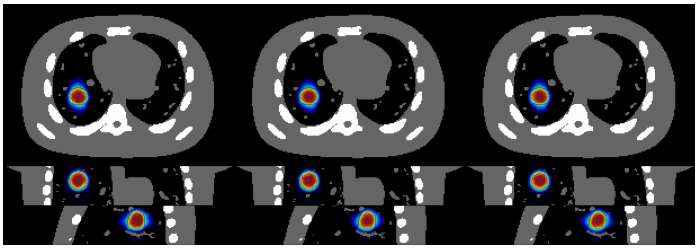

Figure 4.11: GTV point-of-view dose maps for EGRT treatments with different treatment times: 400, 1200, and 2000 s (from left to right).

window increases, and with an almost linear relationship, indicated in Figure 4.13.

Since only the EGRT spatial window has been changed and this is not related to the temporal aspects, the response time statistics is almost the same for all simulations as shown in Table 4.7. This is the same case for the statistics of phase lag where the ratio of each *Lag N* keeps almost constant although the sheer counts increase with a wider spatial window.

Figure 4.14 illustrates the DVH comparison of six simulations which are all normalized to have the same mean lung dose. The DVH shows that the larger the spatial window, the worse the dose performance. However, within the range of [$\pm 0.25^\circ$ $\pm 1^\circ$],

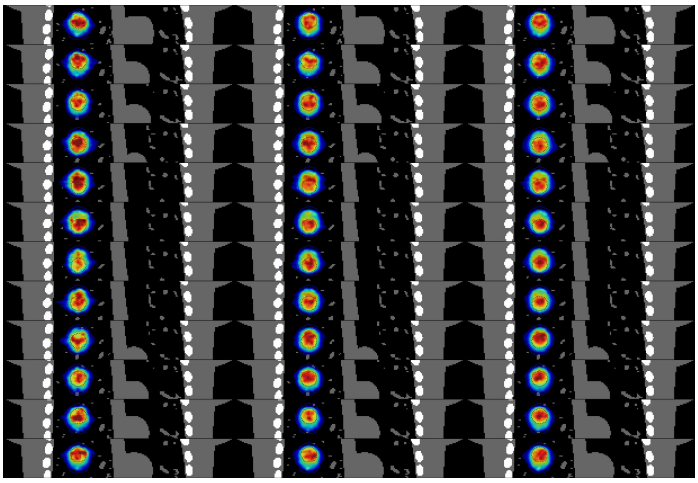

Figure 4.12: Motion tracking maps in coronal view for EGRT treatments with different treatment times: 400, 1200, and 2000 s (from left to right).

Table 4.7: Comparison of outputs from simulations with different EGRT spatial windows

		Response time statistics		
Spatial window	# of responses	Min	Mean	Std
±0.25°	67529	0.135986	0.255987	0.061526
±0.5°	133288	0.135681	0.25548	0.061614
±0.75°	196728	0.134583	0.254982	0.061511
±1°	258372	0.134583	0.254326	0.061477
±2°	487009	0.131287	0.252247	0.061529
±5°	1029183	0.122864	0.246043	0.061479

the difference in GTV dose is small.

Figure 4.15 depicts the GTV point-of-view dose distribution comparison for spatial windows of ±0.25°, ±1°, and ±5°.

Figure 4.16 shows the dose tracking of all 12 motion phases from the coronal view. As shown in the figure, the smallest spatial window shows the most accurate tumor tracking, with largest noise due to the reduced number of beamlet responses. For ±5° spatial window, no obvious lag in dose tracking is observed, although inferior dose escalation is present due to the increase of spatial error.

Table 4.8: Statistics of lag counts(in hundreds)/ratio for Table 4.7

Lag 0	Lag 1	Lag 2	Lag 3	Lag 4	Lag 5	Lag 6
183/0.27	490/0.72	1/0.00	0/0	0/0	0/0	0/0
365/0.27	965/0.72	2/0.00	0/0	0/0	0/0	0/0
538/0.27	1424/0.72	3/0.00	0/0	0/0	0/0	0/0
711/0.27	1868/0.72	4/0.00	0/0	0/0	0/0	0/0
1372/0.28	3488/0.71	8/0.00	0/0	0/0	0/0	0/0
3081/0.29	7193/0.69	16/0.00	0/0	0/0	0/0	0/0

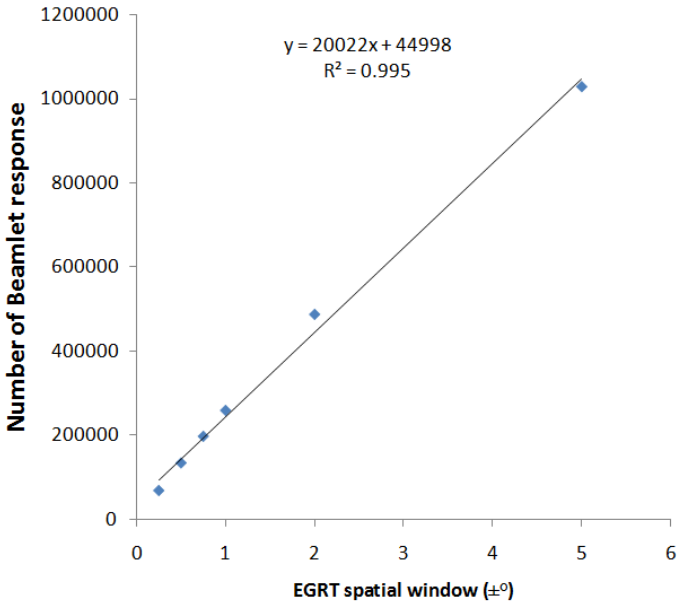

Figure 4.13: Linear relationship between EGRT spatial window and number of beamlet responses.

4.5 EGRT Time Window

The EGRT time window is the time interval in the past from which the Linac selects LORs for radiation response when arriving at each firing point. Since this is the parameter that directly relates to the temporal accuracy of tumor tracking, it needs to be properly determined. To understand how the EGRT time window (given the same rotation frequency of 1 Hz) would affect EGRT performance, the results of six simulations with different EGRT time windows are obtained for comparison. These six simulations are exactly the same except that the time windows are: 0.25, 0.5,

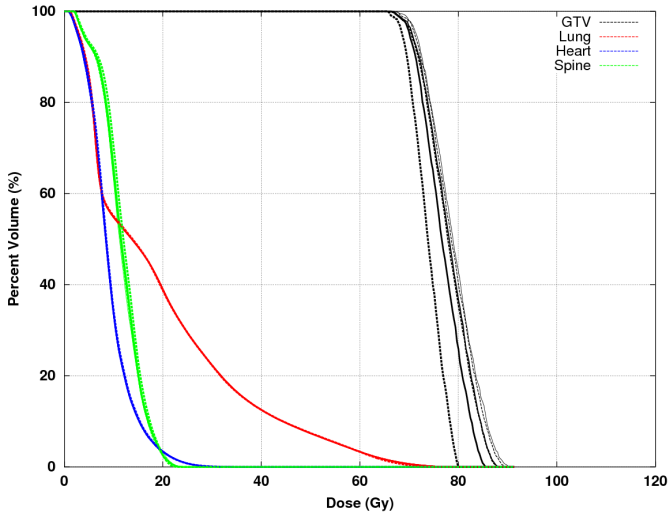

Figure 4.14: DVH comparison of EGRT treatments with different spatial windows. DVH curves are distinguished with increasing line width as the EGRT spatial window increases, and with alternating styles of solid and dashed lines (starting from solid line style).

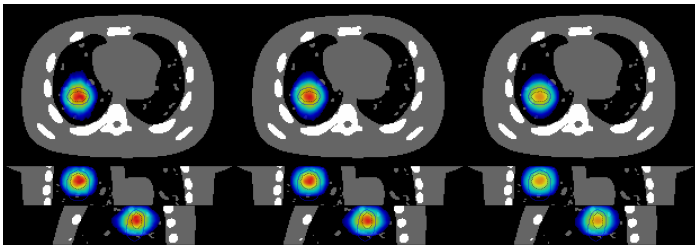

Figure 4.15: GTV point-of-view dose maps for EGRT treatments with different EGRT spatial windows: $\pm 0.25°$, $\pm 1°$, and $\pm 5°$ (from left to right).

0.75, 1, 1.25, and 5 s.

The number of beamlet responses and associated response time statistics, as well as the statistics of phase lag are listed in Table 4.9 and 4.10.

As expected, the number of beamlet responses increases as the EGRT time window increases, and with an almost linear relationship, indicated in Figure 4.17.

The response time statistics in Table 4.9 shows that the fastest response to an LOR is about 0.13 s after its detection, which is independent of the EGRT time window used. With more LORs included as candidates for radiation response as the time window increases, both the mean and standard deviation of response times

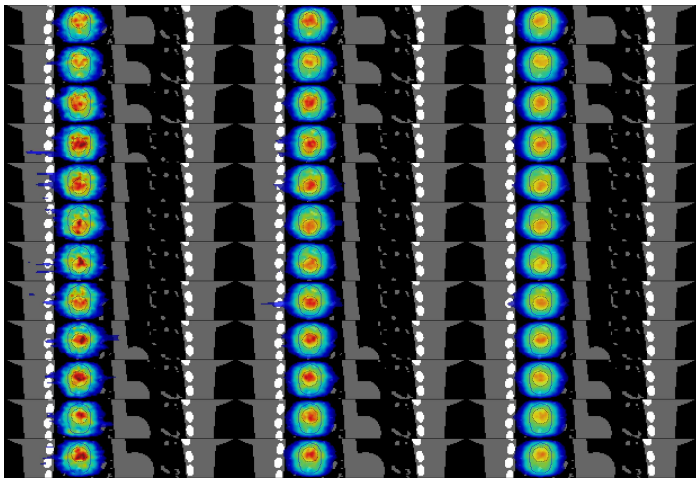

Figure 4.16: Motion tracking maps in coronal view for EGRT treatments with different spatial windows: ±0.25°, ±1°, and ±5° (from left to right).

Table 4.9: Comparison of outputs from simulations with different EGRT time windows

		Response time statistics		
Time window (s)	# of responses	Min	Mean	Std
0.25	63315	0.135681	0.200091	0.030148
0.5	133288	0.135681	0.25548	0.061614
0.75	192781	0.135681	0.39269	0.212331
1	258844	0.135681	0.497978	0.257312
1.25	314866	0.135681	0.622905	0.35595
5	1029948	0.135681	2.257822	1.425035

increase. Table 4.10 depicts the statistics of phase lag for all responded beamlets. As indicated by the results, the smaller the window, the less the phase lag and hence the better the tumor tracking. When the time window is 5 s (larger than the period 4.2 s), all possible phase lags happen. Also note that, the number of Lag 0 counts stays the same for windows of 0.5, 0.75, 1, and 1.25 s. This is because this quantity is saturated, which implies that any time window increase within this range is not useful.

Figure 4.18 illustrates the DVH comparison of six simulations which are all normalized to have the same mean lung dose. Figure 4.19 depicts the GTV point-of-view dose distribution comparison for time windows of 0.25, 1, and 5 s.

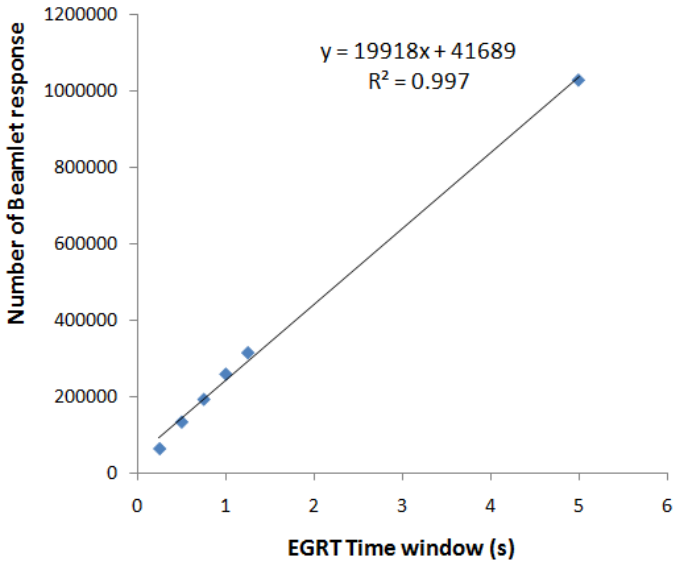

Figure 4.17: Linear relationship between EGRT time window and number of beamlet responses.

Table 4.10: Statistics of lag counts(in hundreds)/ratio for Table 4.9

Lag 0	Lag 1	Lag 2	Lag 3	Lag 4	Lag 5	Lag 6
272/0.43	360/0.56	0/0	0/0	0/0	0/0	0/0
365/0.27	965/0.72	2/0.00	0/0	0/0	0/0	0/0
365/0.18	987/0.51	553/0.28	21/0.01	0/0	0/0	0/0
365/0.14	987/0.38	1016/0.39	219/0.08	0/0	0/0	0/0
365/0.11	987/0.31	1016/0.32	539/0.17	240/0.07	0/0	0/0
1030/0.10	2099/0.20	1988/0.19	1376/0.13	1577/0.15	1555/0.15	671/0.06

Figure 4.20 shows the dose tracking of all 12 motion phases from the coronal view. As shown in the figure, the smallest time window shows the most accurate tumor tracking. For a 5 s time window, both lag in dose tracking and inferior dose escalation are observed.

4.6 Rotation Period

In our previous simulations, 1 s has been used as the rotation period. Such fast rotation imposes engineering challenges to build the EGRT system. In this section, we investigate how EGRT performance is related to the gantry rotation speed. Eight simulations of different rotation periods (i.e. 1, 1.5, 2, 2.5, 3.5, 4, 6, 8 s) have been

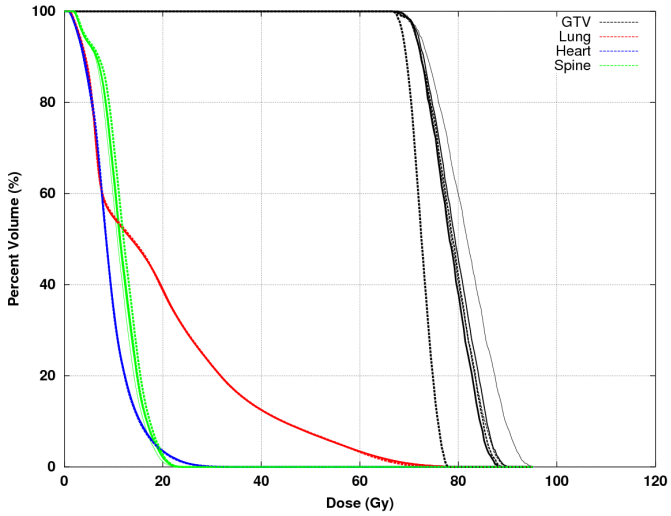

Figure 4.18: DVH comparison of EGRT treatments with different EGRT time windows. DVH curves are distinguished with increasing line width as the EGRT time window increases, and with alternating styles of solid and dashed lines (starting from solid line style).

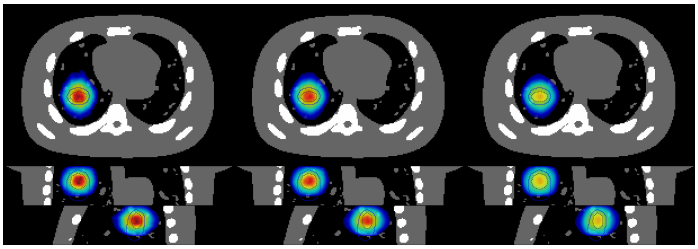

Figure 4.19: GTV point-of-view dose maps for EGRT treatments with EGRT time windows: 0.25, 1, and 5 s (from left to right).

conducted for this investigation. A 0.5 s time window has been kept constant for all eight simulations. In this case, it is expected that when the rotation period gets larger (i.e. rotation is slower), the total number of beamlet responses become smaller and eventually reduces to zero after a certain value. This can be explained using Figure 4.21.

Assume the Linac arrives at the firing position located at point G. Since in the simulation each detector arc covers 90 degrees, the detector pair will be at positions depicted by the arcs $\overset{\frown}{AB}$ and $\overset{\frown}{CD}$. To obtain a qualified LOR for response, the algorithm will check the LOR detection history within an EGRT time window of 500

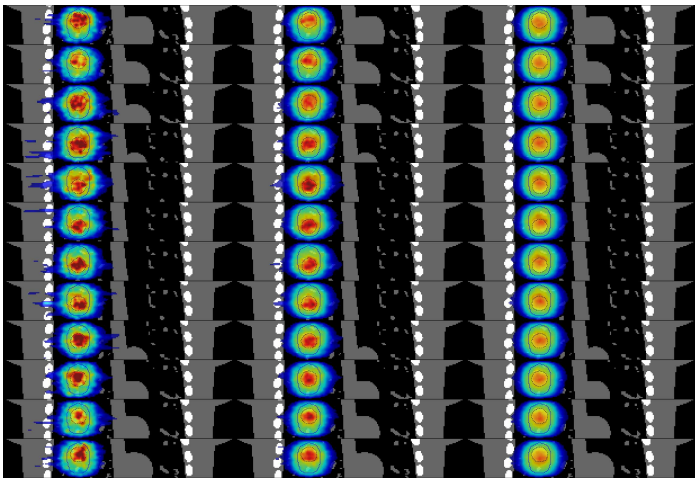

Figure 4.20: Motion tracking maps in coronal view for EGRT treatments with different EGRT time windows: 0.25, 1, and 5 s (from left to right).

ms and with a spatial window of ±0.5°. In other words, only LORs that have been detected by the detector in the previous 500 ms and at the same time have almost intersected the X-ray source will have a chance to be responded to. When the rotation period is 4 seconds, 500 ms corresponds to a travel range of 45 degrees for the Linac, i.e. Linac travels from Point H to G. Therefore, the only possible LOR that is eligible for radiation response is line EOF in such a case. When the rotation period is larger than 4 seconds, no LOR will be possibly detected and responded to at any firing point. This coincides with our simulation results where there is no beamlet response from simulations with rotation periods of 4, 6, and 8 s. Therefore, only the results from simulations with rotation periods of 1, 1.5, 2, 2.5, and 3.5 s are shown.

The number of beamlet responses and associated response time statistics, as well as the statistics of phase lag are listed in Table 4.11 and 4.12. The response time statistics are different from previous sets of simulations. The minimum and mean of response times keep increasing with slower rotation. This is because when rotation period is long, the Linac responses tend to fall behind the LOR detections. Also due to this reason, the standard deviation is decreasing under a fixed time window.

Since the EGRT time window is fixed to be 500 ms, no LOR with a lag more than

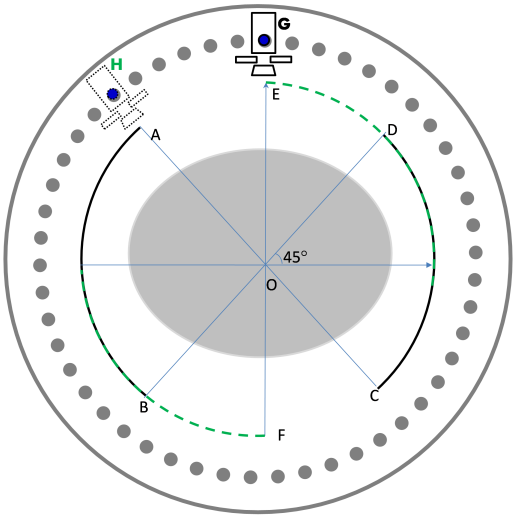

Figure 4.21: EGRT geometry for the explanation of the general relationship between number of beamlet responses and rotation speed.

Table 4.11: Comparison of output from simulations with different rotation periods

Rotation period (s)	# of responses	Response time statistics		
		Min	Mean	Std
1	133288	0.135681	0.25548	0.061614
1.5	115188	0.203888	0.36186	0.079402
2	62377	0.270874	0.399993	0.060645
2.5	29861	0.339874	0.4331	0.042979
3.5	1292	0.475403	0.49226	0.005545

500 ms will be responded to. Therefore, for all five listed simulations, the phase lag is kept within 2 phases as shown in Table 4.12. Also note that with decreasing rotation speed, the phase lag of beamlet responses tends to shift from Lag 0 to Lag 2.

As explained by Figure 4.21, the number of beamlet responses decreases as the rotation period increases, and with an approximate linear relationship, indicated in Figure 4.22

Figure 4.23 illustrates the DVH comparison of four simulations (i.e. 1, 1.5, 2, 2.5 s) which are all normalized to have the same mean lung dose. The result of 3.5 s is not listed since the slow rotation results in a non-comparable dose distribution. DVH shows that the EGRT dose performance has little to do with the rotation speed

Table 4.12: Statistics of lag counts(in hundreds)/ratio for Table 4.11

Lag 0	Lag 1	Lag 2	Lag 3	Lag 4	Lag 5	Lag 6
365/0.27	965/0.72	2/0.00.	0/0	0/0	0/0	0/0
93/0.08	926/0.80	132/0.11	0/0	0/0	0/0	0/0
14/0.02	507/0.81	101/0.16	0/0	0/0	0/0	0/0
0/0.00	227/0.76	71/0.23	0/0	0/0	0/0	0/0
0/0	7/0.58	5/0.41	0/0	0/0	0/0	0/0

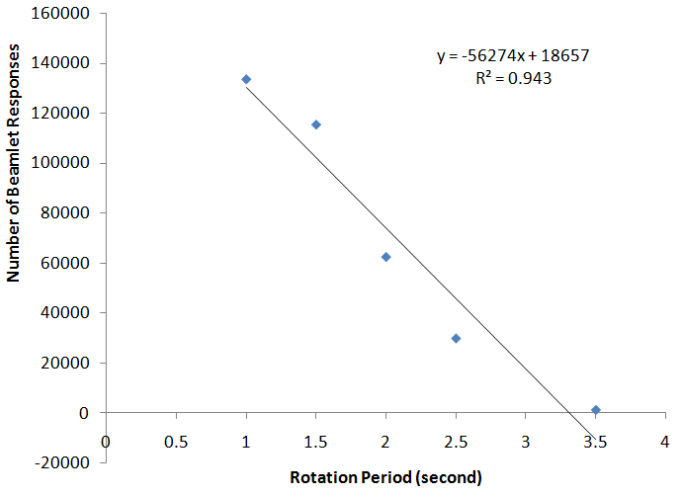

Figure 4.22: Linear relationship between rotation period and number of beamlet responses.

within a range of [1 2.5] s, as long as the EGRT time window is constant. This is beneficial for the manufacturing of the EGRT system since now the bMLC switching speed can be reduced potentially by a factor of at least 2.5 (and potentially more when combined with other parameter changes such as the reduction of firing points, see section 4.1). A compromise is that the number of beamlet responses is decreasing yielding potentially longer treatment times required to achieve a specific dose target.

Figure 4.24 depicts the GTV point-of-view dose distribution comparison for the above three simulations with rotation periods of 1, 2, and 2.5 s.

Figure 4.25 shows the dose tracking of all 12 motion phases from the coronal view. As shown in the figure, the dose map with largest rotation period shows the most noisy tracking due to the reduced number of beamlet responses. However, accurate

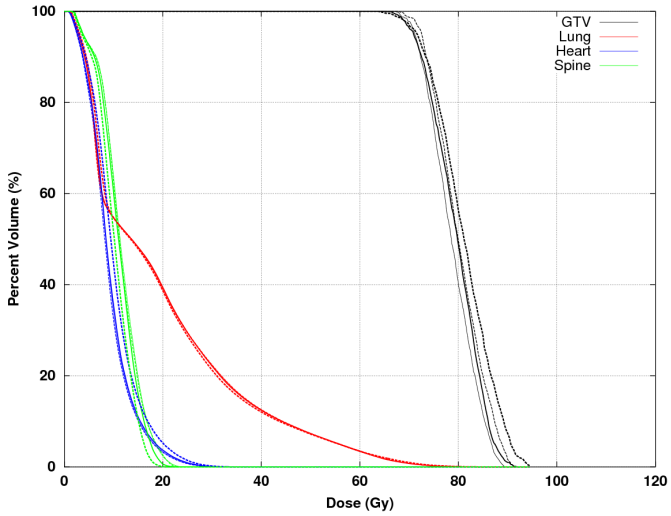

Figure 4.23: DVH comparison of EGRT treatments with different rotation periods. DVH curves are distinguished with increasing line width as the rotation period increases, and with alternating styles of solid and dashed lines (starting from solid line style).

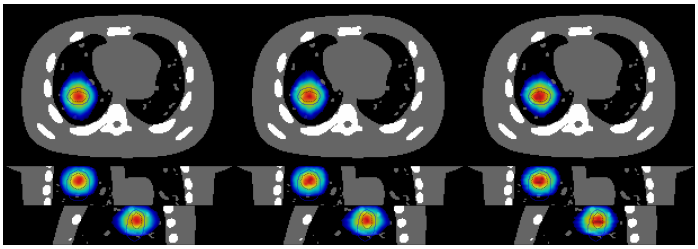

Figure 4.24: GTV point-of-view dose maps for EGRT treatments with rotation periods: 1, 2, and 2.5 s (from left to right).

tumor tracking is preserved in all cases.

4.7 Combination of Rotation Period and Time Window

Due to the special detector placement in EGRT (one pair of symmetrically opposed 90° arcs), it is preferred that the EGRT time window is half of the rotation period. This can be explained again using Figure 4.21. In this case, when the Linac arrives at each firing point, it evaluates the LORs that have been detected within a time window that is half of the rotation period for beamlet responses. Within this window, the Linac always finishes traveling a 180° arc and the detector pair has a full coverage of

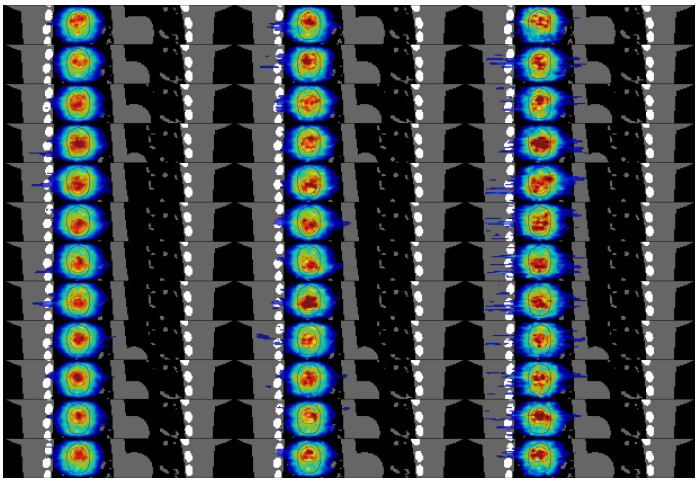

Figure 4.25: Motion tracking maps in coronal view for EGRT treatments with different rotation periods: 1, 2, and 2.5 s (from left to right).

the gantry circle due to its paired structure. Therefore, this combination of rotation period and time window ensures that the emission guidance will be fully utilized for any firing point.

Five simulations with a rotation period/time window combination of 1/0.5, 2/1, 4/2, 6/3, and 8/4 s/s have been carried out to explore its influence on EGRT performance. The number of beamlet responses and associated response time statistics are listed in Table 4.13. The response time statistics change significantly with varying rotation periods. The same conclusion holds true that the mean of response times is approximately half of the EGRT time window for all simulations. The number of beamlet responses slightly decreases with the reduced rotation speed.

Table 4.13: Comparison of output from simulations with different combinations of rotation period and time window

		Response time statistics		
Combination (s/s)	# of responses	Min	Mean	Std
1/0.5	133288	0.135681	0.25548	0.061614
2/1	128542	0.270874	0.508004	0.122845
4/2	121251	0.541046	1.008661	0.245819
6/3	114433	0.812988	1.501988	0.367014
8/4	108229	1.08374	1.990673	0.489642

The statistics of phase lag are listed in Table 4.14. It indicates that the phase lag tends to shift from Lag 0 to Lag 6 (the maximum possible phase lag) as the rotation period increases.

Table 4.14: Statistics of lag counts(in hundreds)/ratio for Table 4.13

Lag 0	Lag 1	Lag 2	Lag 3	Lag 4	Lag 5	Lag 6
365/0.27	965/0.72	2/0.00.	0/0	0/0	0/0	0/0
14/0.01	684/0.53	582/0.45	4/0.00	0/0	0/0	0/0
0/0	28/0.02	385/0.31	509/0.42	279/0.23	8/0.00 0/0	
0/0	0/0	40/0.0357	273/0.2390	340/0.29	314/0.27	175/0.15
0/0	0/0	0/0	68/0.06	334/0.30	448/0.41	230/0.21

Figure 4.26 illustrates the DVH comparison of five simulations (i.e. 1, 2, 4, 6, and 8 s rotation periods) which are all normalized to have the same mean lung dose. The DVH shows that the EGRT dose performance decreases with slower rotation as expected. However, the reduction of the DVH performance is not as significant as one would expect. This is likely due to the fact that although tumor tracking contains significant lag for large rotation periods (as shown in Figure 4.28), the mean GTV position is always equivalently targeted as in this special XCAT phantom case.

Figure 4.27 depicts the GTV point-of-view dose distribution comparison for the above three simulations with combinations of 1/0.5, 4/2, and 8/4 s/s.

Figure 4.28 shows the dose tracking of all 12 motion phases from the coronal view. As shown, significant tracking lag is observed for the rotation period of 8 s.

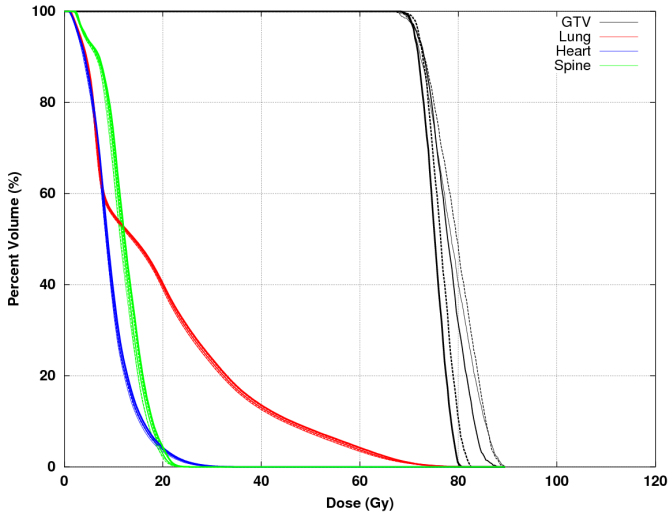

Figure 4.26: DVH comparison of EGRT treatments with different rotation periods and time windows. The DVH curves are distinguished with increasing line width as the rotation period increases, and with alternating styles of solid and dashed lines (starting from solid line style).

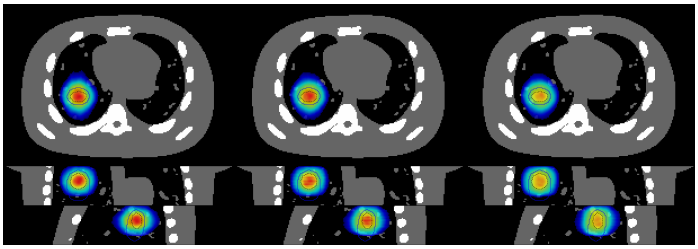

Figure 4.27: GTV point-of-view dose maps for EGRT treatments with rotation periods and time windows: 1/0.5, 4/2, and 8/4 s/s (from left to right).

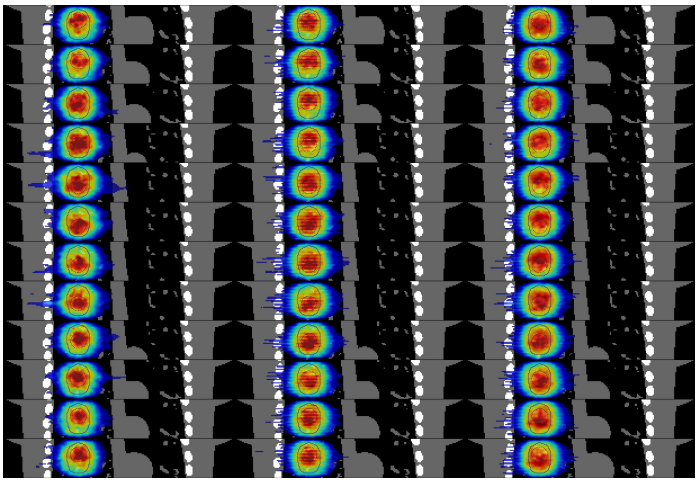

Figure 4.28: Motion tracking maps in coronal view for EGRT treatments with different rotation periods and time windows: 1/0.5, 4/2, and 8/4 s/s (from left to right).

CHAPTER V

EGRT TREATMENT PLANNING SCHEME

Treatment planning is an essential component in RT, as stated in Chapter 2. Any type of new radiation therapy modality should have an associated treatment planning solution to provide the capability of achieving IMRT-type planning modulation as in current conventional RT. The feasibility of tumor tracking and a primitive modulation method to compensate for attenuation have been demonstrated for EGRT using Monte Carlo (MC) simulations with a water phantom, physical phantom experiments, and a 4D digital patient model in Chapter 3.

In this chapter, we develop a planning scheme for EGRT to accomplish sophisticated intensity modulation based on an IMRT plan while preserving tumor tracking, thereby improving upon the basic EGRT treatment with escalated GTV dose without increasing dose to OARs. Both the XCAT phantom and clinical patient data are used for demonstration. We first briefly describe the design of a complete EGRT treatment with the proposed planning scheme. We then present the method of incorporating planning modulation into EGRT and associated evaluation studies with results. Finally we discuss other considerations, benefits, and limitations of this proposed EGRT planning scheme. Note that in this work, we assume EGRT is applied as an implementation of the motion-encompassing method, i.e. the ITV approach.

5.1 Treatment Scheme

Figure 5.1 illustrates a summarized workflow of the proposed EGRT treatment scheme which uses the proposed planning scheme.

The EGRT treatment scheme based on the ITV approach is composed of three major steps: simulation, pre-treatment, and treatment using the EGRT algorithms.

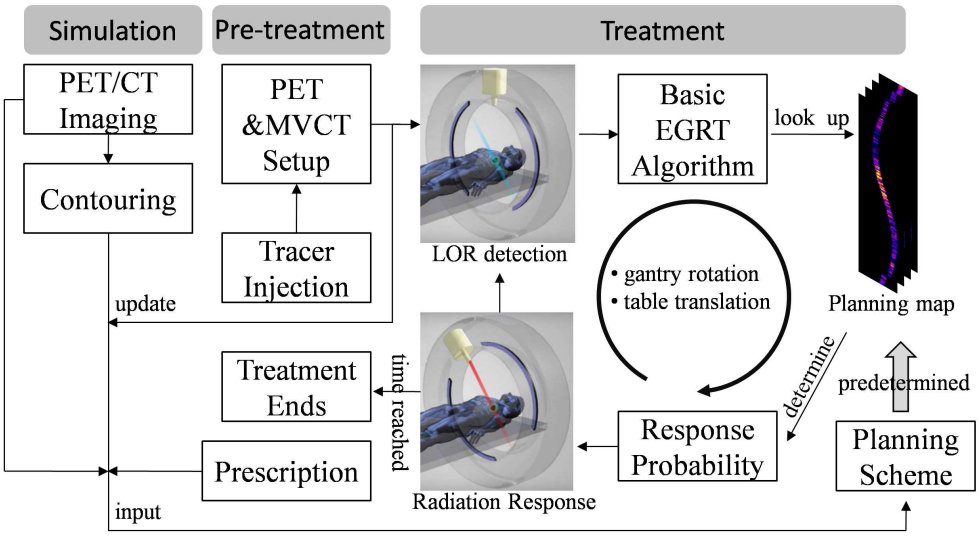

Figure 5.1: EGRT treatment scheme. The entire EGRT treatment is divided into three distinct components. Simulation and pre-treatment include the sequential procedures of imaging, contouring, tracer injection, and patient setup via PET/MVCT to update the planning map. The treatment component includes the two repeating operations of LOR detection and radiation response, which relies on the pre-computed planning map to provide the LOR response probabilities, i.e. leaf opening probabilities.

In simulation, the patient first undergoes PET/CT imaging for contouring and forming the initial treatment plan. Retrospective CT and/or breath-hold CT scans are used to obtain the desired data for planning. The maximum intensity projection can be determined from the 4DCT dataset to obtain the ITV encompassing the full extent of target movement. Margins are added to the ITV to define the PTV to account for patient setup error and residual motion uncertainty. The breath-hold CT image, contours, PET image, and dose prescription are used to calculate a planning map via EGRT's planning scheme (discussed in section 5.2). On the treatment day, the patient is first administered with a PET radiotracer and waits in a waiting room for the optimal uptake time as in a standard PET imaging protocol. The patient is then positioned on the treatment couch and a simultaneous PET/MVCT scan of short duration (< 2 min) is acquired with the EGRT system for alignment and calibration, and additionally to update the planning map (the tracer distribution change within

the treatment fraction is assumed to be small). The treatment is composed of two repeating operations: LOR detection and minimal-lag radiation response. The basic EGRT algorithm sifts out qualified LORs for responses. To achieve the desired intensity modulation, the treatment relies on the planning map to specify the LOR response probabilities and is described below.

5.2 The Proposed EGRT Planning Scheme

In this section, we develop a planning scheme for EGRT to achieve specific planning constraints/goals as in conventional optimized treatments. Two types of constraints are typically used in IMRT optimization: one for OARs which limits the maximum dose to a certain percentage of each volume, and one for the PTV which requires the delivery of a prescription dose with high dose conformality. We aim to demonstrate that, as compared with other ITV approaches, the same planning constraints can be met for OARs in EGRT based on the same IMRT plan. At the same time, the GTV dose can be escalated due to inherent tracking, with the dose reduced for the non-GTV portions within the PTV.

The proposed planning scheme is based on EGRT's unique treatment geometry, which involves the concept of sinogram space as described in section 2.5.2. Dose modulation can therefore be achieved via applying an LOR response probability to a particular sinogram bin which is used to decide whether to open the corresponding bMLC leaf for a qualified LOR. We refer to the probability distribution across all bins in sinogram space as the *planning map*.

5.2.1 The Overall Scheme

Under the geometric approximation of mapping LOR paths into sinogram space, the delivered dose of EGRT can be written as

$$d = D \cdot \Sigma \cdot b \tag{6}$$

where vector b has a length of the number of elements in sinogram space, and specifies the total number of qualified LORs for each sinogram bin in the EGRT treatment. Matrix D is a group of beamlet kernels. The jth column of D is the vectorized 3D dose distribution resulting from a beamlet with unit intensity along the LOR path specified by the jth element of the sinogram. Σ is the planning map in the form of a diagonal matrix, whose jth diagonal element corresponds to the response probability to be applied for the LORs that correspond to the jth sinogram bin. In other words, Σ represents the intensity modulation applied in EGRT.

The planning map Σ can be further decomposed into three daughter modulation maps as

$$\Sigma = \Phi(\Sigma^A \cdot \Sigma^P \cdot \Sigma^{X_m}) \tag{7}$$

where Σ^A, Σ^P, and Σ^{X_m} are all diagonal matrices whose diagonal elements represent modulation accounting for different purposes and have a range of [0 1]. They are referred to as the attenuation correction map, PET activity normalization map, and modified IMRT plan map, respectively. Φ is an operator that normalizes the resultant diagonal elements to have a maximum value of 1. The overall modulation contributed by Σ^A and Σ^P aims to compensate for a non-uniform LOR distribution before any other modulation is applied. Specifically, Σ^A represents the modulation to remove the attenuation effect and Σ^P represents the component to correct for the effect of a non-uniform PET activity distribution outside of the PTV. This can be due to non-specific uptake in tissue surrounding the target (e.g. FDG-uptake in the heart, liver and other organs, as well as uptake due to inflammation). Σ^{X_m} represents the main intensity modulation to be applied in EGRT and is derived from the IMRT plan of a conventional motion-encompassing treatment.

5.2.2 PET Activity Normalization and Attenuation Correction

One distinct feature of EGRT is that the delivery of radiation is *reactive* since it relies on detected LORs as the delivery medium. Therefore, if no modulation is applied and beamlet intensity/duration is constant, the resultant EGRT dose distribution essentially depends on the distribution of detected LORs, which can be non-uniform due to an inhomogeneous PET activity distribution and the non-isotropic attenuation of annihilation photons through the subject.

Non-specific and non-uniform uptake is commonly observed in conventional PET imaging. It is part of the information that PET images convey and therefore no correction is performed during the diagnostic imaging process. However, non-specific and non-uniform uptake in the background needs to be accounted for in EGRT treatments. This is due to the fact the LOR response rates are proportional to the aggregate activity along their response paths. Therefore, an inhomogeneous activity distribution yields a non-uniform LOR response distribution. To correct for this effect, we calculate a PET activity normalization map that is inversely proportional to the LOR detection rates in sinogram space. Specifically, the line integrals of activity are first efficiently pre-calculated using Siddon's algorithm [90] from the reconstructed PET images during pre-treatment for all sinogram bins. The PET activity inside the PTV region is set to zero before projections are calculated to remove bias from uptake in or near the moving GTV. We denote the minimum line integral of PET activity values across all non-zero bins as v^P_{min}. For sinogram bin j with associated line integral value v^P_j , its LOR response probability or bMLC leaf opening probability is given as:

$$p^P_j = v^P_{min}/v^P_j \tag{8}$$

where superscript P indicates the correction for the PET activity effect.

The same issue arises with the non-isotropic attenuation of annihilation photons, which also results in non-uniform LOR detection rates and therefore a non-uniform

radiation response distribution. Likewise, the attenuation effect needs to be corrected before any planning modulation is applied. Please refer to section 2.5.2.1 for a detailed discussion on attenuation correction in EGRT and here we present a brief review.

Similarly as with the PET activity normalization map, the line integrals of attenuation coefficients are first efficiently pre-calculated from the planning patient CT images (and updated from the pre-treatment PET/MVCT scan) for all sinogram bins. Let us denote the maximum line integral value across all bins as a^A_{max} . For sinogram bin j and a line integral value a^A_j, its leaf opening probability is given as:

$$p^A_j = e^{-a^A_{max}+a^A_j} \tag{9}$$

where the superscript A refers to attenuation effect correction. Both Eqns. 8 and 9 are determined heuristically and aim to remove their corresponding effects by compensating for lower LOR detection likelihood with higher LOR response probability, and vice versa.

5.2.3 Modified IMRT Plan

With the LOR response distribution made uniform through PET activity normalization and attenuation correction, EGRT can now incorporate a traditional IMRT plan to improve the dose performance. For the clinical patient case, we use the Pinnacle^3 workstation (Philips Healthcare, Fitchburg, WI) as our optimization engine. For the digital patient, this task is achieved using an optimization package called MOSEK (http://www.mosek.com/) and a beamlet-based optimization algorithm which aims to minimize the L2-norm of the difference between the calculated dose and the prescribed dose for given constraints [113, 115, 114], as in the following formula:

$$minimize \quad \sum_i \lambda_i (A_i x - d_i)^T (A_i x - d_i) \tag{10}$$

$$subject\ to \quad x \geqslant 0 \tag{11}$$

where the index i denotes different structures including PTV and OARs, λ_i is the relative importance factor [109], each column of matrix A_i is the beamlet kernel corresponding to the ith structure, x is a 1D vector that consists of row-wise concatenations of beamlet intensities for all fields, and d_i is the vectorized prescribed dose of the ith structure. The traditional aperture constraint that stems from the physical constraints of the MLC is not included since the EGRT delivery relies on a probability scheme which is not limited by such a constraint.

To reduce the field complexity and the intensity difference between adjacent fields (or firing points), which is also preferred in EGRT's probability-based delivery scheme, two regularization terms are added into formula 10:

$$minimize \quad \sum_i \lambda_i (A_i x - d_i)^T (A_i x - d_i) + \beta_1 \sum_{f=1}^{N_f} \sum_{u=2}^{N_u} (x_{u,f} - x_{u-1,f})^2 + \beta_2 \sum_{f=2}^{N_f} (\sum_{u=1}^{N_u} x_{u,f} - \sum_{u=1}^{N_u} x_{u,f-1})^2 \quad (12)$$

$$subject\ to \quad x \geqslant 0 \quad (13)$$

where β_1 is the penalty weight associated with the first regularization term which aims to reduce the complexity within each field while β_2 is the penalty weight of the second regularization term aiming to reduce the complexity between adjacent fields, N_f is the number of fields and N_u is the number of beamlets within a field. After intensity optimization based on formula 12, the resultant fluence map is converted into the IMRT plan map.

The IMRT plan map is optimized for conventional external beam radiation therapy. It is sub-optimal for EGRT since it does not take into account the GTV dose peaking effect in EGRT treatment. Therefore, dose to nearby OARs may be increased relative to the IMRT planning value, unless a modification to the original IMRT plan

is employed. To achieve the same planning constraints for OARs, we modify the original transformed IMRT plan map, which is implemented by multiplying an additional probability for sinogram bins whose corresponding spatial orientations intersect the OARs of interest. The specific probabilities are empirically chosen for different OARs with a typical range of [0.5 1], depending on their proximities to the GTV.

5.2.4 Workflow of EGRT's Planning Scheme

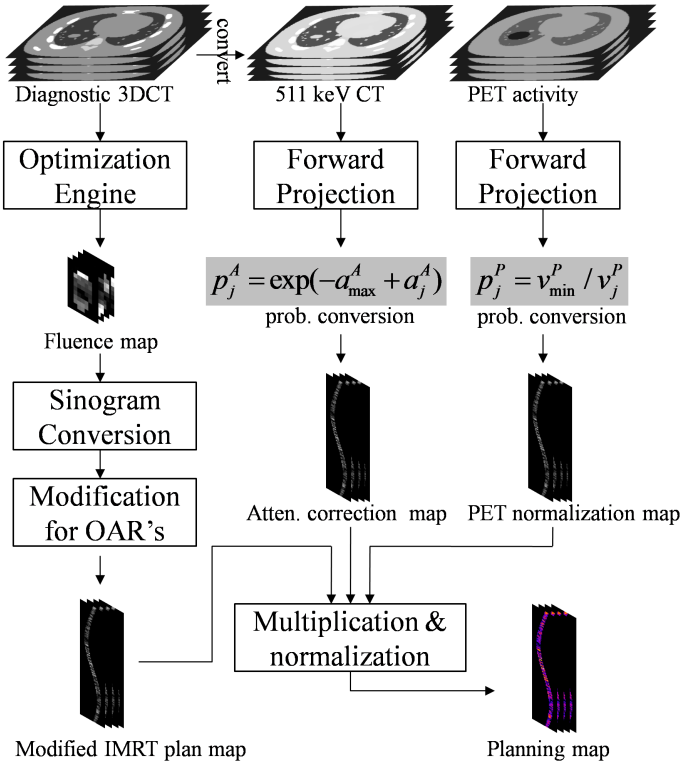

Figure 5.2: Calculation of the planning map. To obtain the final planning map, three daughter modulation maps need to be calculated first: a modified IMRT plan map, attenuation correction map, and PET normalization map. The final planning map is obtained as the product of these three maps with a subsequent normalization.

Figure 5.2 shows a workflow for calculating the EGRT planning map. The planning map is calculated as a multiplication of the modified IMRT plan map, attenuation correction map, and PET activity normalization map followed by normalization. These three maps are built in the same sinogram space of dose delivery and contain

the LOR response probability values to account for the corresponding types of modulation discussed above. To obtain the modified IMRT plan map, the stack of fluence maps are first calculated through conventional inverse planning optimization using simulation CT imaging as described above. The fluence maps are then interpolated and reshaped into sinogram space, and subsequently modified to further suppress dose to nearby OARs. The attenuation correction map is converted from the forward projected CT image based on Eqn. 9. A 511 keV CT image is used in this process, which can be transformed from the pre-treatment MVCT scan. Similarly, the PET activity normalization map is calculated from the projection of the pre-treatment PET scan, excluding the PTV region, based on Eqn. 8. For the clinical patient case, the reconstructed PET images are used as the estimate of the actual PET activity map.

5.2.5 EGRT Simulation Workflow

Simulation studies are performed with both a digital and a clinical patient with moving tumors in the lung region to investigate the performance of the proposed EGRT treatment. The same digital patient as in Chapter 3 is used. To simulate realistic emission data from the digital patient, the same GATE package is used. In the clinical patient case, raw list mode data from a PET/CT Discovery system (GE Healthcare, Waukesha, WI) are retrospectively used for the study, under an institutional review board (IRB) protocol. Both raw PET list mode data and reconstructed, binned 4DPET datasets are used in the simulation. The simulation of Linac dose delivery uses the same VMC++. Both VMC++ and GATE have been validated against well established MC codes and commercial PET systems, respectively.

To simulate a dynamic EGRT treatment as a complete motion management scheme, the simulation workflow for the clinical patient scenario is shown in Figure 5.3.

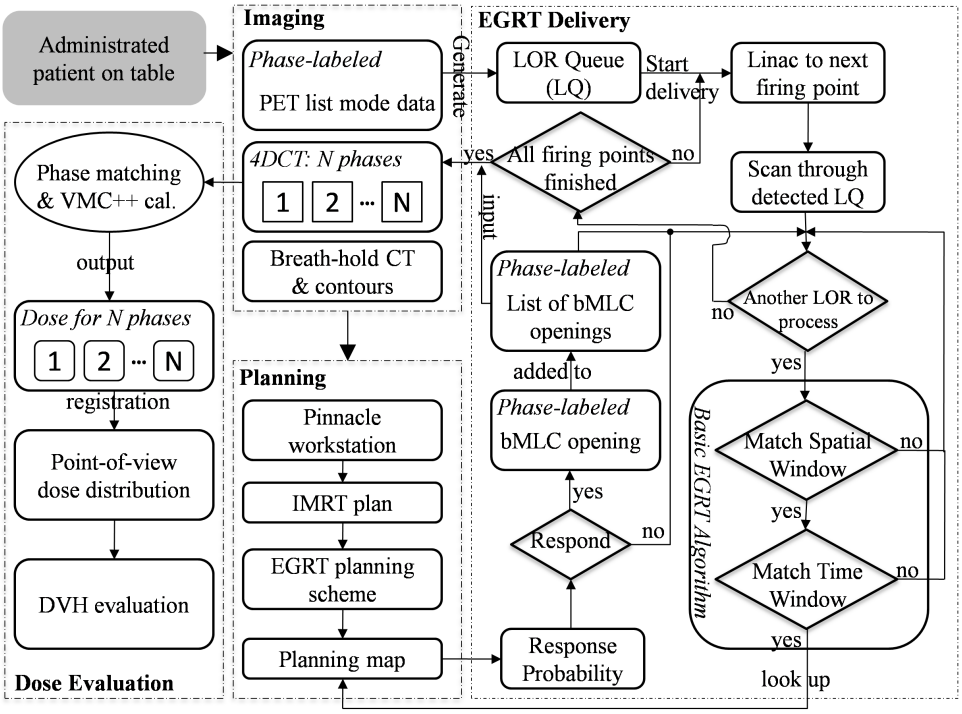

Figure 5.3: EGRT simulation workflow for the clinical patient case (starting from the shaded module on the top left). The workflow is divided into four major segments: imaging, planning, EGRT delivery, and dose evaluation. The first three segments describe a complete radiation therapy chain for moving tumors and the dose evaluation segment is designed to evaluate the dose performance of the treatment.

The entire workflow is segmented into four major sequential steps. The simulation starts from the imaging step where datasets of PET list mode, 4DCT and breath-hold CT images are acquired. PET list mode and 4DCT projection data are collected at the same time using a GE Discovery PET/CT scanner. The CT projection data are sorted based on the phases of the breathing trajectory obtained using the Varian RPM system. The PET list mode data are then synchronized with CT phases using the same breathing trajectory, referred to as phase-labeled PET list mode data. The imaging data are input into the planning step for the generation of the planning map to be fed into the EGRT delivery segment. The IMRT treatment plan with typical beam and field setup parameters is optimized using the Pinnacle[3] workstation. The final planning map is then calculated based on the proposed planning scheme.

The EGRT delivery step is used mainly to simulate the dynamic aspect of the EGRT treatment where tumor tracking and planning modulation are achieved. The EGRT delivery segment starts with the conversion of the phase-labeled raw PET list mode data into the LOR queue where each entry includes its timestamp, 3D Cartesian coordinates of the two LOR end-points, and phase number. When the dose delivery starts, the Linac goes through all firing points sequentially along the whole treatment helix. At each firing point, it scans through the LOR queue that can be detected by the 2-cm PET detectors at its current position and then checks whether each individual LOR meets the basic EGRT algorithm criteria (The PTV intersection criterion is implicitly implemented in the planning scheme). If one LOR is determined to be eligible for response, it will be decided to be responded to or not based on its response probability determined by the planning map according to its location in sinogram space. The consequent bMLC opening will be added to the list of bMLC openings. Once all firing points have been processed, the entire list of bMLC openings will be output, which specifies the complete set of information that defines the beamlet responses during the treatment including the spatial coordinates of the firing points, the leaf numbers that are opened, and the phase number of the 4DCT dataset at the time a leaf is opened.

Each entry of the list of bMLC openings will be matched with the 4DCT dataset based on its phase for subsequent VMC++ calculation in the dose evaluation step. The dose for each phase is obtained via summation of all the beamlet responses for the same phase. To calculate the total dose of a moving structure, dose maps of different phases are registered to the same reference phase through rigid image registration. The multiple dose maps are then summed to produce a point-of-view map relative to the moving structure, resulting in its accumulated total dose during the entire treatment.

The above workflow is different from that for the digital XCAT patient in the

imaging and planning steps. In the imaging step, the emission data are simulated using GATE and the phase information is known a priori. In the planning step, the IMRT plan is optimized using MOSEK and the inverse-planning algorithms as discussed in section 5.2.3.

5.2.6 Performance Evaluation

For performance evaluation, conventional 3D IMRT treatments are first designed for both the digital and clinical patient cases. In the digital XCAT case, the PTV is designed as the ITV plus 6 mm uniform margin added to account for patient setup and other uncertainties. In the patient case, the clinically defined PTV which contains the GTV motion is used. The OAR planning limits are based on the values recommended by the Quantitative Analysis of Normal Tissue Effects in the Clinic (QUANTEC) [65] and Radiation Therapy Oncology Group 0236 [96] for digital and clinical patients respectively. 256 fields are used to correspond with the EGRT treatment geometry. The resultant optimized fluence maps are then used to simulate a 3D divergent dose distribution. Conventional helical IMRT (hIMRT) treatments are also simulated as comparisons to both 3D IMRT and EGRT treatments. On one hand, hIMRT treatments intend to replicate the 3D IMRT treatment in the helical treatment geometry with a different source-to-axis-distance (SAD) by interpolating and reshaping the same IMRT plans. On the other hand, the hIMRT treatments use nearly the same system settings (i.e. the same bMLC system, the same number of firing positions, the same SAD, and the same firing geometry with a more suitable helical pitch) as EGRT treatments. The main difference is that EGRT opens the leaves according to the probability scheme using LOR-based guidance, while the hIMRT treatments deliver the dose with deterministic plan intensities as the 3D IMRT treatments. The purpose of including hIMRT in the current study is to understand if any of the performance benefits of EGRT over 3D IMRT are due to the helical geometry

of EGRT. The evaluation details pertaining to the individual studies are discussed below.

- **Digital XCAT patient**

  In the XCAT patient case, respiratory motion and heart motion are modeled with periods of 4.2 and 1 s, respectively, sampled in 12 phases. The GTV is modeled using an ellipsoid with a set of semi-axis lengths of 1.5, 1, 1.5 cm and placed in the right lung. The GTV motion path is based on the XCAT built-in 3D periodic tumor motion trajectory with typical lung motion behavior and peak-to-peak amplitudes of 16.6, 3.5, and 0.02 mm for SI, AP, and LM directions, respectively. Structures are contoured based on the phantom masks. The ITV volume is calculated as the union set of all GTV voxels. The PTV is designed as a 6 mm uniform extension of the ITV. The IMRT plan is optimized with a prescription of 70 Gy to 95% of the PTV. The table position covers a treatment range of 7 cm containing the whole PTV. The treatment time is 1200 s, resulting in a table speed of approximately 0.006 cm/s. The first phase of the generated 511-keV attenuation phantom, 110-keV attenuation phantom, and PET activity phantom are used for the calculation of the attenuation correction map, IMRT plan map, and PET normalization map, respectively. The tumor, lung, and background activity uptake ratio is set to be 8:0.5:1 with the base background activity set to be 3 kBq/cc. The phantom geometry can be seen in Figure 5.6.

- **Clinical patient**

  The clinical patient datasets of 4DCT, 4DPET, and breath-hold CT are retrospectively collected at the Stanford Cancer Institute under an IRB protocol. The tumor is staged as a metastasis of breast cancer in the left lung region,

with a GTV size of 3.33 cm^3 averaged over all six motion phases. The tumor motion has estimated peak-to-peak amplitudes of 8.5, 4.5, and 2.5 mm for SI, AP, and LM directions, respectively. The raw PET-list mode data is corrected with a 1.02 cm systematic shift in the longitudinal direction after manual registration of the 4DPET and 4DCT volume using RT Image (http://rtimage.sourceforge.net/). Structure contours are made by a designated specialist on the breath-hold CT, which is used for the IMRT plan modulation map calculation with the help of the Pinnacle^3 workstation. In observation of the spine's proximity to the GTV, the IMRT plan is optimized with a prescription of 54 Gy to 95% of the PTV. Optimized fluence maps are output without any modifications for the feasibility of delivery. The breath-hold CT is converted into a 511 keV CT volume for the attenuation correction map calculation. To obtain the PET activity normalization map, the first phase of the reconstructed 4DPET volume is interpolated to coincide with the breath-hold CT volume in terms of resolution and position. The table position covers a treatment range of 9 cm and the treatment time is 1200 s, resulting in a table speed of 0.0075 cm/s. Since only 5 minutes of PET data are acquired per bed position, PET-list mode data are looped with simulated FDG decay for re-use. GTV is manually registered to each 4DCT phase similarly using RT Image to evaluate its accumulated dose during the entire treatment. The phantom geometry can be seen in Figure 5.9.

Figure 5.4 illustrates an example of the fluence maps output from Pinnacle^3 and the IMRT plan map converted from the fluence maps.

A summary of major treatment as well as GATE, and phantom simulation parameters for performance evaluation is shown in Table 5.1 and 5.2, respectively[1].

[1]TWG. = takeWinnerofGoods, Bg. = Background, Sino. = Sinogram, resol. = resolution, ITV/PTV = ITV to PTV

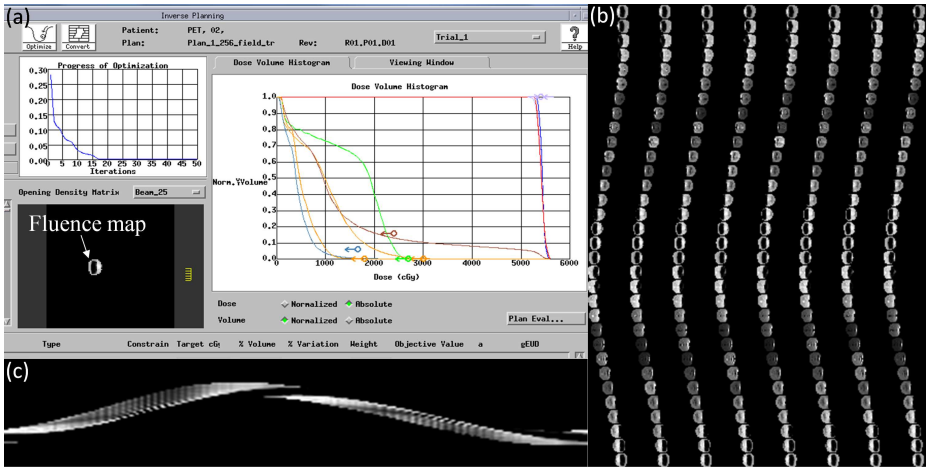

Figure 5.4: Calculation of the IMRT plan map using Pinnacle^3. (a) Pinnacle^3 interface for inverse planning. (b) 256-field fluence maps. (c) The central sinogram of the IMRT plan map.

Table 5.1: Major treatment and GATE simulation parameters

Category	Parameter	Value	Parameter	Value
EGRT	Detector extent	2 cm	iso Leaf aperture(x-y)	0.5 cm
	Detector coverage	$2 \times 90°$ arc	iso Leaf aperture (z)	0.5 cm
	PET ring radius	50 cm	EGRT spatial window	$\pm 0.5°$ arc
	Rotating frequency	1 Hz	EGRT time window	500 ms
	Linac radius	60 cm	hIMRT pitch	0.2
	Collimator radius	50 cm	Radiotracer	FDG
	Collimator leaves	64	Firing positions	256
3DIMRT	SAD	100 cm	Field number	256
GATE	Version	V5.0.0.p01	Light decay time	40 ns
	Coincidence window	10 ns	Energy resolution	0.26
	Scatter threshold(keV)	350,650	Coincidence policy	TWG.

5.3 Results

5.3.1 Digital XCAT Patient

Figure 5.5 shows the dose distribution and DVH comparison of 3D IMRT and hIMRT treatment using the same treatment plan. Motion is not simulated in this case. The dose distribution is normalized to have the same mean lung dose. The slightly inferior performance of hIMRT, when compared to 3D IMRT, is likely due to delivering a divergent IMRT optimized plan in a helical geometry. The SAD difference also contributes to this difference but the influence is small. Overall, the dose performance

Table 5.2: Major phantom and patient simulation parameters

Category	Parameter	Value	Parameter	Value
XCAT	Respiration period	4.2 s	Phantom size	$256 \times 256 \times 35$
	Respiration phases	12	Voxel resolution	$2 \times 2 \times 2$ mm^3
	Couch travel range	7 cm	Dose grid size	$4 \times 4 \times 4$ mm^3
	GTV size	9.40 cm^3	Sinogram bin size	$256 \times 64 \times 35$
	ITV size	17.01 cm^3	Uptake ratio	8: 0.5: 1
	ITV/PTV margin	6 mm	Bg. activity	3 kBq/cc
	Treatment time	1200 s	IMRT field size	5×2 mm^2
	Prescription dose	70 Gy		
Patient	Respiration phases	6	Phantom size	$512 \times 512 \times 40$
	Aver. GTV size	3.33 cm^3	4D-CT resol.	$0.98 \times 0.98 \times 2.5$ mm^3
	Couch travel range	9 cm	Breathhold resol.	$0.98 \times 0.98 \times 1.25$ mm^3
	ITV size	5.97 cm^3	Dose grid size	$3.92 \times 3.92 \times 2.5$ mm^3
	Treatment time	1200 s	Sino. bin size	$256 \times 64 \times 40$
	IMRT field size	5×2.5 mm^2	Uptake SUV	6 (GTV), 1(Bg.)
	PTV size	16.8 cm^3	Prescription dose	54 Gy

of 3D IMRT and hIMRT is similar for both GTV and OARs. Since hIMRT treatment uses exactly the same treatment geometry as EGRT, differences in performance between 3D IMRT and EGRT should be largely independent of the change from a divergent to helical geometry.

Figure 5.6 illustrates the GTV point-of-view dose maps assembled from all 12 motion phases for 3D IMRT, raw EGRT, and EGRT with the planning scheme, as well as the associated DVH curves. The dose distribution is normalized to have the same mean lung dose. 133,288 and 17,818 beamlet responses have been generated for the two EGRT treatments, respectively. Note that the dose increase to nearby OARs due to the EGRT dose peaking effect is not accounted for by modifying the IMRT plan in both EGRT treatments. Without the proper planning scheme implemented, raw EGRT cannot outperform 3D IMRT due to the fact that dose is distributed more toward the lung rather than the heart. EGRT with the planning scheme is able to deliver a better dose distribution to the target, although at the price of increased heart dose due to its proximity to the GTV.

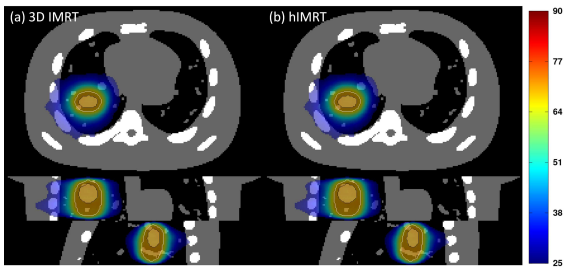

(a) Dose Distribution

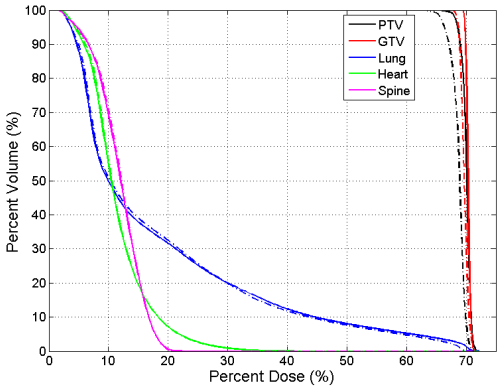

(b) DVH

Figure 5.5: Dose distribution and associated DVH comparison of 3D IMRT and hIMRT. The PTV and GTV are contoured using solid lines in the dose distributions. In the DVH plot, 3D IMRT and hIMRT are represented as solid lines and dashed-dotted lines, respectively.

Figure 5.7 shows the comparison of 3D IMRT, and planning scheme-implemented EGRT without or with modification for additional modulation to the heart and spine. When additional modulation is enabled, the number of beamlet responses is reduced from 17,818 to 15,805. Heart dose is suppressed with additional modulation (see arrow-pointed dose distribution). Compared with the 3D IMRT treatment, EGRT achieves a 15.1% relative increase in dose to 95% of the gross tumor volume (GTV) and a 31.8% increase to 50% of the GTV while the OAR doses are kept similar or lower for EGRT. This comparison shows that dose increases to nearby OARs can be suppressed with additional modification to the original IMRT map with minor dose degradation to the target.

Figure 5.8 depicts the dose maps of all 12 simulated phases for EGRT with the

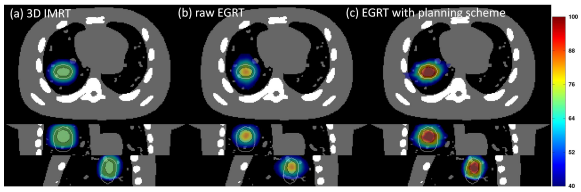

(a) Dose Distribution

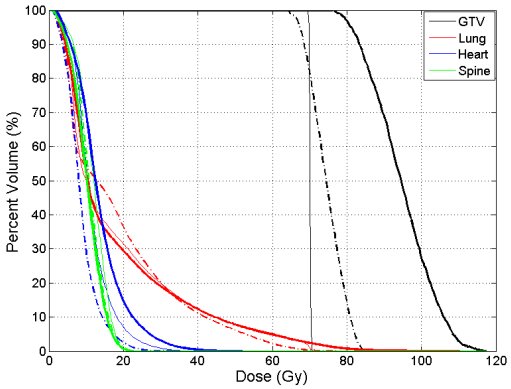

(b) DVH

Figure 5.6: Comparison of 3D IMRT (thin solid line), raw EGRT (dashed-dotted line), and EGRT with the planning scheme that does not include modification for additional OARs modulation (thick solid line).

planning scheme (i.e. Figure 5.7(c)) in both coronal and sagittal views. The results indicate that in spite of the dose *noise* introduced due to the reduced number of beamlet responses, tumor tracking is largely preserved.

5.3.2 Clinical Patient

Figure 5.9 shows the comparison of 3D IMRT and planning scheme implemented EGRT with additional modulation on spine, heart and esophagus. 32,086 beamlet responses have been generated for the EGRT treatment. Compared with the 3D IMRT treatment, EGRT yields a 15.2% relative increase in dose to 95% of the GTV and a 20.7% increase to 50% of the GTV while OAR doses are kept similar or lower for EGRT. Note that the challenging sparing of spine achieved in 3D IMRT is retained in EGRT with the proposed planning scheme.

Figure 5.10 shows the dose maps of all 6 simulated phases for EGRT treatment

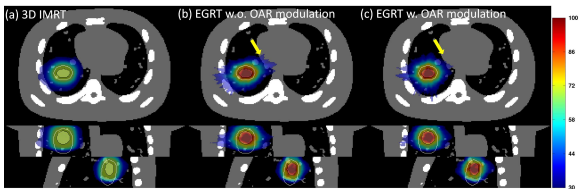

(a) Dose Distribution

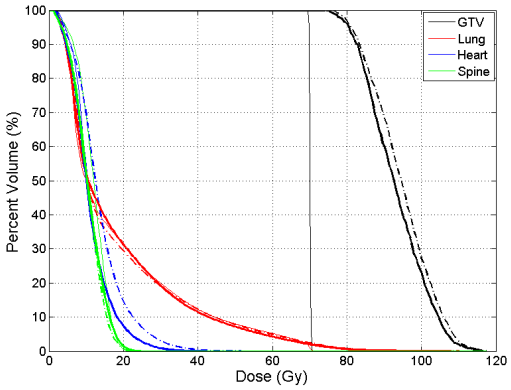

(b) DVH

Figure 5.7: Comparison of 3D IMRT (thin solid line), EGRT with planning scheme that does not include (dashed-dotted line) and includes (thick solid line) additional OAR modulation.

in both coronal and sagittal views. Unlike the XCAT patient case in which PET data and CT phases are ideally matched a priori, such matching in the patient case is not guaranteed due to motion and breathing changes in the sequential PET/CT scan and the uncertainties in PET and CT phase sorting based on external surrogate tracking. Nevertheless, the results still show that tumor tracking is preserved when the planning scheme is incorporated.

5.4 Discussion

In this work, we implement the EGRT concept as a complete motion management scheme that is able to incorporate IMRT plan modulation. Due to the inherent tracking capability of EGRT, the proposed treatment can significantly improve the dose performance of the conventional ITV approach while still preserving its ease of implementation in each step of the imaging, planning, and delivery therapy chain.

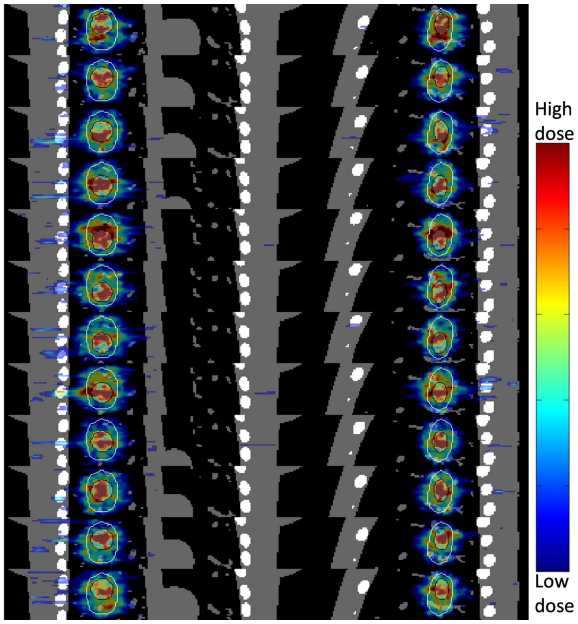

Figure 5.8: Tumor tracking of EGRT with the planning scheme. Both PTV and GTV are contoured to show the dose tracking. The dose map of each phase is displayed with an individually optimized window.

In the current implementation of EGRT, a few items require further consideration and discussion. The planning scheme entails the discarding of a portion of beamlet responses. Dose maps showing the tumor tracking of each phase can therefore be *noisy* as shown in the XCAT patient case. This effect is less pronounced with a smaller number of phases and higher overall activity levels as in the clinical patient case. In either case, the point-of-view dose map is representative of the effective dose for each structure and this is what is used to calculate the DVH curves.

In the evaluation studies, a 256-field IMRT plan is used rather than a conventional plan which typically has 7-12 fields. This is due to the fact that EGRT favors a plan that spans all angles to make full use of LOR data. The helical geometry provides more degrees of freedom than a conventional geometry due to the large number of fields used [10]. Therefore, compared with a conventional step-and-shoot IMRT treatment, EGRT possesses increased flexibility in planning a treatment. The algorithms developed for arc therapy or even new IMRT planning methods tailored

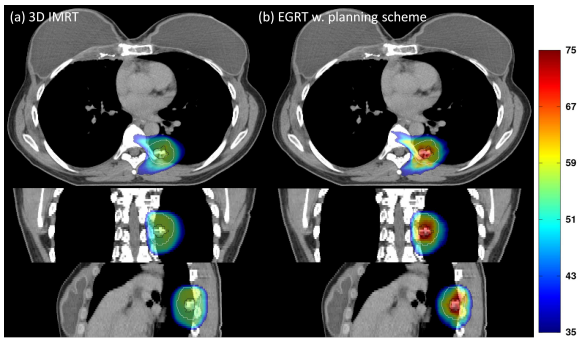

(a) Dose Distribution

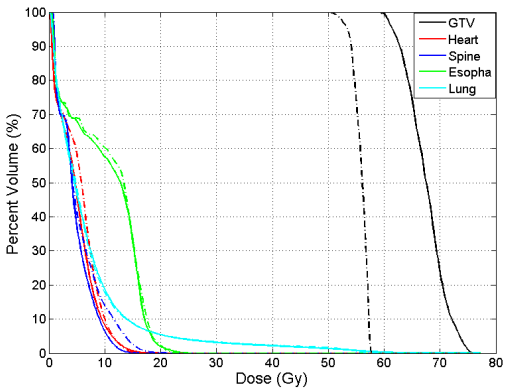

(b) DVH

Figure 5.9: Comparison of 3D IMRT (dashed-dotted line) and EGRT with planning scheme (solid line) for the clinical patient case.

for EGRT delivery can be used to improve EGRT's performance. Additionally, the intensity/duration of the beamlet responses can also be modulated to give further flexibility for EGRT's capability to incorporate planning modulation. Also note that the IMRT plans used in this study were optimized for a divergent geometry. Future work will involve development of a treatment planning system optimized for EGRT's helical geometry.

The proposed planning scheme provides the insight and basis for the future development of a fully characterized EGRT planning system. In order to achieve desired intensity dose modulation without interference, corrections for attenuation and non-uniform PET activity are necessary. Moreover, in spite of the fact that the EGRT

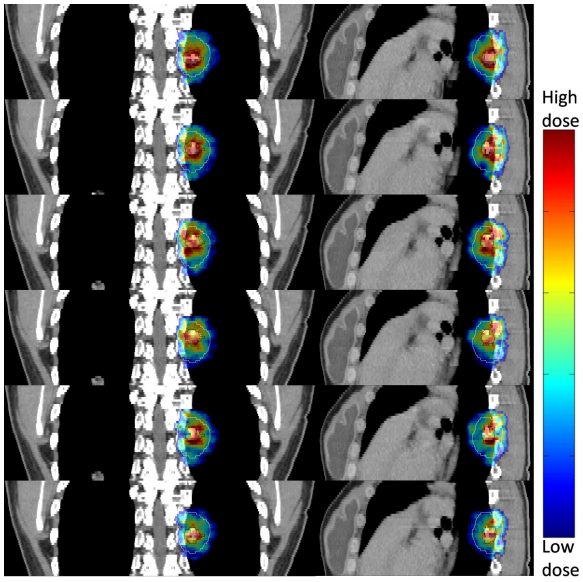

Figure 5.10: Tumor tracking of a breast cancer lung metastasis under EGRT with the planning scheme. The PTV and GTV are contoured for positional reference and target motion delineation, respectively. The dose maps are displayed with the same window [0.5 0.85] relative to the maximum GTV dose across all phases.

delivery relies on the statistical detection of LORs, a deterministic intensity modulation can be approximately achieved. Modifications to the IMRT plan ensure that clinical constraints for OARs can be met. The achievement of dose conformality to the GTV remains an issue for EGRT. The dose peaking effect is a natural result of the radiation *backprojection* principle in EGRT. This technique may be well suited to situations in which an integrated boost dose is desirable [23].

The current proposed planning scheme illustrates a general way to incorporate intensity modulation into EGRT. Although it is evaluated within the context of motion-encompassing methods, the planning scheme can be applied for other applications including gating and tracking methods without major modification to similarly achieve GTV dose escalation. This is due to the fact that the plan intensity weights that would have been delivered to the margins are effectively reduced in EGRT. The planning scheme also accounts for uncertainties beyond tumor motion. For example, the tumor may shrink during the treatment course and this is not accounted for in the

conventional ITV approach unless a patient is re-imaged and re-planned. However, since the planning scheme allows EGRT to concentrate the dose to just the GTV, normal tissue sparing will likely be better if the GTV size is reduced, or equivalently the dose to the GTV can be further increased.

Finally, it should be noted that in the evaluation scheme, it is implicitly assumed that the motion can be or should be divided into phases. However in fact, tumor motion can be quite irregular, even for a lung tumor. Therefore, any 4D tracking based methods with the phase division assumption is subject to the challenges of motion irregularity during the imaging or delivery process. In contrast, the tumor tracking and proposed planning scheme in the EGRT treatment is not limited by the phase theory. EGRT therefore provides a potential solution to deal with the different types of motion, periodic or random, encountered over all treatment sites. Also note that in the simulation study presented in this work, 4DCT is only acquired for evaluation purposes. In an actual EGRT treatment, a slow CT can be used to obtain the ITV instead, thereby avoiding the increased dose and complexity of 4DCT imaging. In fact, each step of imaging, planning, and delivery of the proposed EGRT treatment can essentially be regarded as 3D, with the tumor tracking taken care of automatically. The complexities and uncertainties associated with 4D imaging and delivery can be significantly reduced or in some cases eliminated.

5.5 Conclusion

In this work, we design a planning method for EGRT to achieve intensity modulation with the capability of incorporating a conventional IMRT treatment plan. We proposed a detailed treatment scheme based on this planning method and evaluate it within the context of the motion management strategy where the tumor motion uncertainty is managed by an encompassing volume. Simulation studies are performed on both digital and clinical patients. Emission data from both MC simulation and

a commercial PET/CT scanner has been used for validation. Compared to the ITV approach, EGRT outperforms with a dose increase of more than 15% to the moving target while the dose levels of OARs are kept similar or reduced. With the capabilities of achieving both tumor tracking and intensity modulation, EGRT has the potential to enable true biological targeting and guidance in radiation delivery.

CHAPTER VI

DISCUSSION AND CONCLUSION

6.1 Discussion

6.1.1 Image-based EGRT

As mentioned in Chapter 2, the concept of EGRT is broad and thus not limited to any specific type of dose delivery method or geometry. The work presented in previous chapters has primarily focused on demonstrating feasibility and applications of LOR-based EGRT using a helical dose delivery geometry. To illustrate other possible EGRT implementations, this section will discuss the design and geometry of image-based EGRT.

As previously stated, image-based EGRT aims to reconstruct a PET image based on LOR data generated through subsecond acquisition and then applying a tumor localization algorithm to identify and delineate tumor location using the resulting image for conventional on-board treatment guidance. Figure 6.1 illustrates two similar system designs modified from the conventional Linac for image-based EGRT.

The current conventional Linac system has an on-board x-ray imager (OBI). Two different designs are therefore proposed with and without the OBI. As indicated in Figure 6.1, θ_1 and θ_2 are denoted as the angular coverage of one PET detector arc in the two arrangements. Due to the incomplete data coverage in the sinogram, the two designs have different strengths and drawbacks. The system without OBI has a total angular coverage of $2\theta_1$. Each PET detector has a large effective field of view (FOV) and may show advantages in treating peripheral tumors. The system with OBI has a total angular coverage of $4\theta_2$, which is more evenly distributed around the patient. With the same total data coverage, the system with OBI is expected

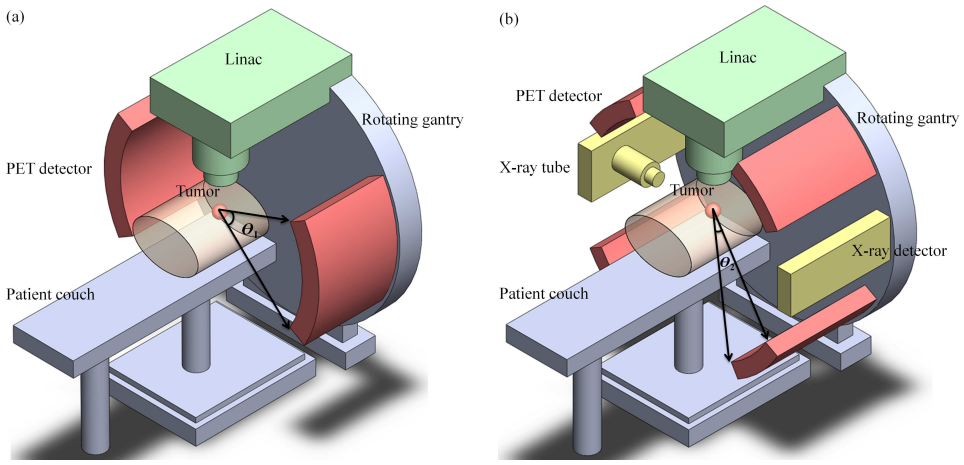

(a) EGRT system without OBI (b) EGRT system with OBI

Figure 6.1: The proposed image-based EGRT system design.

to obtain PET images with fewer artifacts and therefore demonstrate higher tumor localization accuracy.

A preliminary study based on a prostate tumor case and the system design without OBI (a similar design as LOR-based EGRT) is conducted to test the potential use of image-based EGRT for tumor tracking purposes. The prostate phantom used here is the same as in Chapter 3. The preliminary results are shown in Figure 6.2 and 6.3.

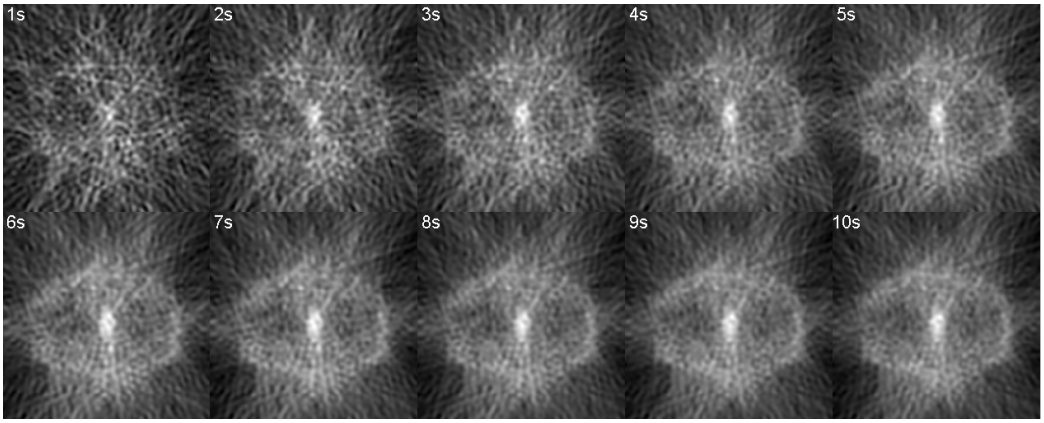

Figure 6.2: 3D PET reconstructed images (imaging time: 1, 2, ..., 10 s) using 3D parallel non-filtered back-projection reconstruction algorithm. Shown is the tumor's central slice from an axial view.

The results indicate that image-based EGRT is very promising for the application of tumor tracking. Note that the reconstruction technique used here is a simple 3D

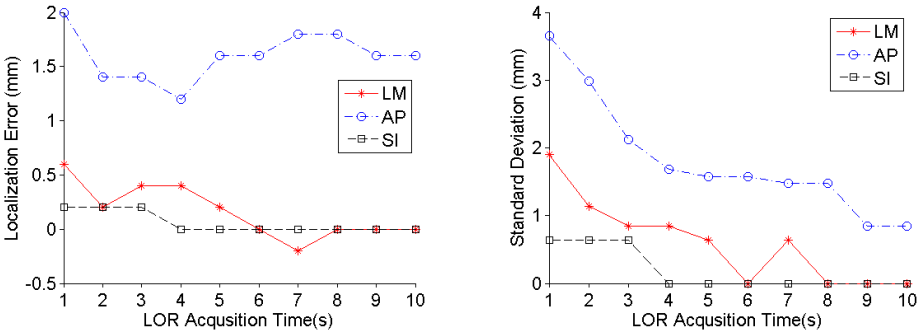

(a) Localization accuracy (b) Standard deviation

Figure 6.3: Localization accuracy and standard deviation for Figure 6.2. SI localization has the highest accuracy and precision, since the reconstruction resolution in the SI direction is 2 mm while the recon resolution in the AP and LM directions is about 7.8 mm. In the LM and SI directions, SI localization converges to the highest accuracy and precision when the acquisition time is greater than 8 seconds. In the AP direction, the localization accuracy has a bias and it is likely due to signal attenuation in the LM direction (due to long body axis and bone attenuation).

parallel backprojection algorithm. Other researchers have proposed more advanced iterative reconstruction algorithms which have shown improved tracking accuracy for subsecond timescales [112].

Figure 6.4 shows the proposed treatment scheme of image-based EGRT in a fixed gantry IMRT system. Before the treatment fraction starts, the FDG radiotracer is administrated to the patient. For each treatment field, PET images are first generated from the incomplete LOR data and compared with the planning CT image to determine the tumor location. The treatment plan is then modified accordingly to compensate for patient setup error and the prescribed dose is delivered. In the case of significant patient motion, the EGRT method is able to provide near real-time tumor tracking. During treatment, the PET detectors continuously detect LORs and the PET images are updated at short time intervals. The dose is delivered based on the phase of tumor motion as in a conventional gating method.

The performance of image-based EGRT therefore mainly depends on the success of two major components: accurate tumor localization and improved dose delivery

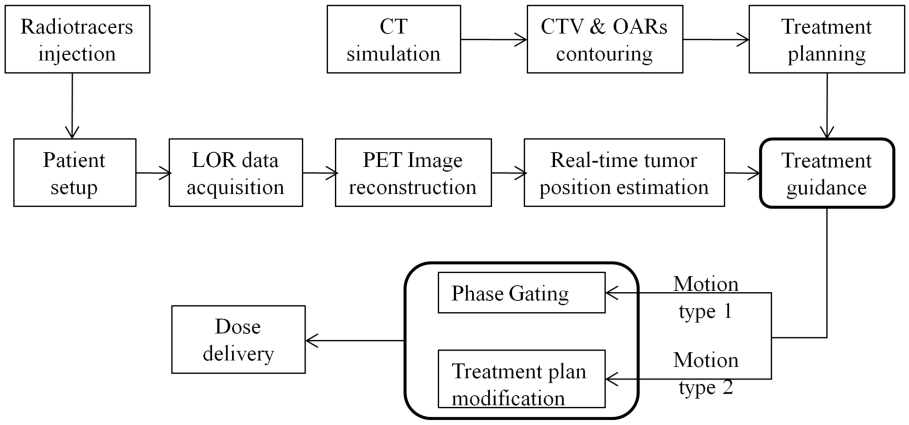

Figure 6.4: EGRT treatment scheme in fixed gantry IMRT.

with a modified treatment plan based on the updated tumor location. In the localization step, a major challenge arises due to inaccurate PET reconstruction from the incomplete LOR data measurement. PET images reconstructed from incomplete data contain strong streak artifacts, and they do not accurately depict the tumor distribution. Nevertheless, in EGRT, the on-board PET images are used only to determine the tumor transformation from the planned position, while the tumor distribution can be obtained from the planning CT images. As such, accurate tumor localization is still achievable in spite of the low quality of on-board PET images, as shown in Figure 6.2 and 6.3. Moreover, iterative algorithms which are not sensitive to truncation of projection data can be applied in this case. With reconstructed images which typically have higher intensity for tumor volumes, a convolution-based cross correlation algorithm can be used to localize the tumor, as is the case for the previous preliminary study. The second challenge arises when the tumor localization step determines that there is indeed a change in tumor location. If the location change is small and the beamlet kernel is assumed to remain unchanged, the change can be accounted for by modifying the treatment plan accordingly via a mathematical transform.

6.1.2 Other Considerations

Important discussions on EGRT's limitations, benefits, and future work have been presented and can be found in section 3.1.4, 3.1.7, and 5.4. In this section, we provide supporting evidence or further discussion for three important issues which have not been fully discussed in the planning scheme study.

6.1.2.1 9-field IMRT Plan

The first issue is the reason why we compare EGRT with a 256-field IMRT in Chapter 5. We explained this is due to the fact EGRT favors a plan that spans all angles to make full use of LOR data. One may then wonder why not use VMAT plan for comparison in this case. In fact, a comparison with the VMAT plan seems more appropriate. However, while a comparison with VMAT is useful, the 256-field IMRT plan presented in this work serves as a good approximation [77]. In addition, the 256-field IMRT plan corresponds well with EGRT's 256-firing-position geometry enabling a direct comparison for implementation. Additional concerns may arise from the fact that we did not compare EGRT with a typical 7-field or 9-field IMRT. Here we present a comparison of 9-field and 256-field IMRT treatments below (Figure 6.5) for further clarification.

These two plans are optimized for the same dose prescription using the Pinnacle system. As shown in Figure 6.5, for similar dose performance to the target, the 256-field plan does a better job than the 9-field plan when evaluating the performance using the maximum dose delivered to OARs as the criterion (Note that during optimization, the planning constraints for OARs are also specified using the form of maximum dose). The result is as expected since a 256-field IMRT plan generally achieves better or at least as good performance as a conventional 7-9 field plan due to the increased degrees of freedom for optimization. Therefore, this comparison demonstrates that a direct comparison of EGRT with 9-field IMRT would lead to the same

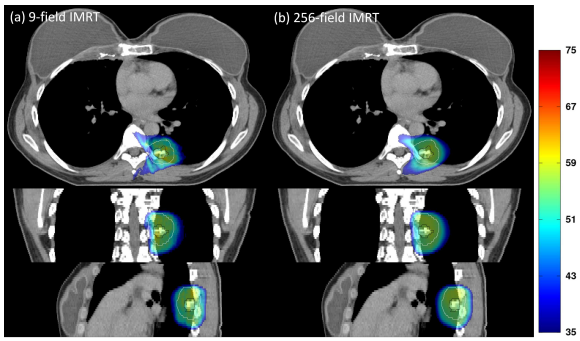

(a) Dose Distribution

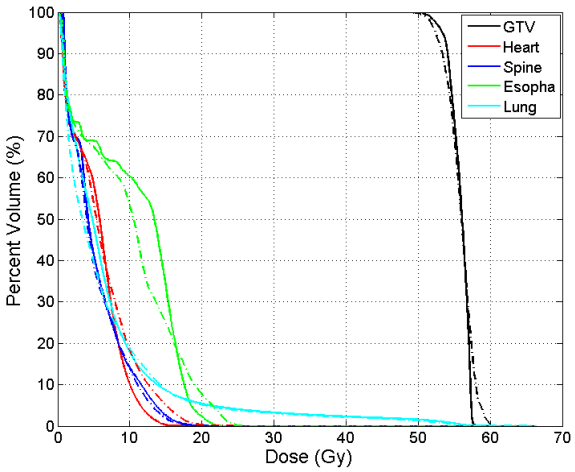

(b) DVH

Figure 6.5: Comparison of 9-field (dash-dotted line) and 256-field (solid lines) IMRT treatment based on the same planning goals.

conclusion as in Chapter 5.

6.1.2.2 Uniformity Constraint in IMRT Optimization

The second issue comes from the fact that uniformity and maximum target dose constraints are used in the IMRT optimization. Due to the nature of the EGRT delivery there are no such constraints. One may be concerned if the IMRT plans are re-optimized with only a minimum dose constraint not worrying about uniformity or maximum dose, the GTV DVH of the IMRT treatment will look more like the EGRT. In addition, dose to OARs may be reduced in IMRT when the uniformity penalization is removed so that the central claim of EGRT's dose escalation may no longer hold

true.

In fact, the comparison of IMRT and EGRT is fair and the claims in this work are valid based on the following reasons. First, the study aims to demonstrate the proposed planning scheme for EGRT as an implementation of the motion-encompassing method, i.e. ITV approach, in a realistic clinical scenario. Therefore, the IMRT method for comparison is designed in the same way as it would be in the clinical ITV approach. The uniformity constraint is necessary since a uniform prescription coverage of the PTV is considered optimal in the conventional ITV approach where tumor tracking is absent.

Secondly, in the original comparison, EGRT is implemented based on the IMRT plan that is optimized with a uniformity constraint. Therefore, the effect of a uniformity constraint is also *translated* to EGRT performance. The fact that EGRT delivers more dose to the tumor with similar OAR sparing is mainly because of the dose delivery mechanism used. EGRT tracks each positron emission LOR and selectively responds. Such a physics-based approach naturally results in more dose concentration inside the tumor. If a different IMRT plan (e.g. without the uniformity constraint) is used as an input to EGRT, then further dose concentration can be achieved.

To support our argument, we design studies for further clarification. Using patient data, we re-optimize an IMRT plan using the Pinnacle optimization engine with no maximum and uniformity dose constraints. To achieve the best possible performance of IMRT, the dose distribution is simulated using this IMRT plan assuming no tumor motion and setup error (except the registration error between the planned CT and 4DCT), referred to as *ideal tumor tracking* in our results presented below. We then implement the EGRT treatment using the new IMRT plan and the proposed scheme as described in Chapter 5. Tumor motion is still simulated in the EGRT treatment.

Figure 6.6 shows the dose distribution and DVH comparison of IMRT and EGRT

treatment using the new optimization. Two important observations can be made: (a) EGRT achieves GTV dose escalation over IMRT treatment with *ideal tumor tracking* without increasing dose to the OARs; (b) more importantly Conclusion (a) is true despite the fact that a non-uniform IMRT plan is used. Note the reason that the dose increase is not as large as that in Chapter 5 is because there is no tumor tracking in the original IMRT treatment while here perfect tracking is assumed in the IMRT treatment.

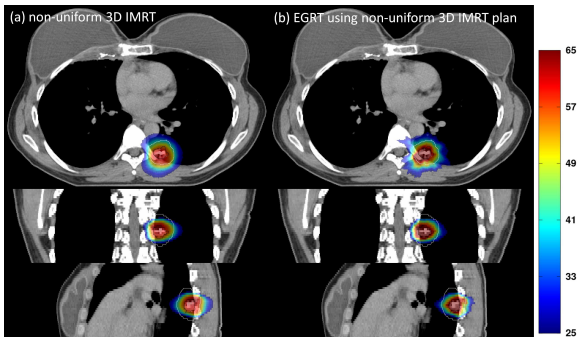

(a) Dose Distribution

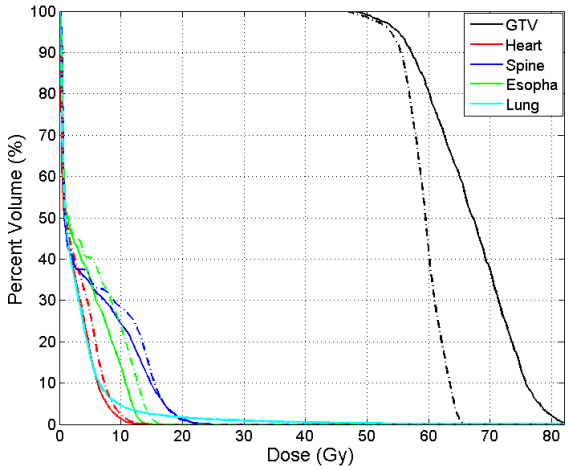

(b) DVH

Figure 6.6: Dose distribution and DVH comparison of IMRT treatment with ideal tracking and non-uniform plan (dash-dot lines) and EGRT treatment based on the same plan with EGRT-tracking (solid lines).

6.1.2.3 Tumor Dynamic Changes

The third issue is raised in considering dynamic tumor changes during the course of RT. For example, researchers have reported significant reduction in the tumor uptake of radiotracers during the entire treatment course. Complete degradation of PET tracer uptake in the tumor or conversely, high tracer uptake in the normal tissue directly adjacent to the GTV due to inflammation have also been observed. One might be concerned that EGRT cannot address dynamic changes since the EGRT method relies on PET signal for the radiation delivery.

It should be noted that in the current design of an EGRT treatment, a tumor-to-background uptake ratio of >1 is required to achieve dose benefits. It is correct that the EGRT performance degrades if the tumor uptake decreases during the treatment course. In previous studies, we implicitly assume that EGRT is primarily used for hypofractionated radiation therapy such as SBRT, where safe dose escalation is achieved by EGRT due to its excellent tumor tracking capability. Studies have shown that within the time frame of several treatment fractions, the maximum standard uptake value (SUV_{max}) inside the tumor volume either decreases by a small amount or in some cases even increases due to suspected hypoxic changes [40, 100]. As such, we are confident that sufficient emissions from the tumor volume are present when EGRT is used in a hypofractionated scenario.

It is true that tumor uptake may considerably change during the long treatment course of conventional fractionated radiation therapy. This change is largely patient specific [100]. In these scenarios, we will require multiple PET scans on different days of radiation therapy to monitor the variation of tumor uptake. As a matter of fact, PET has played an increasingly important role in monitoring radiation therapy [5, 41]. We can use the PET images to customize EGRT plans for better treatment performance. For example, instead of applying a constant fraction dose (e.g. 2 Gy) in a

treatment course, a theoretically more reasonable fraction dose scheme can be designed based on the tumor's unique radiation response (e.g. small/medium fraction dose for tumors showing complete/partial metabolic response, and a large fraction dose for stable or progressive metabolic disease). In rare cases, if PET tracer concentration in the tumor completely degrades and a radiation oncologist concludes that further therapy is necessary, treatment can be switched from EGRT to conventional therapy.

In Chapter 5, we focus on the engineering and algorithmic aspects of our EGRT technique. A detailed investigation on the above issues is beyond the scope of this dissertation, but of high interest in our next-phase research of EGRT.

6.2 Concluding Remarks

The advent of MLC, IMRT, IGRT, and increased computer processing power for advanced, image-based treatment planning methods, have greatly advanced the techniques for delivering modern radiation therapy. However, the sub-millimeter precision of these delivery systems is compromised by treatment uncertainties which may arise from many factors. The main uncertainties include intrafractional and interfractional tumor motion, patient setup error, tumor volume delineation, and unpredictable tumor volume change in response to radiation. They constitute the major challenges of current RT treatment limiting treatment effectiveness.

To realize the full potential of radiation treatment that is constrained by such uncertainties, many methods have been proposed to alleviate the problem and have shown success to a certain extent. However, even state-of-the-art tumor tracking methods have significant disadvantages that are essentially unavoidable. To eliminate treatment uncertainties, the invisible tumor needs to shine brightly during radiation therapy. If tumors could directly *signal* their location during treatment, radiation can be delivered with the highest confidence and the best treatment outcome can be

achieved.

To accomplish the above treatment goal, inherent fusion of imaging and therapy during treatment is required. With this thought in mind and inspired by the physical principle of emission imaging for cancer diagnosis, this work therefore proposes EGRT, which naturally integrates emission guidance into therapy. With the tumor targeted accurately and directly by the emission guidance, clinicians will no longer be operating in the dark. The feasibility of accurate tumor tracking in EGRT has been demonstrated using extensive evaluation studies. To establish EGRT as an independent modality for cancer treatment, a complete planning scheme is proposed and has been demonstrated to work as well. Many therapeutic benefits can be derived from the proposed EGRT treatment. The most direct benefit is GTV dose escalation as compared to conventional methods. Other benefits such as the effectiveness of treating multiple metastases are also compelling.

This dissertation has answered the two most important questions for EGRT including the feasibility of tumor tracking and the capability of dose planning. However, the development of EGRT is still at its early stage. Many aspects require further investigation to fully explore the vast possibilities of EGRT treatment. For example, the current planning scheme does not fully account for biological information and tracer distribution. However, tumor radiobiology is extremely relevant to cancer treatment and such information is readily available in EGRT. If appropriately made use of, such information can substantially improve treatment effectiveness through dose painting based on the real-time PET-guided delivery. We hence look forward to future research efforts to push forward EGRT and realize the potential of personalized biologically guided radiotherapy.

APPENDIX A

SIMULATION TOOLS

Part of this appendix is adapted from our previous work on EGRT [29] and listed here for the reader's reference. Modifications have been made.

A.0.1 Overview

Simulation is a good approach to validate the proposed EGRT concept without building an actual system. To make realistic and productive simulations, several effective simulation tools are needed. One is needed to simulate the positron emission process for the acquisition of LOR data. Another tool is needed to simulate the process of dose delivery according to the dynamically determined beamlet responses. Two dedicated Monte Carlo tools (i.e. GATE and VMC++) are finally selected. Due to the intensive computation involved in Monte Carlo simulation, an online cloud-computing application (i.e. CliQr) is employed to speed up simulations. In the planning scheme study, IMRT treatment plans need to be optimized. A commercial optimization package (i.e. MOSEK) and treatment planning system (i.e. Pinnacle workstation) are used. To validate the EGRT concept, a binary application (i.e. EGRT engine) is built for efficient investigations.

A.0.2 GATE

GATE, short for Geant4 Application for Tomographic Emission, is a PET/SPECT dedicated Monte Carlo simulation platform based on Geant4, an opensource package developed by the international OpenGATE collaboration [94, 44, 83]. GATE can be installed in multiple operating systems including Windows and Linux. In this work, we run GATE in Ubuntu 10.04.

Since GATE is an application built on top of Geant4, simulations can be initiated, designed, and controlled by using simple scripts. Sample scripts of various PET systems are available in the installation package so that users can customize their simulations by modifying on them. Therefore, since highly sophisticated experimental settings can be easily configured, GATE now plays a key role in the design of new medical imaging devices, in the optimization of acquisition protocols, and in the development and assessment of image reconstruction algorithms and correction techniques [94].

In order to understand how GATE works, a summary of steps to write a comprehensive GATE script is given below:

1. Define the scanner geometry
2. Define the phantom geometry
3. Set up the physics process
4. Initialize the simulation
5. Set up the detector model (digitizer)
6. Define the sources
7. Specify the data output format
8. Start the data acquisition

GATE is able to not only construct a user-defined phantom, but also read in a voxelized phantom such as the XCAT phantom. An illustration of a GATE simulation system with a voxelized phantom is shown in Figure A.1.

GATE can directly output the coincidence events in list-mode format specifying the 3D coordinates of the two endpoints for each recorded LOR as well as time information. These outputs are then used as inputs for our EGRT algorithms.

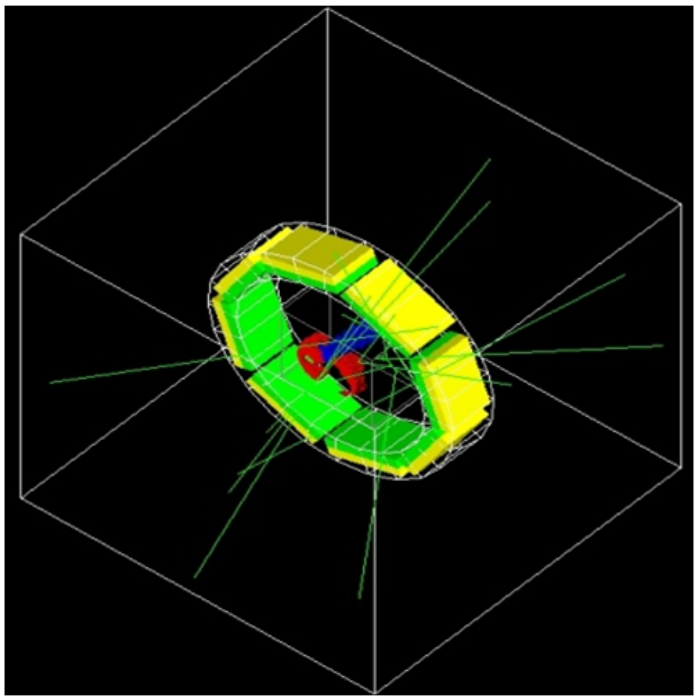

Figure A.1: Illustration of GATE simulation system. The whole system is defined in a cubic volume called **world**. Calculation is done only for particles in the world volume. The ring detector system is placed around the isocenter of the world volume. The voxelized phantom can be read in with its isocenter coincided with that of the world volume.

A.0.3 VMC++

VMC++ (National Research Council, Canada), short for voxel based Monte Carlo package, is a highly efficient Monte Carlo dose calculation engine for radiation therapy treatment planning [47, 46]. It has been validated against well established codes [101]. VMC++ can be easily installed and operated under both Windows and Linux systems. Based on the characteristics of VMC++ (discussed below), it is a perfect fit for the simulation of the Linac dose delivery. The main command of running VMC++ is shown below (in a Windows system):

```
vmc.exe    input_file_name
```

In order to run the VMC++ for customized simulation, the main task is therefore to write an input file which includes the following information:

- The information of the input phantom such as image values and voxel resolution
- Source position and beamlet edge coordinates
- Source spectrum to be used
- Monte Carlo simulation parameters

One input file can only include one point source, thereby simulating dose distribution for only one beamlet response for EGRT. Therefore, an EGRT simulation will need thousands of input files, depending on how many beamlet responses are generated. For each input file, VMC++ simulates the Monte Carlo dose deposited in the phantom according to the beamlet information specified in the input file and then outputs the corresponding 3D dose distribution as a single binary file.

As an example, Figure A.2 shows the VMC++ calculation after a progression of beamlet responses from simulated PET list-mode events for the preliminary water phantom study (see section 3.1.2). The upper left image depicts the dose distribution after only 10 beamlets were delivered, each corresponding to a single previously detected LOR. The bottom right image is the dose distribution after 50,000 beamlets were delivered over a period of 300 s.

A.0.4 CliQr

A major computation in EGRT simulations is the dose distribution calculation of each beamlet response with VMC++ using a MC algorithm. The calculation of one beamlet response is relatively fast which takes about several seconds. However, an EGRT simulation generally results in 10 to 100 thousand beamlet responses. This may take days or even weeks to finish if we simulate all responses sequentially. Considering the need to run many EGRT simulations to test the algorithms or even for debugging purpose, running EGRT simulations in our local computers will not be an ideal option.

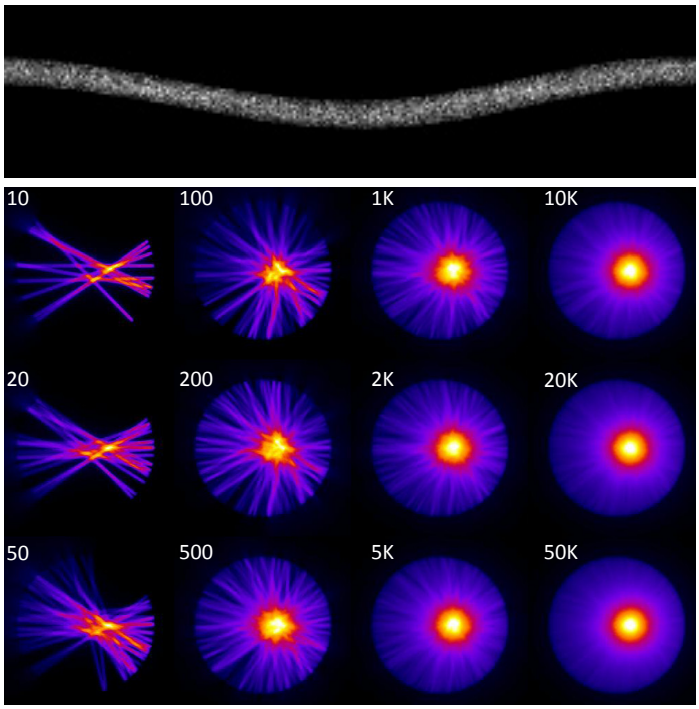

Figure A.2: (Top) Map of bMLC leaf opening counts. Vertical direction is leaf number, horizontal direction is firing position. (Bottom) Dose map progression over logarithmic time scale. Upper left 10 beamlets. Lower right 50,000 beamlets after 300 s. The dose maps are self-normalized to the maximum dose within each case.

Since we do not want to build significant internal hardware infrastructure, the cloud and its almost infinite resources on-demand seemed to be the perfect answer. CliQr (www.cliqr.com) offers a solution that enables us to store our application on the cloud, get on the cloud quickly to start any number of simulations we want, and move from cloud to cloud to get the best performance possible, all without having to change our application or simulation programs in any way. To make full use of cloud resources, we have add the functionality of dividing our beamlet sequence file into many nodes (e.g. 30) so that the simulation time can be shortened to be 1/30 of the original one.

A.0.5 MOSEK

MOSEK is an optimization package to generate IMRT treatment plans for XCAT phantom case in this work. The MOSEK optimization package can be used to solve

large-scale mathematical optimization problems [4]. MOSEK provides fast and efficient specialized solvers for a lot of types of optimization problems including linear problems, quadratic problems, general convex problems, and mixed integer problems. This package can be used with various interfaces including C/C++, .NET, Java, and Python. In this work, MOSEK MATLAB optimization toolbox is called to run the optimization codes.

A.0.6 Pinnacle

To fully demonstrate the feasibility of the EGRT concept, clinical patient data have been collected. Each set of patient data contains gated 4DCT images, gated 4DPET images, raw PET list-mode data, Varian RPM trace data, and breath-hold CT images with planning information such as contours of structures. A commercial Pinnacle treatment planning workstation (Philips Healthcare, Fitchburg, WI) has been used to import all these patient data conveniently together with all clinically contoured structure sets. More importantly, it can be used for customized treatment planning of the patient data and has been very useful during our development of the EGRT planning scheme. Figure A.3 illustrates the Pinnacle interface for customized EGRT planning.

A.0.7 EGRT Engine

After the simulated GATE data or commercial PET scan data are obtained, the subsequent EGRT simulations include a wide variety of simulation tasks that are computation intensive. These include, for example, the process of reading in various input files (e.g. coincidence list mode data, 4DCT images with associate structure files) based on the desired simulation parameters, the implementation of the EGRT basic algorithm on each individual LOR according to the specific EGRT treatment geometry, and consequent Monte Carlo simulations of all resultant beamlet responses

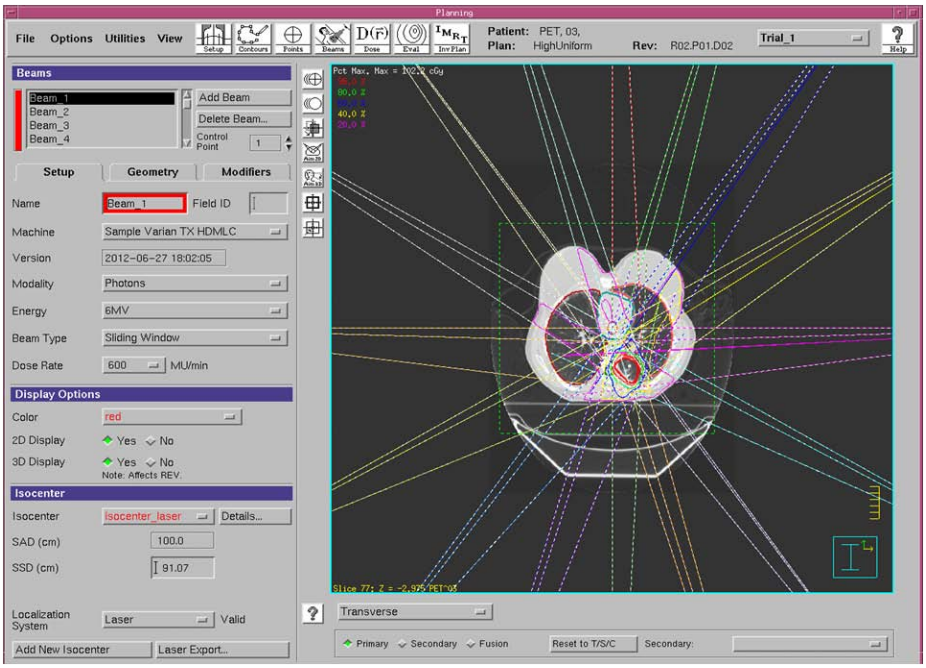

Figure A.3: The Pinnacle interface for customized EGRT planning.

as well as the final dose distribution and DVH calculation which requires image registration.

In addition, the above tasks need to be repeated many times during the early investigation stage of the work. Therefore, it is very desirable to build an application that can perform those resource-consuming jobs efficiently and comprehensively. We used C++ code and algorithms developed by RefleXion Medical (Burlingame, CA), to simulate the EGRT system. RefleXion Medical is a company that is currently developing the first EGRT system.

To run an EGRT simulation, one needs to prepare an appropriate configure file, and then run the following command in any Ubuntu terminal.

```
EGRTSim config.txt
```

where EGRTSim is the name of the EGRT engine binary and the config.txt is the name of the configure file.

A sample configure file is attached in Appendix B for the reader's reference.

APPENDIX B

A SAMPLE CONFIGURE FILE

```
% ExecutionMask [Optional, string, 0000000 ... 1111111]
%
% ExecuteIMRT is true if        (ExecutionMask & 000000001 > 0)
% ExecuteEGRT is true if        (ExecutionMask & 000000010 > 0)
% ExecuteDVH is true if         (ExecutionMask & 000000100 > 0)
% ExecuteFullVMC is true if       (ExecutionMask & 000001000 > 0)
% ExecuteQuickVMC is true if      (ExecutionMask & 000010000 > 0)
% Execute3DIMRT is true if        (ExecutionMask & 000100000 > 0)
% ExecuteSinoRecon is true if     (ExecutionMask & 001000000 > 0)
% WriteCoincidenceToDisk is true if   (ExecutionMask & 010000000 > 0)
% VisualizeVolumes is true if     (ExecutionMask & 100000000 > 0)
%
ExecutionMask 000010010

% CoincidenceDataFile [Optional, <Valid String>, NULL]
% Specifies the processed coincidence data file (assumes a fixed EGRT geometry)
CoincidenceDataFile /home/smazin/HEAD/Code/PETSim/test_pcoin.dat

% CalibrationCoincidenceDataFile [Optional, <Valid String>, NULL]
% Specifies the processed calibration coincidence data file
CalibrationCoincidenceDataFile /home/smazin/HEAD/Code/PETSim/test_cal_pcoin.dat

% AttenuationMapPath [optional, <Valid string> [<positive float>], NULL, -1]
% Path to attenuation map for attenuation correction
% Second argument is water value for CT image. If specified then the map
% will be converted to 511keV.
AttenuationMapPath /data/attenuationmap511keV.dat 0.018

% AttenuationNormCutoffPercentage [optional, float [0..1], 1]
% Percent of max value in atten. map to use as cutoff for taking average of
% for probability normalization.
AttenuationNormCutoffPercentage 1

% PETMapPath [optional, <Valid string>, NULL]
% Path to PET map for PET map correction
PETMapPath /data/PETMap.dat

% PlanningModulationMapPath [optional, <Valid string>, NULL]
% Path to a Planning Modulation map to incorporate IMRT planning into EGRT
% EnforceVolumeFilter OR IgnoreVolumeFilter will specify whether or not
% to use the planning mod map only or in conjunction with the PTV filter
PlanningModulationMapPath /data/PlanModMap.dat IgnoreVolumeFilter

% BatchVMCSize [Optional, positive integer, 200]
% Note that for IMRT and IMRT3D, BatchSize is interally force to '1', to
% overcome deficiencies in the libvmcpp.so interface/API
BatchVMCSize    200

% LogSeverity [Optional, Debug|Error, Error]
% Debug: More verbose comments are output and intermediate files are not deleted.
LogSeverity Error

% OutputFilePrefix [Mandatory, <Valid string>, NULL]
% Specifies the prefix used to name the output files storing the
OutputFilePrefix  Output/Run1
```

```
% GATEDataFile [Optional, <Valid filename>, NULL]
% If specified, PET event data will be generated from GATE coincidence data
GATEDataFile  /home/qfan/HEAD/GateSims/gateCoincidences.dat

% GATEConfigFilePath [Optional, <Valid string>, NULL]
% Specifies the path to the GATE config file (needed to read params for dose mapping)
GATEConfigFilePath  ../../GateSims/sim7_300s_z2.0cm_motionXYZ/phantom.mac

% GATETableMotion [Optional, true|false, false]
% Specifies whether Table Motion was simulated in the GATE simulation.
GATETableMotion   false

% GEListModeNumDataFiles [Optional, <positive integer>, 0]
% If GEListModeNumDataFiles is specified, PET event data will be generated from
% a set of GE list mode data files
% Each GE list mode data file entry should be specified as follows:
% (Filename [string]) (Z-offset [float]) (T-overlap [float(0..1), 0.5])
% (VarianRPMLag [<optional>, float, -10])
GEListModeNumDataFiles  1
~/fromJaeWon/07_06_2010/LM_static 0.0   0.5   -10

% VarianRPMFile [Optional, <Valid string>, <Valid string>, NULL, NULL]
% Specifies the path to the Varian RPM data file to bin list-mode PET/CT data
% Second string should read "BinByPhase" if the motion binning is to be phase-based
VarianRPMFile   Motion.vxp

% VarianRPMMinPos [Optional, float, 0]
% Specifies the minimum position for binning using the VarianRPM motion trajectory.
VarianRPMMinPos 0

% VarianRPMMaxPos [Optional, float, 0]
% Specifies the maximum position for binning using the VarianRPM motion trajectory.
VarianRPMMaxPos 0

% VarianRPMZOffset [Optional, float, 0]
% Specifies the Zoffset for binning using the VarianRPM motion trajectory.
VarianRPMZOffset 0

% VarianRPMMinTriggers [Optional, int, 12]  (must be >= 2)
% The number of triggers that will be checked to determine VarianRPMLag
VarianRPMMinTriggers 12

% CenterOfMassFile [Optional, <valid string>, NULL]
% Specifies filename to use for Center Of Mass text file (Motion Estimator)
CenterOfMassFile /data/fromJaeWon/11_05_2010/LM_Vol-7/Avrg_COM.txt

% PlanningVolumes [Optional, positive integer (Number of volumes)]
% Each volume configured as (data_type=Analytical|Voxelized), (label=[string]),
% (planning_type=PTV|GTV|OAR|BOOST|PTV3DIMRT|NORMVMIN|NORMVMEAN|
% NORMVMAX|NORMVXX|NORMDXX|RX|PET),
% (motion=static|periodic|VarianRPM), egrt-probability [0..1], plotDVH (0 or 1)
PlanningVolumes   1
Voxelized Tumor   GTV   static  1.0  1  /home/ananduri/mask 01001
Analytical  PTV   PTV   static  1.0  1  0 0 0 2 2 2   0 0 0 0
Analytical  Lung  OAR   static  0.01 1  3 3 3 1 1 1 0 0 0 0

% RXDoseLevel [Optional, positive float, 100]
% Dose [Gy] that will be prescribed to the RX Volume
RXDoseLevel 100

% TimeStep [Optional, positive double, 0.0001]
% EndCalibrationTime [Optional, positive double, -1];
% EndTime [Optional, positive double, 10.0]
TimeStep    0.0001
EndCalibrationTime -1
EndTime   10

```

```
% PETDetExtent [Optional, positive double, 2.0]
% PET detector extent in z [cm]
PETDetExtent  2.0

% PETRingRadius [Optional, positive double, 50.0]
% PET arc radius of curvature [cm]
PETRingRadius 50.0

% PETDetWidth [Optional, positive double, 0.1]
% PET detector width [cm]
PETDetWidth 0.1

% Arcs  [Mandatory, positive integer (number of arcs), 0]
% Number of detectors [positive integer], Starting Angle (degrees)
Arcs  2
750   135
750   315

% RingRotationPeriod [Optional, positive double, 1.0]
% Rotation period of gantry [s]
RingRotationPeriod  1

% RingCount [Optional, positive integer, 1]
% Number of PET rings
RingCount 1

% RingZOffset [Optional, double, -0.5]
% Offset (units of PETDetExtent) in the Z-direction, where first ring is situated
RingZOffset -0.5

% TableStartPosZ [Optional, positive double, 0.0]
% Table start position in z (in cm)
TableStartPosZ  0.0

% TableEndPosZ [Optional, positive double, 0.0]
% Table end position in z (in cm)
TableEndPosZ  0.0

% PETRandomAngleAmount [Optional, positive double, 0]
% PET random angle amount to add to second ray [deg]
PETRandomAngleAmount  0

% IsotopeHalfLife [Optional, positive double, 0]
% Halflife (in minutes) of the radioisotope in the PET tracer (e.g. F18 is 109.771)
% determines how much decay will happen when looping occurs
IsotopeHalfLife 0

% LinacPosition [Optional, positive double between [0,360), 90]
% Location in degrees of the linac
LinacPosition 90

% LinacRadius [Optional, positive double, 60]
% Distance (in cm) from linac to center of PET ring
LinacRadius 60

% LinacPower [Optional, positive double, 8.5/60]
% Linac power output (in Gy/s)
LinacPower  0.141666667

% LeafApertureISO [Optional, positive double, 0.5]
% Leaf aperture width at isocenter (cm)
LeafApertureISO   0.5

% LeafApertureISO_Z [Optional, positive double, 0.5]
% Leaf aperture width (in the z-direction) at isocenter (cm)
LeafApertureISO_Z   0.5

% CollimatorAngleSpread [Optional, positive double between [1.0, 60.0), 10.0]
```

```
% Angular spread of the collimator in degrees
CollimatorAngleSpread 10

% CollimatorLeaves [Optional, positive integer between [0,1024), 64]
% Number of leaves on the MLC
CollimatorLeaves  64

% Collimator Radius [Optional, positive double, 50]
% Distance (in cm) from collimator to isocenter
CollimatorRadius  50

% RotateGantryClockwise [Optional, positive boolean, false]
% Specifies whether the gantry (PET detectors and linac) rotates counterclockwise
RotateGantryCounterClockwise  false

% EGRTTimeWindow [Optional, positive double, 0.50]
% Time window (in seconds) for valid PET events
EGRTTimeWindow  0.50

% EGRTAngularSpread [Optional, positive double, 0.5]
% Spread (in degrees) between the linac and a valid PET event (at any given time)
EGRTAngularSpread 0.5

% EGRTZWindow [Optional, positive double, 2.0]
% Z-tolerance for an LOR to be responded to
EGRTZWindow 2.0

% EGRTFiringPoints [Optional, positive integer, 256]
% Number of discrete firing points (along the linac-circle) used by EGRT
EGRTFiringPoints    256

% EGRTGammaTarget [Optional, positive float [0,1], 0]
EGRTGammaTarget 0

% IMRTHelicalPitch [Optional, positive float, 0.2]
% The helical pitch for IMRT treatment (number of rotations per slice traversed)
IMRTHelicalPitch    0.2

% SinogramPhiLines [Optional, positive integer, 210]
% SinogramDistLines [Optional, positive integer, 249]
% Specifies the dimensions of the Sinogram
SinogramPhiLines  210
SinogramDistLines 249

% ReconSizeXYZ [Optional, positive integer, (VMC Phantom Size)]
% BackProjectOffsetXYZ [Optional, positive double, (VMC Phantom Offset)]
% Specifically used by QuickVMC and SinoRecon
ReconSizeXYZ    512   512   1
BackProjectOffsetXYZ  0.0   0.0   0.0

% BackProjectorFOV [Optional, positive double, 50.0]
% Back-projection FOV
BackProjectFOV  50.0

% BackProjectorFOVz [Optional, positive double, 5.0]
% Back-projection FOV in z
BackProjectFOVz 5.0

% BackProjectorOSFactor [Optional, positive integer, 8]
% Back-projection oversampling factor
BackProjectOSFactor 8

% NumPhasesEGRT [Optional, positive integer, 1]
% Number of phases for EGRT simulation
NumPhasesEGRT 1

% NumPhasesIMRT [Optional, positive integer, 1]
% Number of phases for IMRT simulation
```

```
NumPhasesIMRT 1

% MotionPeriod [Optional, positive double, 0.0]
% Period for motion model (for Periodic, if static or VXP this is ignored)
MotionPeriod 0

% DICOMPhaseDir [Optional, <Valid string>, NULL]
% Use to list multiple dicom directories, one per phase
% DICOM files for each directory will be converted to a VMC++ .CT 3D phantom file
% NOTE can either specify DICOMPhaseDir or VMCPhantomFilePath/Prefix but not both
DICOMPhaseDir /data/DICOM/phase00
DICOMPhaseDir /data/DICOM/phase01

% GenerateRTStructROIMask [Optional, <string, string, integer array>, NULL]
% Use to convert RTStruct ROI's into 8-bit masks
% First string: RTStruct file, second string: DICOM ref image directory
GenerateRTStructROIMask /data/rtstruct.dcm /data/dicomCT 0 3 5

% VMCPhantomFilePath [Optional, <Valid string>, NULL]
% Specifies the path to the VMC phantom file.
% NOTE can either specify DICOMPhaseDir or VMCPhantomFilePath/Prefix but not both
VMCPhantomFilePath /data/VMCPhantoms/NCATphantom_256x256x35_2mm.CT

% VMCPhantomFilePathPrefix [Optional, <Valid string>, NULL]
% Specifies the prefix-path to the VMC phantom file for multiple phases.
VMCPhantomFilePathPrefix /data/VMCPhantoms/NCATphantom_256x256x35_2mm

% TruncVMCNewFilePath [Optional, string, NULL]
% If truncating VMC file, this specifies path to output new truncated VMC file
% If not defined the default is the output directory
TruncVMCNewFilePath /mnt/vmc++/phantoms/tempVMC.CT

% TruncVMCNewFilePathPrefix [Optional, string, NULL]
% If truncating VMC file, this specifies path to output new truncated VMC file prefix
% If not defined the default is the output directory
TruncVMCNewFilePathPrefix /mnt/vmc++/phantoms/tempVMC

% VMCPhantomTruncateSlices [Optional, int, int, 0, 1000]
% Specifies the slices to truncate to for the VMC .CT file
% Used to speed up processing time by ignoring slices that receive little to zero dose
% Note if this is used one cannot also specify VMCPhantomTruncateWithZBuffer
VMCPhantomTruncateSlices 0 1000

% VMCNcasePerBeamlet [Optional, positive integer, 10000]
% Specifies the value of VMC ncase per beamlet parameter
VMCNcasePerBeamlet  10000

% VMCNumExecThreads [Optional, integer, 1]
VMCNumExecThreads 1

% QuickVMCMultiplyPhantom [Optional, boolean, false]
% Specifies whether to multiply the VMC phantom by the QuickVMC dose map
QuickVMCMultiplyPhantom false

% DVHLegend [Optional, string, float, string ('all', 12, 'bold')]
% Usage: DVHLegend <show> <fontsize> <fontweight>
DVHLegend all 12  bold

% DVHPlotDoseMap
% Usage: DVHPlotDoseMap <doseprefix> <numphases> <AlgName> <LineWidth> <LineStyle>
DVHPlotDoseMap ./simxxx_vmc_Alg01_Phase 1 IMRT 4.0 --
DVHPlotDoseMap ./simxxx_vmc_Alg00_Phase 6 EGRT 4.0 -

% DVHReportDXX [Optional, float, float, ... (0.95, 0.5)]
% Reports the DXX values for the volumes to be plotted.
% Usage: DVHReportDXX <val1> <val2> etc.
% vals must be between 0 and 1 (exclusive)
%DVHReportDXX 0.95 0.5
```

```
329
% GenImagesTruncate [Optional, true/false, (false)]
331 % Specifies whether generated image overlays should be truncated
GenImagesTruncate false
333
% GenImagesDosePhaseLimits [Optional, float, float (0.2 0.8)]
335 % Low and High multiplicatve values for dose phase overlay images
GenImagesDosePhaseLimits 0.2 0.8
337
% GenImagesColorMap [Optional, string, "jet"]
339 % ColorMap to display dose images in (and contours)
GenImagesColorMap jet
341
% GenImagesContours [Optional, float, float, float, ...]
343 % Contour levels on the POV dose map images [Gy].
GenImagesContours 50 100 200
345
% GenImagesContourParams [Optional, float, string, float, float, float]
347 % <Linewidth>, <Linestyle> and <RGB color> when plotting contours.
GenImagesContourParams 2.0 - -1 -1 -1
349
% GenImagesDrawVolume [Optional, string, float, string, float, float, float]
351 % Usage: GenImagesDrawVolume <VolLabel> <linewidth> <linestyle> <Red Green Blue>
GenImagesDrawVolume Vol1 2.0 -- 0 0 0
353 GenImagesDrawVolume Vol2 2.0 -- 0 1 0

355 % Pinnacle Settings
% Fluence file / start angle (deg) / CW (-1) or CCW (1)
357 % / IsocenterZ (cm) / Num Fields / First Field
% / Last Field / FieldSizeX / FieldSizeZ / FieldDX (cm) / FieldDZ (cm)
359 % / ColWidthX (cm) / ColWidthZ (cm) / SAD (cm)
PinnacleSettings ~/Public/1_16.img 90 -1 0.0 16 0 15 101 101 0.5 0.5 0.5 0.5 100
361
% PinnacleFluenceIsoShift [Optional, float, float, 0.5, 0.5]
363 % Specifies isocenter location in Pinnacle fluence map
% relative to the central pixel in units of pixels
365 PinnacleFluenceIsoShift 0.5 0.5

367 % PinnacleMultiSource [Optional, boolean, false]
% Specifies whether to turn on multi-source 3DIMRT (i.e. non-Z-divergent delivery)
369 PinnacleMultiSource false

371 % PinnacleGenerateDoseKernels [Optional, boolean, false]
% Specifies whether to generate the dose kernels for all beamlets in the given field
373 PinnacleGenerateDoseKernels false
```

Listing B.1: EGRT configure file.

REFERENCES

[1] "Prostate seed implant." `http://www.swrads.org/012_prostate%20seed.html`, May 2013.

[2] "Radiation therapy for cancer." `http://www.cancer.gov/cancertopics/factsheet/Therapy/radiation/`, May 2013.

[3] Abeloff, M. D., Armitage, J. O., Niederhuber, J. E., Kastan, M. B., and McKenna, W. G., *Abeloff's clinical oncology*. Churchill Livingstone/Elsevier Philadelphia, 2008.

[4] Anderson, E., "The MOSEK Optimization Toolbox for MATLAB Version 2.5, Users Guide and Reference Manual," *World Wide Web, http://www. mosek. com (1999–2002)*.

[5] Avril, N. E. and Weber, W. A., "Monitoring response to treatment in patients utilizing PET," *The Radiologic clinics of North America*, vol. 43, no. 1, 2005.

[6] Baumann, P., Nyman, J., Hoyer, M., Wennberg, B., Gagliardi, G., Lax, I., Drugge, N., Ekberg, L., Friesland, S., Johansson, K.-A., and others, "Outcome in a prospective phase II trial of medically inoperable stage I non–small-cell lung cancer patients treated with stereotactic body radiotherapy," *Journal of Clinical Oncology*, vol. 27, no. 20, pp. 3290–3296, 2009.

[7] Bel, A., Petrascu, O., Van de Vondel, I., Coppens, L., Linthout, N., Verellen, D., and Storme, G., "A computerized remote table control for fast on-line patient repositioning: Implementation and clinical feasibility," *Medical physics*, vol. 27, p. 354, 2000.

[8] Berbeco, R. I., Mostafavi, H., Sharp, G. C., and Jiang, S. B., "Towards fluoroscopic respiratory gating for lung tumours without radiopaque markers," *physics in Medicine and Biology*, vol. 50, no. 19, p. 4481, 2005.

[9] Beyer, T., Townsend, D., Brun, T., Kinahan, P., Charron, M., Roddy, R., Jerin, J., Young, J., Byars, L., and Nutt, R., "A combined PET/CT scanner for clinical oncology," *Journal of Nuclear Medicine*, vol. 41, no. 8, pp. 1369–1379, 2000.

[10] Bichay, T., Cao, D., Orton, C. G., and others, "Helical tomotherapy will ultimately replace linear accelerator based IMRT as the best way to deliver conformal radiotherapy," *Medical physics*, vol. 35, p. 1625, 2008.

[11] Britton, K. R., Takai, Y., Mitsuya, M., Nemoto, K., Ogawa, Y., Yamada, S., and others, "Evaluation of inter-and intrafraction organ motion during intensity modulated radiation therapy (IMRT) for localized prostate cancer measured by a newly developed on-board image-guided system," *Radiation medicine*, vol. 23, no. 1, pp. 14–24, 2005.

[12] Brix, G., Lechel, U., Glatting, G., Ziegler, S. I., Münzing, W., Müller, S. P., and Beyer, T., "Radiation exposure of patients undergoing whole-body dual-modality 18F-FDG PET/CT examinations," *Journal of Nuclear Medicine*, vol. 46, no. 4, pp. 608–613, 2005.

[13] Carol, M., "Peacock: A System for Planning and Rotational Delivery of Intensity-Modulated Fields," *International Journal of Imaging Systems and Technology*, vol. 6, no. 1, pp. 56–61, 1995.

[14] Chamberland, M., Wassenaar, R., Spencer, B., and Xu, T., "Performance evaluation of real-time motion tracking using positron emission fiducial markers," *Medical physics*, vol. 38, p. 810, 2011.

[15] Chang, S. D., Main, W., Martin, D. P., Gibbs, I. C., and Heilbrun, M. P., "An analysis of the accuracy of the CyberKnife: a robotic frameless stereotactic radiosurgical system," *Neurosurgery*, vol. 52, no. 1, pp. 140–147, 2003.

[16] Chen, M., Chen, Y., Chen, Q., and Lu, W., "Theoretical analysis of the thread effect in helical TomoTherapy," *Medical physics*, vol. 38, no. 11, pp. 5945–5960, 2011.

[17] Chen, Q.-S., Weinhous, M. S., Deibel, F. C., Ciezki, J. P., and Macklis, R. M., "Fluoroscopic study of tumor motion due to breathing: facilitating precise radiation therapy for lung cancer patients," *Medical physics*, vol. 28, p. 1850, 2001.

[18] Cherry, S. R., Sorenson, J. A., and Phelps, M. E., *Physics in nuclear medicine*. Saunders, 2012.

[19] Coleman, R., Laymon, C., and Turkington, T., "FDG imaging of lung nodules: a phantom study comparing SPECT, camera-based PET, and dedicated PET," *Radiology*, vol. 210, no. 3, p. 823, 1999.

[20] Cui, Y., Dy, J. G., Sharp, G. C., Alexander, B., and Jiang, S. B., "Multiple template-based fluoroscopic tracking of lung tumor mass without implanted fiducial markers," *Physics in medicine and biology*, vol. 52, no. 20, p. 6229, 2007.

[21] De Ruysscher, D. and Kirsch, C.-M., "PET scans in radiotherapy planning of lung cancer," *Radiotherapy and Oncology*, vol. 96, no. 3, pp. 335–338, 2010.

[22] DeVita Jr, V. T., Lawrence, T. S., and Rosenberg, S. A., *Cancer: Principles & Practice of Oncology*, vol. 1. Lippincott Williams & Wilkins, 2010.

[23] Dogan, N., King, S., Emami, B., Mohideen, N., Mirkovic, N., Leybovich, L. B., and Sethi, A., "Assessment of different IMRT boost delivery methods on target coverage and normal-tissue sparing," *International Journal of Radiation Oncology* Biology* Physics*, vol. 57, no. 5, pp. 1480–1491, 2003.

[24] D'Souza, W. D., Nazareth, D. P., Zhang, B., Deyoung, C., Suntharalingam, M., Kwok, Y., Yu, C. X., Regine, W. F., and others, "The use of gated and 4D CT imaging in planning for stereotactic body radiation therapy," *Medical dosimetry: official journal of the American Association of Medical Dosimetrists*, vol. 32, no. 2, p. 92, 2007.

[25] Enmark, M., Korreman, S., and Nyström, H., "IGRT of prostate cancer: is the margin reduction gained from daily IG time-dependent?," *Acta Oncologica*, vol. 45, no. 7, pp. 907–914, 2006.

[26] Everitt, S., Hicks, R., Ball, D., Kron, T., Schneider-Kolsky, M., Walter, T., Binns, D., and Mac Manus, M., "Imaging cellular proliferation during chemo-radiotherapy: a pilot study of serial 18F-FLT positron emission tomography/computed tomography imaging for non-small-cell lung cancer," *International Journal of Radiation Oncology* Biology* Physics*, vol. 75, no. 4, pp. 1098–1104, 2009.

[27] Ezzell, G., Eisbrauchi, A., Yu, C., Butler, B., Xiao, Y., Rosen, I., Rosenman, J., Sharpe, M., Xing, L., Xia, P., and others, "Implementing IMRT in clinical practice: a joint document of the American Society for Therapeutic Radiology and Oncology and the American Association of Physicists in Medicine," *Int. J. Radiation Oncology Biol. Phys*, vol. 58, no. 5, pp. 1616–1634, 2004.

[28] Fan, Q. and Zhu, L., "Emission guided radiation therapy: A simulation study of treatment without margin," *Medical Physics*, vol. 37, p. 3330, 2010.

[29] Fan, Q., "Emission guided radiation therapy: a feasibility study," 2010.

[30] Fan, Q., Nanduri, A., Mazin, S., Zhu, L., and others, "Emission guided radiation therapy for lung and prostate cancers: A feasibility study on a digital patient," *Medical physics*, vol. 39, no. 11, p. 7140, 2012.

[31] Forrest, Mackie, Ruchala, and etc, "The utility of megavoltage computed tomography images from a helical tomotherapy system for setup verification purposes," *International Journal of Radiation Oncology* Biology* Physics*, vol. 60, no. 2, pp. 1639–1644, 2004.

[32] Gambhir, S., Czernin, J., Schwimmer, J., Silverman, D., Coleman, R., and Phelps, M., "A tabulated summary of the FDG PET literature," *Journal of Nuclear Medicine*, vol. 42, no. 5 suppl, p. 1S, 2001.

[33] Geraghty, P. R., Kee, S. T., McFarlane, G., Razavi, M. K., Sze, D. Y., and Dake, M. D., "Ct-guided transthoracic needle aspiration biopsy of pulmonary nodules: Needle size and pneumothorax rate," *Radiology*, vol. 229, no. 2, pp. 475–481, 2003.

[34] Gierga, D. P., Brewer, J., Sharp, G. C., Betke, M., Willett, C. G., and Chen, G. T., "The correlation between internal and external markers for abdominal tumors: implications for respiratory gating," *International Journal of Radiation Oncology* Biology* Physics*, vol. 61, no. 5, pp. 1551–1558, 2005.

[35] Grills, I. S., Mangona, V. S., Welsh, R., Chmielewski, G., McInerney, E., Martin, S., Wloch, J., Ye, H., and Kestin, L. L., "Outcomes after stereotactic lung radiotherapy or wedge resection for stage I non-small-cell lung cancer," *Journal of clinical oncology*, vol. 28, no. 6, pp. 928–935, 2010.

[36] Grosu, A., Astner, S., Riedel, E., Nieder, C., Wiedenmann, N., Heinemann, F., Schwaiger, M., Molls, M., Weber, W., and others, "An interindividual comparison of O-(2-[18F] Fluoroethyl)-L-Tyrosine (FET)- and L-[Methyl-11C] Methionine (MET)-PET in patients with brain gliomas and metastases," *International Journal of Radiation Oncology* Biology* Physics*, 2011.

[37] Guckenberger, M., Meyer, J., Wilbert, J., Richter, A., Baier, K., Mueller, G., and Flentje, M., "Intra-fractional uncertainties in cone-beam CT based image-guided radiotherapy (IGRT) of pulmonary tumors," *Radiotherapy and oncology*, vol. 83, no. 1, pp. 57–64, 2007.

[38] Hall, E. J. and Giaccia, A. J., *Radiobiology for the Radiologist, 6e.* Lippincott Williams & Wilkins, 2006.

[39] Hanley, J., Debois, M. M., Mah, D., Mageras, G. S., Raben, A., Rosenzweig, K., Mychalczak, B., Schwartz, L. H., Gloeggler, P. J., Lutz, W., and others, "Deep inspiration breath-hold technique for lung tumors: the potential value of target immobilization and reduced lung density in dose escalation," *International Journal of Radiation Oncology* Biology* Physics*, vol. 45, no. 3, pp. 603–611, 1999.

[40] Henderson, M., Hoopes, D., Fletcher, J., Lin, P., Tann, M., Yiannoutsos, C., Williams, M., Fakiris, A., McGarry, R., and Timmerman, R., "A pilot trial of serial 18F-Fluorodeoxyglucose Positron Emission Tomography in patients with medically inoperable stage I non–small-cell lung cancer treated with hypofractionated stereotactic body radiotherapy," *International Journal of Radiation Oncology* Biology* Physics*, vol. 76, no. 3, pp. 789–795, 2010.

[41] Hicks, R. J., "The role of PET in monitoring therapy," *Cancer Imaging*, vol. 5, no. 1, p. 51, 2005.

[42] Hoisak, J. D., Sixel, K. E., Tirona, R., Cheung, P. C., and Pignol, J.-P., "Correlation of lung tumor motion with external surrogate indicators of respiration," *International Journal of Radiation Oncology* Biology* Physics*, vol. 60, no. 4, pp. 1298–1306, 2004.

[43] Hugo, G. D., Agazaryan, N., and Solberg, T. D., "An evaluation of gating window size, delivery method, and composite field dosimetry of respiratory-gated IMRT," *Medical physics*, vol. 29, p. 2517, 2002.

[44] Jan, S., Santin, G., Strul, D., Staelens, S., Assie, K., Autret, D., Avner, S., Barbier, R., Bardies, M., Bloomfield, P., and others, "GATE: a simulation toolkit for PET and SPECT," *Arxiv preprint physics/0408109*, 2004.

[45] Jiang, S. B., Pope, C., Al Jarrah, K. M., Kung, J. H., Bortfeld, T., and Chen, G. T., "An experimental investigation on intra-fractional organ motion effects in lung IMRT treatments," *Physics in medicine and biology*, vol. 48, no. 12, p. 1773, 2003.

[46] Kawrakow, I., "Improved modeling of multiple scattering in the Voxel Monte Carlo model," *Medical Physics*, vol. 24, p. 505, 1997.

[47] Kawrakow, I., Fippel, M., and Friedrich, K., "3D electron dose calculation using a Voxel based Monte Carlo algorithm (VMC)," *Medical physics*, vol. 23, p. 445, 1996.

[48] Keall, P. J., Cattell, H., Pokhrel, D., Dieterich, S., Wong, K. H., Murphy, M. J., Vedam, S. S., Wijesooriya, K., and Mohan, R., "Geometric accuracy of a real-time target tracking system with dynamic multileaf collimator tracking system," *International Journal of Radiation Oncology* Biology* Physics*, vol. 65, no. 5, pp. 1579–1584, 2006.

[49] Keall, P. J., Mageras, G., Balter, J., Emery, R., Forster, K., Jiang, S., Kapatoes, J., Kubo, H., Low, D., Murphy, M., and others, "The management of respiratory motion in radiation oncology: Handout for AAPM 2005 continuing education session," *AAPM TG-76*, 2005.

[50] Keall, P., Joshi, S., Vedam, S., Siebers, J., Kini, V., and Mohan, R., "Four-dimensional radiotherapy planning for DMLC-based respiratory motion tracking," *Medical physics*, vol. 32, pp. 942–951, 2005.

[51] King, Brooks, G. P. C. and Presti, "Stereotactic body radiotherapy for localized prostate cancer: interim results of a prospective phase II clinical trial," *International Journal of Radiation Oncology* Biology* Physics*, vol. 73, no. 20, pp. 1043–1048, 2009.

[52] Kondziolka, D., Patel, A., Lunsford, L. D., Kassam, A., Flickinger, J. C., and others, "Stereotactic radiosurgery plus whole brain radiotherapy

versus radiotherapy alone for patients with multiple brain metastases.," *International journal of radiation oncology, biology, physics*, vol. 45, no. 2, p. 427, 1999.

[53] Kubo, H. D. and Hill, B. C., "Respiration gated radiotherapy treatment: a technical study," *Physics in medicine and biology*, vol. 41, no. 1, p. 83, 1996.

[54] Kupelian, P., Willoughby, T., Mahadevan, A., Djemil, T., Weinstein, G., Jani, S., Enke, C., Solberg, T., Flores, N., Liu, D., and others, "Multi-institutional clinical experience with the Calypso system in localization and continuous, real-time monitoring of the prostate gland during external radiotherapy," *International Journal of Radiation Oncology* Biology* Physics*, vol. 67, no. 4, pp. 1088–1098, 2007.

[55] Langen, K. M., Papanikolaou, N., Balog, J., Crilly, R., Followill, D., Goddu, S. M., Grant III, W., Olivera, G., Ramsey, C. R., and Shi, C., "QA for helical tomotherapy: Report of the AAPM Task Group 148," *Medical physics*, vol. 37, p. 4817, 2010.

[56] Li, X. A., Wang, J. Z., Jursinic, P. A., Lawton, C. A., and Wang, D., "Dosimetric advantages of IMRT simultaneous integrated boost for high-risk prostate cancer," *International Journal of Radiation Oncology* Biology* Physics*, vol. 61, no. 4, pp. 1251–1257, 2005.

[57] Lin, T., Cervino, L. I., Tang, X., Vasconcelos, N., and Jiang, S. B., "Fluoroscopic tumor tracking for image-guided lung cancer radiotherapy," *Physics in medicine and biology*, vol. 54, no. 4, p. 981, 2009.

[58] Litzenberg, D. W., Balter, J. M., Lam, K. L., Sandler, H. M., and Ten Haken, R. K., "Retrospective analysis of prostate cancer patients with implanted gold markers using off-line and adaptive therapy protocols," *International Journal of Radiation Oncology* Biology* Physics*, vol. 63, no. 1, pp. 123–133, 2005.

[59] Mackie, T., Balog, J., Ruchala, K., Shepard, D., Aldridge, S., Fitchard, E., Reckwerdt, P., Olivera, G., McNutt, T., and Mehta, M., "Tomotherapy," *Seminars in Radiation Oncology*, vol. 9, no. 1, pp. 108–117, 1999.

[60] Mackie, T., Holmes, T., Swerdloff, S., Reckwerdt, P., Deasy, J., Yang, J., Paliwal, B., and Kinsella, T., "Tomotherapy: a new concept for the delivery of dynamic conformal radiotherapy," *Medical Physics*, vol. 20, p. 1709, 1993.

[61] Mackie, T., Holmes, T., Reckwerdt, P., and Yang, J., "Tomotherapy: optimized planning and delivery of radiation therapy," *International Journal of Imaging Systems and Technology*, vol. 6, pp. 43–43, 1995.

[62] Malinowski, K., Noel, C., Lu, W., Lechleiter, K., Hubenschmidt, J., Low, D., and Parikh, P., "Development of the 4D phantom for patient-specific, end-to-end radiation therapy QA," in *Proceedings of SPIE*, vol. 6510, p. 65100E, 2007.

[63] Marks, L. B., "Conventional fractionated radiation therapy vs radiosurgery for selected benign intracranial lesions (arteriovenous malformations, pituitary adenomas, and acoustic neuromas)," *Journal of neuro-oncology*, vol. 17, no. 3, pp. 223–230, 1993.

[64] Marks, L. B., "Dosimetric predictors of radiation-induced lung injury," *International Journal of Radiation Oncology* Biology* Physics*, vol. 54, no. 2, pp. 313–316, 2002.

[65] Marks, L. B., Yorke, E. D., Jackson, A., Ten Haken, R. K., Constine, L. S., Eisbruch, A., Bentzen, S. M., Nam, J., and Deasy, J. O., "Use of normal tissue complication probability models in the clinic," *International Journal of Radiation Oncology* Biology* Physics*, vol. 76, no. 3, pp. S10–S19, 2010.

[66] Mayse, M. L., Parikh, P. J., Lechleiter, K. M., Dimmer, S., Park, M., Chaudhari, A., Talcott, M., Low, D. A., and Bradley, J. D., "Bronchoscopic implantation of a novel wireless electromagnetic transponder in the canine lung: a feasibility study," *International Journal of Radiation Oncology* Biology* Physics*, vol. 72, no. 1, pp. 93–98, 2008.

[67] Mazin, S., Nanduri, A., and Pelc, N., "Emission Guided Radiation Therapy System: A Feasibility Study," *Medical Physics*, vol. 37, p. 3145, 2010.

[68] Mazin, S., Yang, J., Yamamoto, T., and Nanduri, A., "Free breathing motion tracking in Emission Guided Radiation Therapy," *Medical Physics*, vol. 38, p. 3478, 2011.

[69] McQuaid, D. and Webb, S., "IMRT delivery to a moving target by dynamic MLC tracking: delivery for targets moving in two dimensions in the beam's eye view," *Physics in medicine and biology*, vol. 51, no. 19, p. 4819, 2006.

[70] Murphy, M. J., "Tracking moving organs in real time," in *Seminars in radiation oncology*, vol. 14, pp. 91–100, Elsevier, 2004.

[71] Padhani, A., Krohn, K., Lewis, J., and Alber, M., "Imaging oxygenation of human tumours," *European radiology*, vol. 17, no. 4, pp. 861–872, 2007.

[72] Palma, D., Visser, O., Lagerwaard, F. J., Belderbos, J., Slotman, B., and Senan, S., "Treatment of stage I NSCLC in elderly patients: a population-based matched-pair comparison of stereotactic radiotherapy versus surgery," *Radiotherapy and Oncology*, vol. 101, no. 2, pp. 240–244, 2011.

[73] Park, C., Papiez, L., Zhang, S., Story, M., Timmerman, R. D., and others, "Universal survival curve and single fraction equivalent dose: useful tools in understanding potency of ablative radiotherapy," *International journal of radiation oncology, biology, physics*, vol. 70, no. 3, p. 847, 2008.

[74] Pickren, J., Lopez, G., Tsukada, Y., and Lane, W., "Brain metastases: An autopsy study," in *Cancer Treat Symp*, vol. 2, pp. 295–313, 1983.

[75] Pratx, G., *Image Reconstruction in High Resolution PET: GPU Accelerated Strategies for Improving Image Quality and Accuracy*. Stanford University, 2010.

[76] Rajendran, J. and Krohn, K., "Imaging hypoxia and angiogenesis in tumors," *Radiologic Clinics of North America*, vol. 43, no. 1, pp. 169–187, 2005.

[77] Rao, M., Yang, W., Chen, F., Sheng, K., Ye, J., Mehta, V., Shepard, D., and Cao, D., "Comparison of Elekta VMAT with helical tomotherapy and fixed field IMRT: plan quality, delivery efficiency and accuracy," *Medical physics*, vol. 37, p. 1350, 2010.

[78] Riboldi, M., Sharp, G., Baroni, G., and Chen, G., "Four-dimensional targeting error analysis in image-guided radiotherapy," *Physics in medicine and biology*, vol. 54, no. 19, p. 5995, 2009.

[79] Rosenberg, I., "Radiation oncology physics: A handbook for teachers and students," *British Journal of Cancer*, vol. 98, no. 5, pp. 1020–1020, 2008.

[80] Rosu, M. and Hugo, G. D., "Advances in 4D radiation therapy for managing respiration: Part II-4D treatment planning," *Zeitschrift für Medizinische Physik*, 2012.

[81] Sawant, A., Venkat, R., Srivastava, V., Carlson, D., Povzner, S., Cattell, H., and Keall, P., "Management of three-dimensional intrafraction motion through real-time DMLC tracking," *Medical physics*, vol. 35, p. 2050, 2008.

[82] Schmid, D. T., John, H., Zweifel, R., Cservenyak, T., Westera, G., Goerres, G. W., von Schulthess, G. K., and Hany, T. F., "Fluorocholine PET/CT in patients with prostate cancer: Initial experience," *Radiology*, vol. 235, no. 2, pp. 623–628, 2005.

[83] Schmidtlein, C., Kirov, A., Nehmeh, S., Erdi, Y., Humm, J., Amols, H., Bidaut, L., Ganin, A., Stearns, C., McDaniel, D., and others, "Validation of GATE Monte Carlo simulations of the GE Advance/Discovery LS PET scanners," *Medical Physics*, vol. 33, p. 198, 2006.

[84] Schuster, D., Votaw, J., Nieh, P., Yu, W., Nye, J., Master, V., Bowman, F., Issa, M., and Goodman, M., "Initial experience with the radiotracer anti-1-amino-3-18F-fluorocyclobutane-1-carboxylic acid with PET/CT in

prostate carcinoma," *Journal of Nuclear Medicine*, vol. 48, no. 1, pp. 56–63, 2007.

[85] Segars, W., Mahesh, M., Beck, T., Frey, E., and Tsui, B., "Realistic CT simulation using the 4D XCAT phantom," *Medical physics*, vol. 35, p. 3800, 2008.

[86] Seppenwoolde, Y., Shirato, H., Kitamura, K., Shimizu, S., van Herk, M., Lebesque, J. V., and Miyasaka, K., "Precise and real-time measurement of 3D tumor motion in lung due to breathing and heartbeat, measured during radiotherapy," *International Journal of Radiation Oncology* Biology* Physics*, vol. 53, no. 4, pp. 822–834, 2002.

[87] Shirato, H., Harada, T., Harabayashi, T., Hida, K., Endo, H., Kitamura, K., Onimaru, R., Yamazaki, K., Kurauchi, N., Shimizu, T., and others, "Feasibility of insertion/implantation of 2.0-mm-diameter gold internal fiducial markers for precise setup and real-time tumor tracking in radiotherapy," *International Journal of Radiation Oncology* Biology* Physics*, vol. 56, no. 1, pp. 240–247, 2003.

[88] Shirato, H., Shimizu, S., Kunieda, T., Kitamura, K., van Herk, M., Kagei, K., Nishioka, T., Hashimoto, S., Fujita, K., Aoyama, H., and others, "Physical aspects of a real-time tumor-tracking system for gated radiotherapy," *International Journal of Radiation Oncology* Biology* Physics*, vol. 48, no. 4, pp. 1187–1195, 2000.

[89] Shirato, H., Suzuki, K., Sharp, G. C., Fujita, K., Onimaru, R., Fujino, M., Kato, N., Osaka, Y., Kinoshita, R., Taguchi, H., and others, "Speed and amplitude of lung tumor motion precisely detected in four-dimensional setup and in real-time tumor-tracking radiotherapy," *International Journal of Radiation Oncology* Biology* Physics*, vol. 64, no. 4, pp. 1229–1236, 2006.

[90] Siddon, R. L., "Fast calculation of the exact radiological path for a three-dimensional CT array," *Medical physics*, vol. 12, p. 252, 1985.

[91] Slotman, B. J., Lagerwaard, F. J., and Senan, S., "4D imaging for target definition in stereotactic radiotherapy for lung cancer," *Acta Oncologica*, vol. 45, no. 7, pp. 966–972, 2006.

[92] Steenbakkers, R. J., Duppen, J. C., Fitton, I., Deurloo, K. E., Zijp, L. J., Comans, E. F., Uitterhoeve, A. L., Rodrigus, P. T., Kramer, G. W., Bussink, J., and others, "Reduction of observer variation using matched CT-PET for lung cancer delineation: a three-dimensional analysis," *International Journal of Radiation Oncology* Biology* Physics*, vol. 64, no. 2, pp. 435–448, 2006.

[93] Stevens, C. W., Munden, R. F., Forster, K. M., Kelly, J. F., Liao, Z., Starkschall, G., Tucker, S., and Komaki, R., "Respiratory-driven lung tumor motion is independent of tumor size, tumor location, and pulmonary function," *International Journal of Radiation Oncology* Biology* Physics*, vol. 51, no. 1, pp. 62–68, 2001.

[94] Strulab, D., Santin, G., Lazaro, D., Breton, V., and Morel, C., "GATE (Geant4 Application for Tomographic Emission): a PET/SPECT general-purpose simulation platform," *Nuclear Physics B (Proceedings Supplements)*, vol. 125, pp. 75–79, 2003.

[95] Thorwarth, D., Geets, X., and Paiusco, M., "Physical radiotherapy treatment planning based on functional PET/CT data," *Radiotherapy and Oncology*, vol. 96, no. 3, pp. 317–324, 2010.

[96] Timmerman, R., Paulus, R., Galvin, J., Michalski, J., Straube, W., Bradley, J., Fakiris, A., Bezjak, A., Videtic, G., Johnstone, D., and others, "Stereotactic body radiation therapy for inoperable early stage lung cancer," *JAMA: the journal of the American Medical Association*, vol. 303, no. 11, pp. 1070–1076, 2010.

[97] Tsunashima, Y., Sakae, T., Shioyama, Y., Kagei, K., Terunuma, T., Nohtomi, A., and Akine, Y., "Correlation between the respiratory waveform measured using a respiratory sensor and 3D tumor motion in gated radiotherapy," *International Journal of Radiation Oncology* Biology* Physics*, vol. 60, no. 3, pp. 951–958, 2004.

[98] Turkington, T. G., "Introduction to PET instrumentation," *Journal of nuclear medicine technology*, vol. 29, no. 1, pp. 4–11, 2001.

[99] Underberg, R. W., Lagerwaard, F. J., Slotman, B. J., Cuijpers, J. P., and Senan, S., "Use of maximum intensity projections (MIP) for target volume generation in 4DCT scans for lung cancer," *International Journal of Radiation Oncology* Biology* Physics*, vol. 63, no. 1, pp. 253–260, 2005.

[100] van Baardwijk, A., Bosmans, G., Dekker, A., van Kroonenburgh, M., Boersma, L., Wanders, S., Öllers, M., Houben, R., Minken, A., Lambin, P., and others, "Time trends in the maximal uptake of FDG on PET scan during thoracic radiotherapy. A prospective study in locally advanced non-small cell lung cancer (NSCLC) patients," *Radiotherapy and oncology*, vol. 82, no. 2, pp. 145–152, 2007.

[101] Vatanen, T., Traneus, E., and Lahtinen, T., "Dosimetric verification of a Monte Carlo electron beam model for an add-on eMLC," *Physics in medicine and biology*, vol. 53, no. 2, p. 391, 2008.

[102] Wagman, R., Yorke, E., Ford, E., Giraud, P., Mageras, G., Minsky, B., and Rosenzweig, K., "Respiratory gating for liver tumors: use in dose

escalation," *International Journal of Radiation Oncology* Biology* Physics*, vol. 55, no. 3, pp. 659–668, 2003.

[103] Wang, C., "Improved local control of nasopharyngeal carcinoma after intracavitary brachytherapy boost," *American journal of clinical oncology*, vol. 14, no. 1, pp. 5–8, 1991.

[104] Wiersma, R. D., Wen, Z., Sadinski, M., Farrey, K., and Yenice, K. M., "Development of a frameless stereotactic radiosurgery system based on real-time 6D position monitoring and adaptive head motion compensation," *Physics in medicine and biology*, vol. 55, no. 2, p. 389, 2010.

[105] Willoughby, T. R., Kupelian, P. A., Pouliot, J., Shinohara, K., Aubin, M., Roach III, M., Skrumeda, L. L., Balter, J. M., Litzenberg, D. W., Hadley, S. W., and others, "Target localization and real-time tracking using the Calypso 4D localization system in patients with localized prostate cancer," *International Journal of Radiation Oncology* Biology* Physics*, vol. 65, no. 2, pp. 528–534, 2006.

[106] Wong, J., Hardcastle, N., Tomé, W., Bayliss, A., Tolakanahalli, R., Lerch, M., Petasecca, M., Carolan, M., Metcalfe, P., and Rosenfeld, A., "Independent quality assurance of a helical tomotherapy machine using the dose magnifying glass," *Medical Physics*, vol. 38, no. 4, pp. 2256–2264, 2011.

[107] Wong, J. W., Sharpe, M. B., Jaffray, D. A., Kini, V. R., Robertson, J. M., Stromberg, J. S., and Martinez, A. A., "The use of active breathing control (ABC) to reduce margin for breathing motion," *International Journal of Radiation Oncology* Biology* Physics*, vol. 44, no. 4, pp. 911–919, 1999.

[108] Wu, Q., Mohan, R., Morris, M., Lauve, A., Schmidt-Ullrich, R., and others, "Simultaneous integrated boost intensity-modulated radiotherapy for locally advanced head-and-neck squamous cell carcinomas. I: dosimetric results," *International journal of radiation oncology, biology, physics*, vol. 56, no. 2, p. 573, 2003.

[109] Xing, L., Li, J., Donaldson, S., Le, Q., and Boyer, A., "Optimization of importance factors in inverse planning," *Physics in medicine and biology*, vol. 44, no. 10, p. 2525, 1999.

[110] Xing, L., Thorndyke, B., Schreibmann, E., Yang, Y., Li, T.-F., Kim, G.-Y., Luxton, G., Koong, A., and others, "Overview of image-guided radiation therapy," *Medical Dosimetry*, vol. 31, no. 2, pp. 91–112, 2006.

[111] Xu, T., Wong, J. T., Shikhaliev, P. M., Ducote, J. L., Al-Ghazi, M. S., and Molloi, S., "Real-time tumor tracking using implanted positron emission markers: concept and simulation study," *Medical physics*, vol. 33, p. 2598, 2006.

[112] Yang, J., Yamamoto, T., Thielemans, K., Mazin, S., Graves, E., and Keall, P., "A feasibility study for real-time tumor tracking using positron emission tomography (PET)," *Medical Physics*, vol. 38, p. 3479, 2011.

[113] Zhu, L., Lee, L., Ma, Y., Ye, Y., Mazzeo, R., and Xing, L., "Using total-variation regularization for intensity modulated radiation therapy inverse planning with field-specific numbers of segments," *Physics in medicine and biology*, vol. 53, p. 6653, 2008.

[114] ZHU, L., NIU, T., CHOI, K., and XING, L., "Total-variation regularization based inverse planning for intensity modulated arc therapy," *Technology in cancer research & treatment*, vol. 11, no. 2, pp. 149–162, 2012.

[115] Zhu, L. and Xing, L., "Search for IMRT inverse plans with piecewise constant fluence maps using compressed sensing techniques," *Medical physics*, vol. 36, p. 1895, 2009.